Surface morphology control at the nanoscale by temporal and polarization control of ultrafast laser pulses

Anthony Nakhoul

N°d'ordre NNT: **2022STET0048**

THÈSE de DOCTORAT
DE L'UNIVERSITÉ JEAN MONNET SAINT-ÉTIENNE

Membre de l'université de Lyon

École Doctorale N° 488
Sciences Ingénierie Santé SIS

Spécialité / discipline de doctorat :
Science et génie des matériaux

Soutenue publiquement le 29/11/2022, par :
Anthony Nakhoul

Morphologie de surface à l'échelle nanométrique par contrôle temporel et de polarisation des impulsions laser ultracourtes

---

Devant le jury composé de :

OLIVIER UTEZA	Université Aix-Marseille	Président
EMMANUEL STRATAKIS	FORTH-IESL	Rapporteur
JÖRN BONSE	BAM, Berlin	Rapporteur
FLORENCE GARRELIE	Université Jean-Monnet	Examinatrice
FLORENT PIGEON	Université Jean-Monnet	Invité
CLAIRE MAURICE	Ecole des Mines de Saint-Etienne	Co-directrice de thèse
JEAN-PHILIPPE COLOMBIER	Université Jean-Monnet	Directeur de thèse

Acknowledgements

The work presented in this Doctoral thesis is devoted to the experimental and theoretical study of surface morphology control on nanometric scale induced by ultrafast laser pulses. The Doctoral thesis consists of a short introduction and a series of six chapters, all dealing with different aspects of this topic.

This work has been carried out at the department of Laser-Matter Interaction of Laboratoire Hubert Curien at Université Jean Monnet (UJM), Saint-Etienne, France, in collaboration with the department of Sciences des Matériaux et des Structures of Laboratoire Georges Friedel at Ecole des Mines (EMSE), Saint-Etienne, France, from 2019 to 2022.

I would like to express my gratitude to my supervisors, Prof. Jean-Philippe Colombier (UJM) and Dr. Claire Maurice (EMSE) for their support and for always keeping me focused on the essentials during these past years. My deepest thanks go to Prof. Florent Pigeon (UJM) and Prof. Florence Garrelie (UJM) for providing and sharing advice when it was needed. I'd like to thank them all for the time they have devoted in the discussions of different thoughts and ideas and for proof-reading all my written work. It's been a pleasure working with you, and I wish and hope for further collaboration in the future.

Thanks are also to Anton Rudenko and Eduardo Brandao for their collaborations. Special thanks for my collegues, Rim, Mariam, Mathilde, Sedao and Gergess for sharing countless cups of coffee over conversations about the trials and tribulations of postgraduate studies as well as of topics beyond.

Finally, I would like to thank my family for their support and encouragement, my father Ramez Nakhoul and my mother Samar Matta for all the long distance support, my sister MD. Marie Nakhoul and her husband MD. Karl Seif for their motivation, my cat Misty for the provided tenderness during the covid containment, and my wife MD. Maria Zakhem for her love, patience, understanding and for the best PhD. gift ever, my baby girl Emily!

Saint-Etienne, October 2022

Anthony Nakhoul

Résumé

Une surface irradiée par un laser ultra-rapide est un parangon typique de système auto-organisé, qui fait émerger et organise des micropatterns complexes et même des nanopatterns. Une manifestation spectaculaire de structures dissipatives consiste en différents types de nanostructures distribuées de manière aléatoire et périodique qui émergent d'une surface métallique homogène. La formation de "nanopeaks", de "nanobumps", de "nanohumps" et de "nanocavities" avec une unité de taille transversale de 20-80 nm et jusqu'à 100 nm de hauteur est rapportée sous irradiation laser femtoseconde avec une dose d'énergie régulée. Nous montrons que l'utilisation d'une double impulsion laser à polarisation croisée ajoute une dimension supplémentaire au processus de nanostructuration. En effet, la dose d'énergie laser et la rétroaction multi-impulsions règlent la distribution du gradient d'énergie, franchissant les valeurs critiques pour les régimes d'auto-organisation de surface. La capacité de synthétiser et de concevoir des objets nanométriques hautement complexes de différentes tailles, surfaces et formes conditionne de manière spectaculaire le développement de nanomatériaux multifonctionnels. La technologie laser ultrarapide est très prometteuse en tant que processus sans contact capable de fabriquer rationnellement et rapidement des nanostructures complexes présentant des fonctions de surface innovantes. Le défi le plus critique dans le contrôle de la croissance des structures induites par laser en dessous de la limite de diffraction de la lumière est l'absence d'ordre externe associé à l'interaction locale inhérente à la nature auto-organisatrice du phénomène. Nous présentons ici des nanopatterns à haut rapport d'aspect pilotés par un couplage de surface en champ proche et architecturés par une mise en forme d'impulsions de polarisation contrôlée en temps opportun. La production de ces nanostructures distinctes peut permettre une fonctionnalisation unique de la surface pour le contrôle des propriétés mécaniques, biomédicales, optiques ou chimiques de la surface à l'échelle nanométrique. Et la nanotopographie de surface à haut rapport d'aspect obtenue devrait empêcher la prolifération bactérienne et présente un grand potentiel pour la catalyse, la photonique dans l'UV profond et la détection. Des simulations électromagnétiques couplées à des simulations hydrodynamiques révèlent pourquoi cette manipulation optique unique permet la génération de "nanopeaks" par absorption locale inhomogène soutenue par une convection à l'échelle nanométrique. En outre, nous avons utilisé l'apprentissage automatique guidé par la physique, un domaine de recherche émergent qui combine la connaissance physique et l'apprentissage automatique pour prédire de nouveaux modèles en intégrant la connaissance physique partielle sous la forme de l'équation partielle de Swift-Hohenberg. Les travaux réalisés ne font pas seulement progresser l'objectif général d'élucider le phénomène multi-échelle complexe de la formation de LIPSS, mais ils ouvrent également une nouvelle voie expérimentale pour générer des structures non conventionnelles avec des périodicités extrêmes sur différents matériaux, ouvrant ainsi de nouvelles possibilités pour la fonctionnalisation des métaux par traitement laser ultrarapide.

Abstract

Ultrafast-laser irradiated surface is a typical paragon of a self-organizing system, which emerges and organizes complex micropatterns and even nanopatterns. A spectacular manifestation of dissipative structures consists of different types of randomly and periodically distributed nanostructures that arise from a homogeneous metal surface. The formation of nanopeaks, nanobumps, nanohumps and nanocavities patterns with 20–80 nm transverse size unit and up to 100 nm height are reported under femtosecond laser irradiation with a regulated energy dose. The use of crossed-polarized double laser pulse adds an extra dimension to the nanostructuring process as laser energy dose and multi-pulse feedback tune the energy gradient distribution, crossing critical values for surface self-organization regimes. The capacity to synthesize and design highly intricated nanoscale objects of different sizes, surfaces and shapes dramatically conditions the development of multifunctional nanomaterials. Ultrafast laser technology holds great promise as a contactless process able to rationally and rapidly manufacture complex nanostructures bringing innovative surface functions. The most critical challenge in controlling the growth of laser-induced structures below the light diffraction limit is the absence of external order associated to the inherent local interaction due to the self-organizing nature of the phenomenon. Here, high aspect-ratio nanopatterns are reported driven by near-field surface coupling and architectured by timely-controlled polarization pulse shaping. The production of these distinct nanostructures can enable unique surface functionalization toward the control of mechanical, biomedical, optical, or chemical surface properties on a nanometric scale. Moreover, the obtained high aspect-ratio surface nanotopography is expected to prevent bacterial proliferation, and has great potential for catalysis, vacuum to deep UV photonics and sensing. Electromagnetic coupled with hydrodynamic simulations reveal why this unique optical manipulation allows peaks generation by inhomogeneous local absorption sustained by nanoscale convection. Furthermore, we used physics-guided machine learning, an emerging field of research that combines physical knowledge and machine learning to predict novel patterns by integrating partial physical knowledge in the form of the Swift-Hohenberg partial equation. The carried work not only advances the general goal of elucidating the complex multi-scale phenomenon of LIPSS formation, but it also opens a new experimental path to generate unconventional structures with extreme periodicities on different materials, opening up new possibilities for ultrafast laser processing functionalization of metals.

Contents

List of Figures

List of Tables

Acronyms

LIPSS	Laser-Induced Periodic Surface Structures
LSFL	Low-Spatial Frequency LIPSS
HSFL	High-Spatial Frequency LIPSS
nf	Near-Field
ff	Far-Field
TTM	Two-Temperature Model
MD	Molecular Dynamics
AFM	Atomic Force Microscopy
EBSD	Electron Back-Scattered Diffraction
SEM	Scanning Electron Microscopy
SE	Secondary Electrons
FEG	Field-Emission Gun
TEM	Tranmission Electron Microscopy
STEM	Scanning TEM
ADF	Annular Dark Field
BF	Bright Field
DF	Dark Field
FIB	Focused Ion Beam
FDTD	Finite-Difference Time-Domain
FFT	Fast-Fourier Transform
XR	X-rays
UV	Ultraviolet
IR	Infrared
CPA	Chirped Pulse Amplification
WDM	Warm Dense Matter
EOS	Equations Of State
GND	Geometrically Necessary Dislocations
SPP	Surface Plasmon Polaritons
N_{DPS}	Number of Double-Pulse Sequence
Ra_{th}	Arithmetical Mean Roughness Threshold
TFP	Thin Film Polarizer
Ku	Kurtosis
ML	Machine Learning
SH	Swift-Hohenberg

Introduction

Background

Femtosecond laser sources allow to explore the materials behavior under swift photoexcitation. This represents a privileged way to bring material surfaces in extreme states of temperature and pressure far from equilibrium. During the relaxation stage, out-of-equilibrium systems usually exhibit pattern formation as a result of spontaneous spatial breaking symmetry of the initial homogeneous state [1]. In particular, ultrashort laser energy deposition induces local thermal stresses and transient phase changes which modifies materials microstructures and topography [2, 3]. The fast interaction with material surfaces results in the formation of anisotropic surface morphology, usually recognized as laser-induced periodic surface structures (LIPSS) or ripples. LIPSS are a special type of arranged nanopatterns, known with their periodicity varying from near laser wavelength down to sub-100 nm scale [4]. These structures can alter wetting [5], tribological, and optical characteristics [6]. Laser-induced textures provide hydrophobic [7], antimicrobial [8], colored [9], and wear-resistant surfaces [10]. Their formation is generally occurring in multi-pulse irradiation regime with a fluence below the ablation threshold. Consequently, the first laser pulse modifies the surface topography randomly by creating roughness centers that are perceived by the next pulses. All the consecutive laser pulses impact on a surface being constantly modified by the previous pulses and being roughened constantly, from an initially quasi-flat surface to transiently growing disturbances. LIPSS can be generated with different periodic scales by virtue of the radiative and nonradiative modes of light coupling, which involves polarization effects on the freshly formed roughness centers [11]. Far beyond the diffraction limit, most of the sub-wavelength structures are oriented by the laser polarization, commonly spaced between 50-200 nm in the literature and a priori provoked by local field enhancement on the local roughness [12, 13]. They are generally called high spatial frequency LIPSS (HSFL) of type r in the literature [14]. The light coupling is composed of scattered waves but also of nonradiative fields that emerge from nanoreliefs and that generate coherent exchanges of optical near fields [15]. Strong enhancement of the oriented electromagnetic field at surface defects trigger local heat confinement that can destabilize the thin laser-induced melt layer. During the sub-surface rarefaction process, periodic nanovoids enclosed under the surface and nanocavities emerge at the surface by cavitation [16]. During the acceleration of the molten surface by the rarefaction wave, a Marangoni-convection instability can be triggered by hydrothermal waves perpendicular to these temperature gradients [17], forming high spatial frequency periodic surface structures.

Furthermore, it was observed that under multi-pulse feedback regimes, there is a strong dependence of the generation of surface roughness and finally periodic nanoripples on the crystallographic surface orientation [2]. More refined nanostructure was obtained on Cr (100) by a single pulse irradiation and a more pronounced LIPSS after two laser pulses as compared to (110) surfaces [18]. The competition between the evolution of transient liquid structures generated in the spallation process and the rapid resolidification of the

surface region were proposed to define the types, sizes and dimensions of the nanoscale surface features [18]. Thus, the formation of sub-100nm nanopatterns are clearly dependent on crystallographic orientation and initial surface roughness. Recent investigations show that two orthogonal linear polarization states can cancel polarization dependence of nanopatterns alignment. Controlling ultrafast laser pulse polarization, inter-pulse delay, and laser fluence creates unique 2D surface morphologies. Several studies focused on near-submicron 2D-LIPSS have revealed the appearance of rhombus, triangle and spherical structures on cobalt [19], while others have reported triangular and square nanostructures by using double linearly crossed polarized and counter-rotating circularly polarized pulses on stainless steel with a time-delays in the picosecond range [20]. These periodic nanostructures were created by scanning the surface and have a periodicity close to the laser wavelength. However, none of these studies have reported such symmetry features at the nanoscale.

Problem definition

Driven by near-field light enhancement, periodic patterns have reached ultimate sizes of tens of nanometers on a (001)-oriented Nickel surface. A self-organizing array of nanocavities with a diameter of 20 nm and a periodicity of 60 nm was developed by a new technique by delaying cross-polarized laser pulses, this technique overcomes the anisotropic polarization response of the surface, allowing for self-arranged nanoscale topography in advanced technological areas [21, 22]. This work explores the creation of previously unseen nanopattern morphologies controlled by different energy doses, all well below the diffraction limit. We address the laser irradiation settings and material circumstances suited to induce nanostructuring self-organization. Under ultrafast excitation, a homogenous metal surface forms disordered, nanopeaks, nanohumps, nanobumps and nanocavities patterns as presented in Figure 1. Irradiation conditions defined by peak fluence, time-delay, and the number of double-pulse sequences have a key role to select competing surface patterns by sequentially fostering emergence, growth, amplification, and regulation of pattern development. The degree of instability of such patterns is so high that the nanostructure shape organization can be altered by a delay change of a few picoseconds. These states are characteristic of attractors toward which the dynamical system tends to evolve in dissipative structures. The door is open to describe mathematically the nonlinear dynamics of laser-induced surfaces with models able to reproduce the variability of the patterns in the phase space and explore the origin of bifurcations.

Outline

This thesis was performed at Hubert-Curien laboratory, Saint-Etienne, France in collaboration with Ecole nationale supérieure des Mines de Saint Etienne (EMSE), in the frame of MORPHOSURF project, labeled by EUR MANUTECH of Lyon University. The experimental work for surface preparation was performed at Laboratoire Georges Friedel of EMSE and the experimental work for laser irradiation was supported by the laser-matter interaction

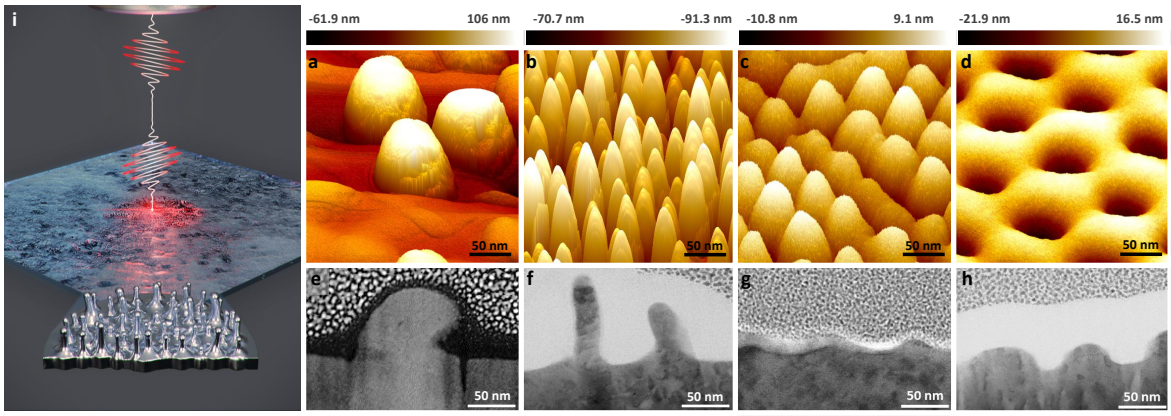

Figure 1: 3D atomic force microscopy of the nanobumps (a), nanopeaks (b), nanohumps (c) and nanocavities (d) presenting the nanostructures height and distribution. (e-h) Transmission electron microscopy of the principal nanstructures presenting the cross view of nanostructures. (i) Schematic illustration of nanopeaks formation by femtosecond laser double pulse.

group in Laboratoire Hubert Curien. This work enabled access to different characterization microscopy: Scanning Electron Microscopy (SEM), Atomic Force Microscopy (AFM) were performed at both laboratories, which allowed topographical investigation of laser induced-roughness and LIPSS morphology. Thin lamellas extraction as well as in-depth characterization were carried out at Manutech by Stéphanie Reynaud employing focused ion beam and the transmission electron microscopy. Physico-chemical analysis was performed at Manutech by Alina Hamri to identify the contribution of nanoscale texturing to surface functionalization. Finally, antibacterial tests were performed on textured samples by Steve Papa.

For theoretical analysis, a collaboration was made with the University of Arizona, where Anton Rudenko performed hydrodynamic simulations on the observed laser-induced periodic surface structures. Moreover, non-linear dynamics calculations were performed at the Hubert-Curien laboratory by Eduardo Brandao.

In chapter 1, we review an up-to-date state of the art linked to the fundamental processes between ultrashort laser and matter, the case of metals being specifically considered. We start by introducing the femtosecond laser sources, their characteristics and potentials. The mechanisms of laser interaction with metals is discussed and different LIPSS formation approaches are explained. It exposes different scenarios leading to the formation of laser-induced periodic surface structures, such as electromagnetic, hydrodynamic, chemical and self-organisation approaches. Finally, 2D LIPSS are classified and discussed, periodic nanostructures on the scale of tens of nanometers will be exposed and discussed in the following chapters.

Chapter 2 starts with describing different techniques for sample preparation as well as the experimental setup for double-pulse sequence generation. This entails producing femtosecond pulses of energy close to a millijoule via the laboratory's laser equipment, with double-pulse train generation using a Mach-Zehnder interferometer. The Liu method for

determining laser fluence is also explained. Atomic force microscopy (AFM), scanning electron microscopy (SEM), and transmission electron microscopy (TEM) are also employed to analyze LIPSS and nanostructures features. Finally, physico-chemical analysis is performed to identify the hydrophilic or hydrophobic character of the irradiated Ni sample, and antibacterial adhesion analysis is also performed on irradiated Ti samples.

In chapter 3, our work demonstrates the potential of ultrafast laser for the fabrication of unconventional self-organized periodic nanopatterns with a sub-100 nm periodicity, such as nanobumps, nanohumps, nanopeaks, nanocavities, nanobreath-figure, nanocrosshatch and nanolabyrinthe. In an elegant way, the control of fluid flows on the nanoscale by laser irradiation is demonstrated by tuning laser processing parameters. This will bring new fundamental ideas to communities of photonics, laser-matter interaction, and fluid dynamics.

Chapter 4 evokes the capacity to synthesize and design highly intricated nanoscale objects of different sizes, surfaces and shapes. Here we report high aspect-ratio nanopatterns driven by near-field surface coupling and architectured by timely-controlled polarization pulse shaping. We study the multipulse dynamics of nanopeaks generation and we show how their aspect-ratio and distribution can be controlled by laser processing parameters. The obtained high aspect-ratio surface nanotopography is expected to prevent bacterial proliferation, and to have great potential for catalysis, vacuum to deep UV photonics and sensing.

Chapter 5 supplements our comprehension on the dynamics of self-organised nanostructures formation. Electromagnetic coupled with hydrodynamic simulations are performed to reveal why this unique optical manipulation allows peaks generation by inhomogeneous local absorption sustained by nanoscale convection. Moreover, we use non-linear dynamics and physics-guided machine learning, an emerging field of research that combines physical knowledge and machine learning to predict novel patterns by integrating partial physical knowledge in the form of the Swift-Hohenberg partial equation. The work carried out not only advances the general goal of elucidating the complex multi-scale phenomenon of LIPSS formation, but it also opens a new experimental path for generating unconventional structures with extreme periodicities on different materials, opening up new possibilities for the functionalization of metals by ultrafast laser processing.

In chapter 6, we perform different types of characterization to optimize surface functionalization at the nanoscale. Physico-chemical analysis of textured Ni sample reveals a slight improvement of the surface hydrophobia. Moreover, the nanotextured Ti samples show a great potential in manufacturing antibacterial surfaces, which opens the doors for future works in this field.

Finally, the main results and conclusions are summarized, paving the way towards future research suggestions.

Part I

State of the art

Chapter 1

Ultrafast laser-matter interaction in metals

Among the many driving forces behind technological advancement, two stand out the most: A curious mind, and a persevering heart

– Karl Edward Seif

In this chapter, we review an up-to-date state of the art linked to the fundamental processes between ultrashort laser and matter, the case of metals being specifically considered. We start by introducing the femtosecond laser sources, their characteristics and potentials. The mechanisms of laser interaction with metals are discussed, and different LIPSS formation approaches are explained. It identifies different scenarios leading to the formation of laser-induced periodic surface structures, such as electromagnetic, hydrodynamic, chemical and self-organisation approaches. Finally, 2D LIPPS are classified and discussed. Periodic nanostrucutres on the tens of nanometers scale will be exposed and discussed in the following chapters.

1.1 Femtosecond laser sources

Ultrashort laser pulses, which are renowned for their high intensities and short pulse durations, are increasingly studied in disciplines employing micron and submicron textures as well as surface functionalization issues. The choice of laser (picosecond / femtosecond) as well as its parameterization and the type of targeted material permits modulation of the multiscale structures that can be obtained. The distinguishing characteristic of ultrashort pulse lasers is that the pulse duration is shorter than the electrons' cooling time. Therefore, the material is preserved and not harmed by the high ablative energy to which it is exposed.

1.1.1 Brief history

T.H. Maiman realized the first ruby-based laser in 1960 [23], concretizing several theoretical and experimental works on light amplification, optical pumping, and the development of adapted cavities. Many devices have been developed since then with the goal of improving laser mode synchronization and decreasing pulse duration. Most modern lasers use four atomic energy level amplifiers (as opposed to three for the Maiman laser) to optimize population inversion and amplification performance. Modulating the amplitude or phase of a transmitted wave can achieve mode synchronization, a critical component in the evolution of laser systems. Thus, many combinations were tested for years before the CPM (Colliding Pulse Mode-locked dye laser) with Fork appeared in 1981, allowing mode synchronization via pulse collisions. Treacy and Fork's work on optical compressors in 1969 and 1987, respectively, significantly reduced the duration of a typical pulse, reaching 6 fs. Simultaneously, significant progress has been made in expanding emission frequency ranges. Lasers can now emit a wide range of wavelengths, from X-rays (XR) to ultraviolet (UV) to infrared (IR) [23]. The table 1.1 lists the various types of lasers, as well as the date they first appeared and their main characteristics, such as the type of active medium used and the wavelength, energy, and pulse duration ranges. The use of aluminum oxide doped with titanium as an amplifying medium has allowed a considerable reduction in pulse durations. Finally, very recently, the team of Gérard Mourou (Nobel Prize in Physics 2018) has developed a technique called CPA (Chirped Pulse Amplification) to amplify and compress a nanosecond pulse [24].

L.A.S.E.R. stands for **L**ight **A**mplification by **S**timulated **E**mission of **R**adiation. In or-

Laser Type	Amplifying Medium	Emission Range (nm)	Energetic Range	Pulse Duration	App. Date
Gas	Nitrogen	337	1 to 100 mJ	100 ns	1964
Gas	Excimer	190 to 350	1 to 300 mJ	10 to 60 ns	1971
Gas	Helium, Neon	632	0.1 to 100 mW	Continuous	1961
Gas	CO_2	10600	1 W to 50 W	10 to 100 ns / Cont.	1964
Solid	Ruby	694	0.1 to 10 J	30 ns / 500 µs	1960
Solid	Nd : YAG	1064	0.1 mJ to 50 J	30 ps to 30 ns	1964
Solid	Ti : Al_2O_3	370 to 3000	0 to 0.2 J	< 80 fs	1982
Liquid	Dye	350 to 1000	mW to W	Continuous	1966

Table 1.1: Main types of laser and their characteristics

der to function, it requires the generation of a first pulse thanks to a resonant cavity often delimited by two mirrors, one of which is semi-reflecting. This cavity is characterized by its "longitudinal modes", i.e. the wavelengths generated by the numerous round trips between the mirrors formed and constructed by constructive interference. For the operation of a conventional laser oscillator, the longitudinal modes oscillate without any specific link between them. In the case of a femtosecond oscillator, the different modes are out of phase by a defined phase value which allows their superposition (or cancellation). Thanks to this fixed phase shift, it is possible to generate pulse duration being inversely proportional to the frequency range. This is what makes the specificity of these mode-locked lasers [23, 25, 26]. To select this femtosecond pulse, non linear optical phenomena are exploited (e.g. Kerr effect or Pockels effect) [27]. This pulse is then stretched, amplified (often by a CPA system [24]) and then compressed again as shown in Figure 1.1.

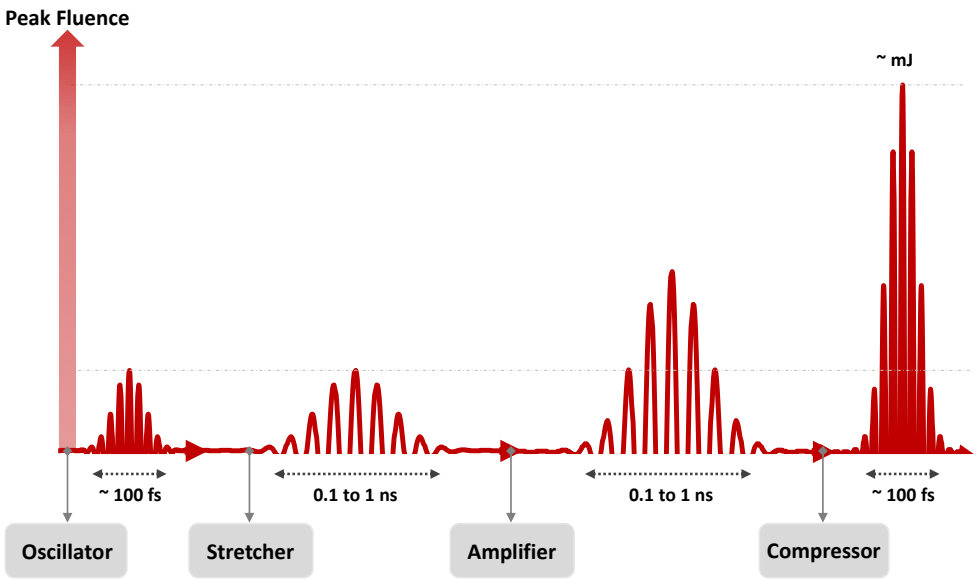

Figure 1.1: Simplified diagram of the complete femtosecond laser system, composed of an oscillator, a stretcher, an amplifier (CPA type) and a compressor.

1.1.2 Characteristics and potentials

The irradiation of materials by ultrashort laser pulses makes it possible today to shape structures on various supports, and this for complex forms. The surface offers a promising topography to functionalize optical, mechanical or electronic systems. Figure 1.2 illustrates some of these functionalizations, most of them realized within the Hubert Curien Laboratory (LabHC). Some structures can reach characteristic dimensions of the order of a few hundred nanometers, which makes it possible to consider new optical signal processing for wavelengths ranging from the visible to the near infrared. Also, it is possible to trap the light on the surface (Figure 1.2) (b,c) or in the volume (Figure 1.2) (a,d) of a support thanks to micro-structuring techniques, and to make the photons interact in a controlled way with the material, in order to obtain original physical conditions. Singular morphological properties have also been observed at the nanoscale of irradiated solids, resulting from complex photon excitation followed by growth dynamics inducing various equilibrium forms [28, 29]. This sub-micron structuring has a strong applicative potential since it is possible to shape structures of various geometries (cavities, cutting, marking, surface wrinkles. . .), thus offering a complex topography of the surface and giving rise to numerous applications (tribology, wettability, anti-counterfeiting. . .).

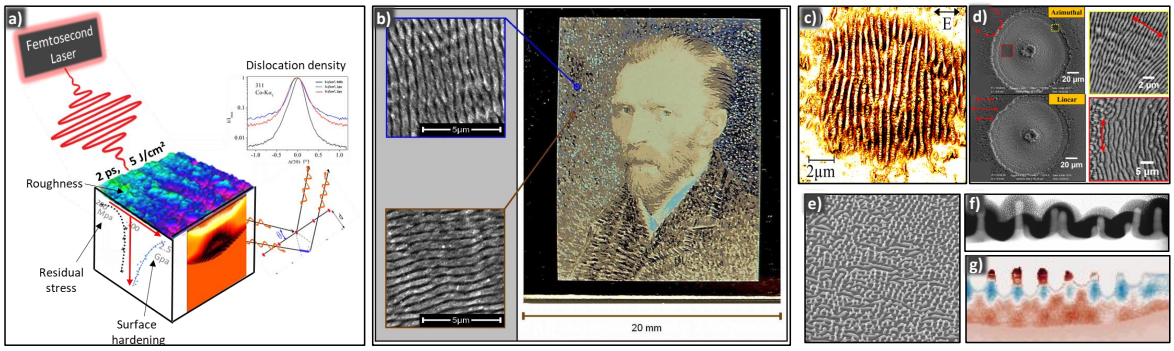

Figure 1.2: Some examples of ultrashort-matter laser applications. a) Surface integrity modification by ultrafast laser pulses [30]. b) Colored marking visualized through its diffractive effects by a controlled nanostructuring on stainless steel surface [31]. c) Ripples obtained on tungsten surface after 80 pulses of 50 fs [32]. d) Surface morphologies on a silicon wafer irradiated by azimuthal and linear polarization [33]. e) Forest of high aspect ratio nanopeaks irradiated by orthogonal polarization, presenting a cross sectional view on TEM (f) and an electromagnetic coupled with hydrodynamic simulation presenting this unique nanostructures (g) [34].

The control of structuring processes requires to master the excitations involved, especially the phenomena involving optical resonances such as plasmons on the surface of the material. From a physical point of view, the originality and the potential of applications linked to femtosecond technologies result from the possible control of the material reaction along excitation and relaxation paths (electronic, atomic, thermal, mechanical, structural), with the consequence of a precise control of the structuring mechanisms [29]. As presented in Figure 1.2 (a), ultrafast laser was recently used to modify the surface integrity and peen the surface region of aluminum based alloy 2024-T351 without a sacrificial layer prior to

the process. It was shown that controllable laser parameters such as fluence and pulse duration have a significant influence on peening qualities, such as the compressive residual stress, hardness, and surface roughness of peened parts [30]. Moreover, micro-hardness was increased from 2.1 to 2.5 GPa in the near-surface region. The obtaining of micro- and nanostructures is intimately related to the energy confinement, to the limited thermal character of the interaction and to a preferential transformation of the material states. These characteristics influence not only the direct structuring possibilities but also the applications related to nanosurgery, nanoparticles generation or spectroscopic purposes.

1.2 Mechanisms of laser interaction with metals

1.2.1 Mechanisms driving laser ablation

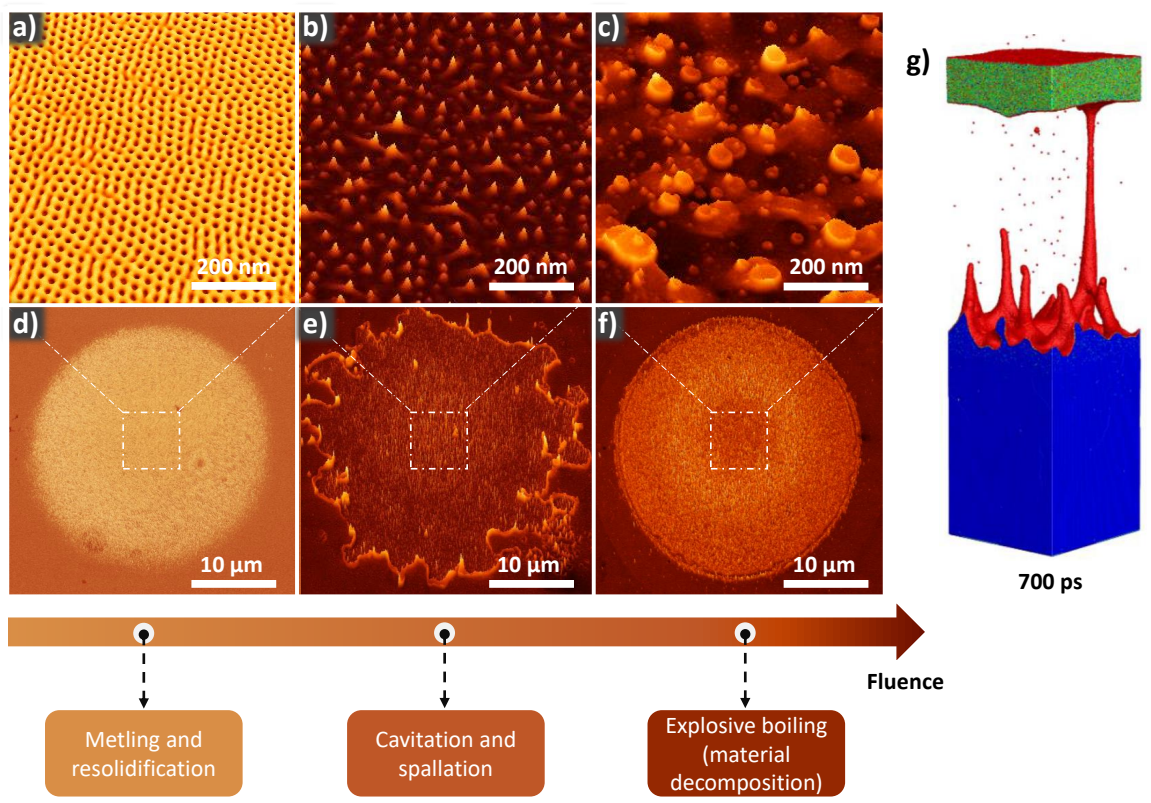

Figure 1.3: Mechanisms driving laser ablation as a function of the fluence. For sub-spallation fluences, the system experiences melting and resolidification (a, d). In the case of sub-phase explosion regime, cavitation of the melting region leads to ejection of a liquid layer from the surface of the target (b, e, g). Increasing the fluence above the phase explosion will eject multiple liquid layers and lead to ablation of the material. (g) Molecular dynamics simulation illustrating the evolution of the surface of a material irradiated by ultra-short laser, adapted from [18].

Structure changes can occur depending on the temperature reached by the material

(melting temperature, evaporation temperature, etc.). The energy deposited on the surface by the irradiation is transmitted to the lattice and converted into kinetic energy, which can lead to the ejection of materials and particles. This is known as the laser ablation phenomenon [18, 35]. Figure 1.3 (a-f) depicts various mechanisms leading to ablation as a function of the irradiation fluence. They are mainly melting and resolification, cavitation and spallation phenomena or material decomposition by explosive boiling. Figure 1.3 (g) shows a zone of a metallic material irradiated by an ultrashort laser, it was obtained using a standard molecular dynamics simulation [18]. Some of the mechanisms leading to ablation are illustrated as a function of the simulation time, as well as the orders of magnitude of the dimensions of the affected layers and the ablated elements.

Many different types of topographic changes can occur on the surface of the irradiated material as a result of these different mechanisms leading to material ablation, depending on the different categories of materials.

1.2.2 Absorption by a metal

To enable a laser metal processing application, the electromagnetic energy of the laser light must be converted into thermal energy within the metal. Mechanisms of light absorption within the metal determine the amount of energy transformed. This "secondary" type of energy, the absorbed energy, rather than the laser beam itself is available for heating the metal and producing the desired effect, such as nanostructuring, cutting, welding, and so on. Laser absorption in a metal is affected by a variety of factors involving both the laser and the metal. The wavelength of the light, the angle with which the beam impinges on the metal surface, the pulse duration, and the polarization of the beam, which is related to how the electric field in the light wave is oriented, are the main laser parameters of importance. It can also be affected by the intensity, which is a combination of the laser beam's intensity and focal spot size in some cases. The composition of the material, whether a pure element (such as copper, iron, aluminum, etc.) or an alloy (such as brass or steel), is the primary material parameter determining the amount of absorbed light. Light always interacts with the electrons inside the metal or alloy, regardless of composition, because light is an electromagnetic wave and electric and magnetic fields only interact with charged matter. The electric field will accelerate the electrons, and energy will be transferred to the lattice through various collisions with the other constituents of the metal.

The metal will heat up as energy is transferred to it, and as the temperature rises, the amount of absorbed light may change because both the electrons and the lattice atoms in the metal gain kinetic energy, which influences the collision frequency. Absorption is also strongly influenced by the surface properties of the metal or alloy. Most actual surfaces are not perfectly flat (even mirror polished) and have varying degrees of texture and roughness that affect their optical behavior. Pits and valleys, for example, may "trap" some of the light and thus increase absorption. Metals naturally have a layer (or layers) of oxides on their surface, and the chemical and optical properties of the oxides can often differ significantly from the properties of the metal or alloy beneath. We may then encounter a situation in which the light is "caught" by the oxide layer, increasing absorption even further. Finally, contamination such as dirt, oil, or dust alters the absorptive potential of a metal surface.

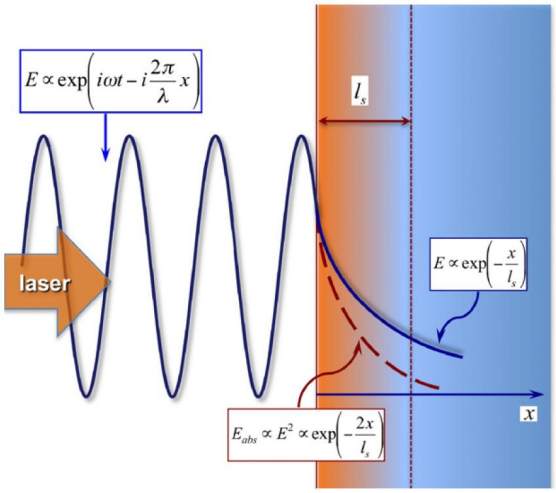

Figure 1.4: Laser electric field E penetration into the solid in normal skin effect; the absorbed laser energy $E_{abs} \sim$ T $\sim$ E². Adopted from [36].

This can include substances left over from previous processing steps (such as polishing or finishing), from handling, or even from the fabrication of the metal or alloy itself.

We are primarily interested in interactions with highly absorbing media. The relationship between the absorbed intensity (I_{abs}) and the incident intensity (I_0) in laser surface interaction can be expressed as: I_{abs} = (1 - R) $\times$ I_0, where R is the reflectance, which is the fraction of the incident intensity that is reflected off the surface of the material. The reflectance is typically determined experimentally or by using theoretical models, and it depends on various factors such as the laser wavelength, the angle of incidence, the polarization of the light, and the optical properties of the material. The laser energy is absorbed in a thin layer called the skin layer l_s, which has a typical thickness of several tens of nanometers and is much smaller than the focal spot's diameter. For ultrafast photoexcited Nickel, we estimate that the skin depth is $\delta = 2l_s = 18$ nm for an estimated average temperature of $T_e = 10000$ K [37].

1.2.3 Description of the transient state of the material

The power of ultrashort lasers generates and modifies the population of free electrons in the conduction band of the material. The speed with which the material is excited prevents it from relaxing by thermal expansion and thus allows isochore heating of the free electrons remaining degenerated at high density. Indeed, the heated surface layer has a typical thickness of the order of the skin thickness, i.e. about 10-20 nm for most metals. The displacement of this surface layer during 100 fs is given from the expansion velocity, close to the speed of sound in the solid ($\simeq$ 5000 m.s^{-1}), or by $\nu_s = \sqrt{\gamma_e N_e \kappa_B T_e / M_i}$ in a plasma hypothesis, where M_i is the mass of the ion, N_e the number of free electrons per atom and γ = 3 the adiabatic constant in a solid [36]. Figure 1.5 (a) illustrates the features of the thermodynamic regime achieved in the applications of interest. In this work, we are focusing on the LIPSS formation regime after solid-liquid transition. We specifically do not exceed

a T_e temperature of 3 eV in our experiments (< 2 J/cm²). The majority of the processes that we are interested in can be controlled by varying the pulse's temporal duration by a few tens of picoseconds. On this time scale, the surface relaxes and approaches the critical density. The zone corresponding to the formation of laser-induced periodic surface structures (LIPSS) is located at the solid-liquid transition and is not expected to extend beyond the liquid-gas binodal line at this time.

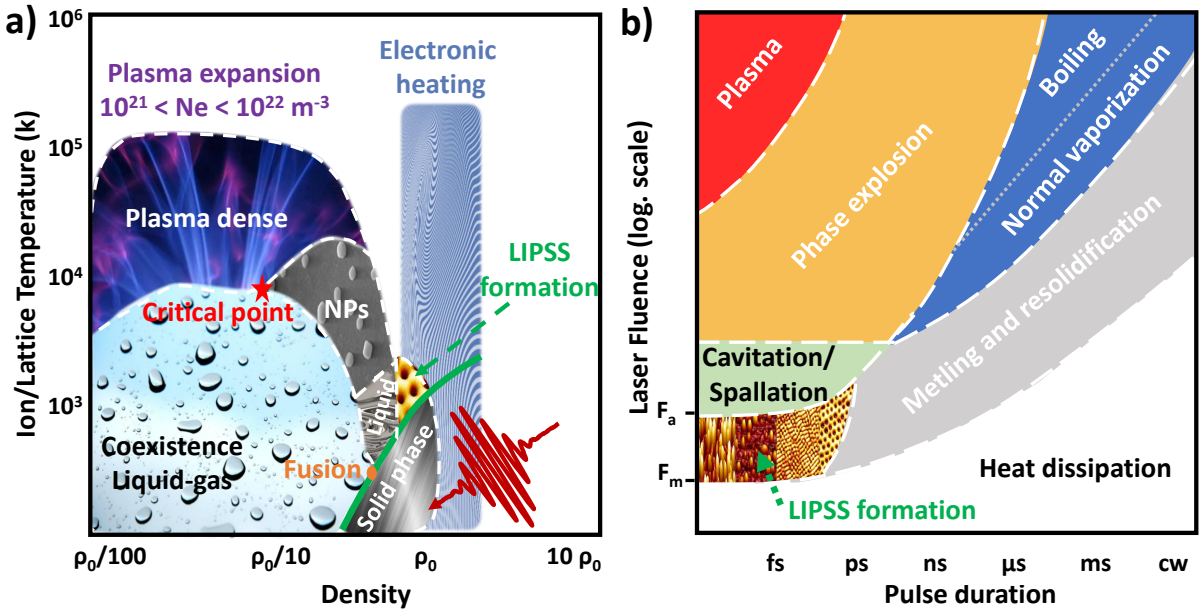

Figure 1.5: a) Thermodynamic diagram representing the transient phases reached by the material, as a result of an ultrashort laser irradiation. The zone of interest in this work is where LIPSS formation occurs after solid-liquid transition. b) Schematic diagram illustrating manifestation of thermal processes at laser fluences typical for material processing as a function of pulse duration [38].

Furthermore, thermal processes are responsible for both macro- and microscopic structural modification of materials at all stages of laser-material interactions. Figure 1.5 (b) depicts a schematic representation of some of the major laser-induced thermal processes as a function of pulse duration and laser fluence. The actual boundaries for these processes' onsets are strongly influenced by the thermophysical, optical, and mechanical properties of irradiated materials. For example, despite the high reflectivity of metal surfaces, which reduces the absorbed energy dose, relatively low laser energy densities are typically required to cause metal damage, such as melting and ablation. However, wide-bandgap inorganic dielectrics and polymers, despite being low reflecting materials, require significantly higher laser fluences than metals to achieve melting and/or ablation [38].

Controlling the laser fluence allows for the creation of different material regimes at the same pulse duration. For example, with a femtosecond laser pulse, we can progress from LIPSS formation to cavitation/spallation, phase explosion, and plasma simply by increasing the fluence. In this work, we are mainly focusing on the LIPSS formation regime which is between the melting (F_m) and ablation (F_a) fluences threshold, just before cavitation and spallation occur.

Electron and ion temperatures: Two-temperature model

Understanding the phenomena of laser-matter interaction and all related mechanisms (cavitation, spallation, ablation, etc.) is required to study and comprehend the topographic and structural changes caused by ultrashort laser irradiation. The light absorption mechanisms during ultrashort laser irradiation of a material are strongly dependent on the nature of the material and the fluence deposited on the surface. A solid material is a lattice of atoms that are more or less strongly bound to the electrons that surround them. In the case of a metal, the quasi-free electrons will receive the energy deposited by photon absorption in a matter of ten femtoseconds. Their relaxation can last up to ten picoseconds. After accumulating energy, free electrons transfer it to the ion lattice through collisions (electron/phonon coupling) until the material reaches thermodynamic equilibrium. The pulse duration is typically shorter than the thermalization time, resulting in an imbalance between the two systems that comprise the material lattice, free electrons and ions. The TTM (Two Temperature Model) developed in 1974 [39, 40] governs the evolution of these two systems, which are characterized by these two coupled energy transfer equations.

The power of ultrashort lasers changes the band spectrum of the irradiated solids and generates a population of free electrons in the conduction band of insulating materials or strongly modifies that of metals. The rapidity with which the material is excited prevents it from relaxing by thermal expansion and thus allows an isochore heating of the free electrons remaining degenerated at high density. The electromagnetic stress is such that the electrons are strongly excited at electron temperatures much higher than the ionic temperature. The time necessary for the relaxation of the electron energy towards the crystal lattice is then several picoseconds.

$$C_e \frac{\partial T_e}{\partial t} = \frac{\partial}{\partial z}(k_e \frac{\partial T_e}{\partial z}) - \gamma(T_e - T_i) + S(z,t) \tag{1.1}$$

$$C_i \frac{\partial T_i}{\partial t} = \gamma(T_e - T_i) + \frac{\partial}{\partial z}(k_i \frac{\partial T_i}{\partial z}) \tag{1.2}$$

The different terms of these equations represent:

- C_e and C_i: respectively are the volumetric heat capacities of ions and electrons.
- T_e and T_i: respectively are the electronic and ionic temperatures.
- k_e and k_i: respectively are the thermal conductivities of electrons and ions.
- S: is the heat source term corresponding to the incident laser energy.
- γ: is the electron-phonon coupling coefficient.

Collisions between electrons and the lattice transfer energy, causing an increase in system heat and, as a result, various thermal phenomena, depending on the deposited laser energy and thermodynamic properties of the material. However, "non-thermal" phenomena can occur, but these are the majority of the cases that will not be developed.

1.2.4 Nanostructures induced by field scattering

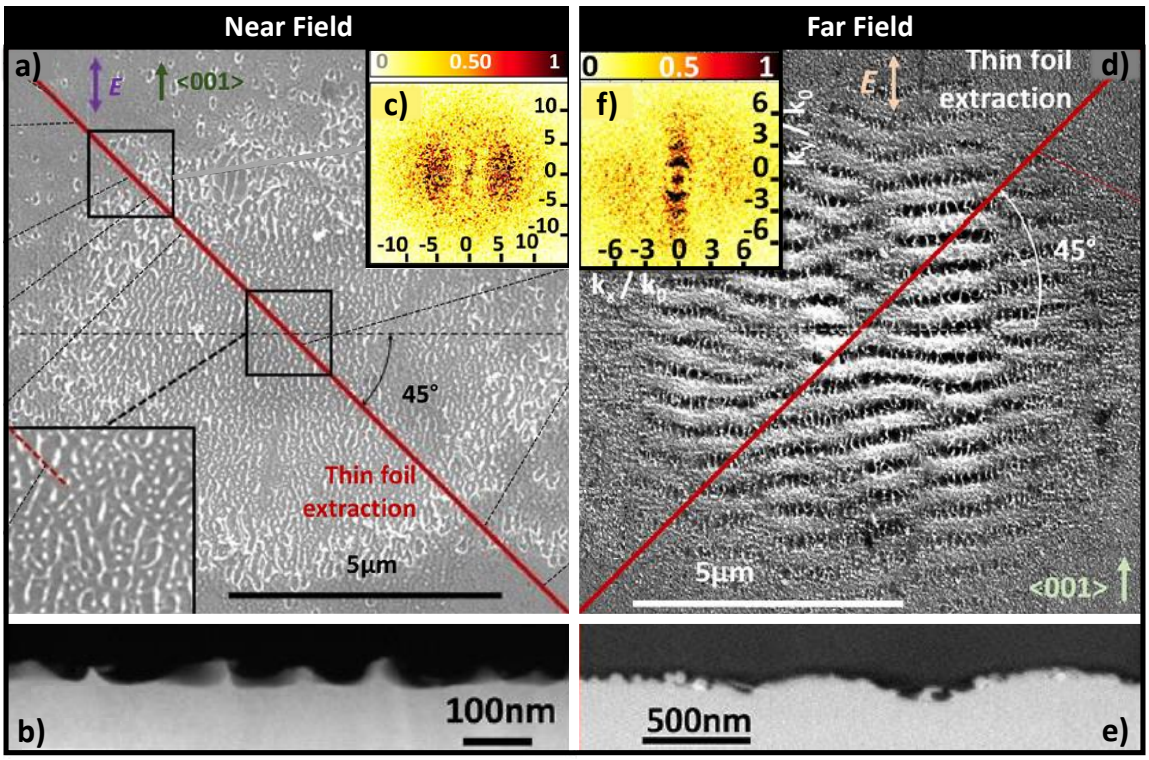

Figure 1.6: Near field (nf) (a) and far field (ff) (b) nanostructures produced on Ni(100) surface after fs-laser irradiation at near-threshold fluence, peak fluence 0.38 J/cm², 2 pulses for (a-c) and 0.19 J/cm², 46 pulses for (d-f). (a, d) SEM image of the central area, with notations of laser polarization (E), crystal direction (001). (b, e) HAADF images of TEM thin foil extraction, presenting nf in (b) and ff in (e). (c, f) FT spectrum of the SEM images. The two lobes indicate $nf_{\parallel}$ frequency distribution in (c) and $ff_{\perp}$ features in (f). Adapted from [41].

Recently, several studies have been conducted on laser-induced field enhancement [16, 18]. Far field and near field features are presented in the Figure 1.6 based on different laser conditions, and were then subjected to high resolution microstructural analysis. A single laser pulse does not cause significant surface modification near the ablation threshold fluence, but two pulses do. Figure 1.6 (a) depicts the production of $nf_{\parallel}$ features by two laser pulses at near ablation threshold fluence. Spallation removes matter from a tiny central area of the laser spot, and $nf_{\parallel}$ formation occurs. The SEM image shows a top view of the central area. Figure 1.6 (b) highlights the $nf_{\parallel}$ structures and the rim of the spallation crater in the center. Spallation is caused by the relaxation of laser-induced stresses generated beneath the surface, which coincides with the nucleation, growth, and coalescence of multiple voids. The SEM image determines the central periodicity of $nf_{\parallel}$ = 145 nm, which is confirmed by FT analysis in Figure 1.6 (c).

Moreover, additional experiments were conducted with a high number of pulses and a low incident laser fluence near the melting point, as positive feedback conditions of irradiation are the most commonly used regime of LIPSS formation. Figure 1.6 (d-f) depicts

surface and cross-section examinations of a laser impact with parallel and perpendicular coexistence, performed at 0.19 J/cm² and 46 pulses. It is presumed that near-field enhancement was required at first to localize the laser energy, and that the interference effect resulted in $fff_{\perp}$ formation later on as presented in Figure 1.6 (e). The SEM image (Figure 1.6 (d)) shows the spot center, with both parallel and perpendicular structures clearly visible in a 5 µm radius area. The FT in Figure 1.6 (f) sums up the spatial alignment and periodic features of these ff structures.

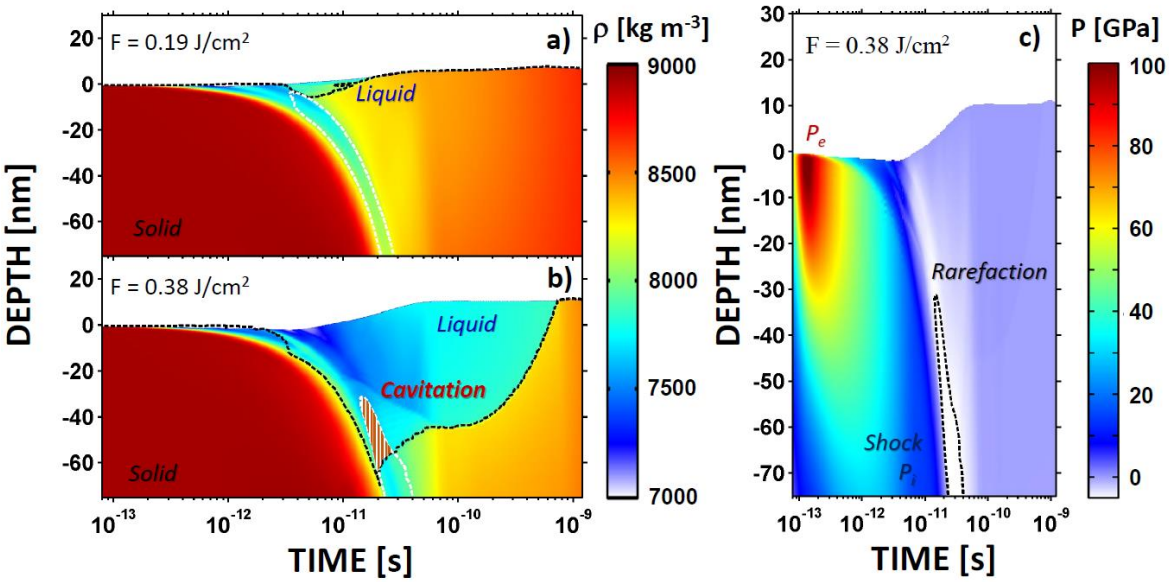

Figure 1.7: Spatiotemporal evolution of material density (a, b) and total pressure (c) calculated by a hydrodynamic simulation of a Ni sample irradiated with a 60 fs laser pulse at an incident fluence of 0.19 J/cm² (a) and 0.38 J/cm² (b-c). The black dashed lines indicate the solid-liquid interface for density evolution and the tensile strength limit for pressure diagram (c). Melt fracture is supposed to occur when the material experiences a high tensile stress in a liquid state as represented by the red hatched area in (b). Adapted from [16].

Molecular dynamics and hydrodynamic simulations have previously described the nucleation and cavitation processes in a stretched metastable system. [42–44]. It has been demonstrated, particularly for metals, that the dynamics of the laser-induced bubbles can affect the outer-surface relief on the spalled layer because the surface tension force can reach the same order of magnitude as the inertia force [45]. The 2T-hydrodynamics code Esther was used to investigate the response of a Ni surface to ultrashort laser pulse heating [29, 46], to simulate the appearance of tensile stresses subsequent to the unloading of thermomechanical stress created by the ultrafast laser heating. Following laser excitation in a sub-ablation regime, the one dimensional in-depth calculation of the successive thermodynamic states defines the energy, density and pressure distributions for both electrons and ionic species inside the material.

The investigated fluences are 0.19 J/cm² and 0.38 J/cm², which correspond to Figure 1.6 experimental conditions as well as melting and ablation fluence thresholds. Figure 1.7 depicts the spatiotemporal dynamics of material density and total pressure, including electron

and lattice contributions. A thin liquid film of 5 nm thickness is formed at the surface between 3 ps and 18 ps for the lower fluence (Figure 1.7 (a)). It means that a second pulse can affect the material response as long as the surface remains liquid. However, the liquid layer is thicker, up to 60 nm, for the single-pulse higher fluence shown in Figure 1.7 (b), and resolidification occurs at around 750 ps. This depth corresponds to the surface relief shown in Figure 1.6 (a-c). Figure 1.7 (c) shows early thermomechanical excitation of electrons in the first picosecond, followed by shock propagation deeper into the solid at a maximum pressure of 12 GPa. The abrupt drop in pressure generates two rarefaction waves that propagate in opposite directions, causing local tensile stress and potentially nucleation and cavitation processes.

Mesoscopic aspects: influence of crystal orientation

Another study by Sedao et al. on the effect of the crystalline orientation of the irradiated material on the formation of LIPSS for polycrystalline nickel samples has also been published [2]. This original work explains the inhomogeneity of structures formation on the surface of a metal irradiated by a low number of pulses. This locally non-uniform formation is due to the singular responses of the different crystalline orientations present on the surface. Figure 1.8 shows some results obtained in this work where the comparison of SEM (a) and EBSD (b) taken on the same irradiated nickel sample clearly shows a disparity of structuring depending on the grain considered. The lower part of the laser impact corresponds to an oriented crystal (111) while the two other grains show oriented planes (213) and (215). Three particular areas have been magnified to observe the presence or not of LIPSS, in the grains or in the vicinity of a grain boundary. This result indicates a strong dependence in orientation, the (111) orientation appearing less favorable than the others for the formation of LIPSS at its surface. Figure 1.8 (c) shows results reinforcing this observation on another impact with crystal orientations of orthogonal directions to (111), i.e. (100) and (110). This impact was analyzed by EBSD (Figure 1.8 (d)), revealing a more marked disorientation for (111) than for the other planes. This means that the defects formed are more important for this orientation than for the others. In other words, there seems to be a competition between the absorbed laser energy converted into crystal defects or into periodic surface structuring, potentially possible when a solid-liquid phase transition occurs. The conclusions of this work are speculative for the moment but we can imagine that the (111) plane, which is the most difficult to melt since it is denser (its melting temperature is close to that of the bulk), remains solid, thus accommodating and trapping its defects after each laser pulse. Conversely, when the two planes (100) and (110) exceed the surface melting threshold, assumed to be several hundred Kelvin lower for the first atomic layers [47], a flow of material is possible and the structuring is organized. The higher defect density observed for the (111) crystal plane has recently been attributed in part to the formation of twins. This formation can occur either under the effect of very high pressures or during resolidification. The preferred direction of the pressure gradients does not allow the twinning of (111) planes, diminishing the validity of the first hypothesis. The second hypothesis, linked to a resolidification, is also questionable, knowing that these defects are also created in great proportion at low fluences, not implying, a priori, any phase transformation [41].

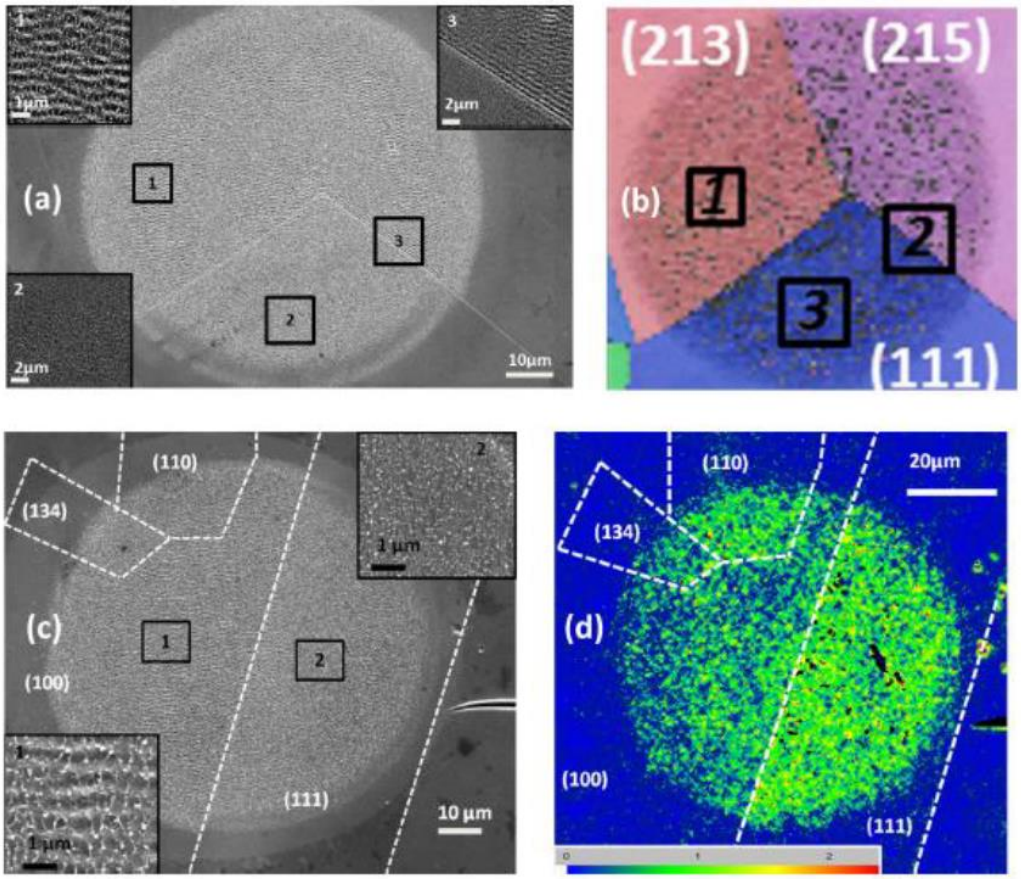

Figure 1.8: (a) SEM image of a site irradiated with 20 laser pulses at 0.3 J/cm². b) EBSD mapping where the color depends on the crystalline orientation with respect to the normal to the surface. The indices corresponding to the crystalline plane parallel to the surface are indicated. Each numbered region is visible in the insets of the figure on the left. (c) SEM image of a site irradiated with 18 laser pulses at 0.38 J/cm². (d) Local disorientation mapping by EBSD indicating greater distortion of the crystal planes (111). (c, d) Clearly illustrate the competition between the formation of LIPSS and the accumulation of defects. Adapted from [41].

Moreover, other work on Cr has revealed that material response to the first laser pulse is strongly dependent on crystallographic surface orientation, with (100) Cr surface exhibiting the formation of higher and more refined nanoscale surface roughness as compared to (110) surface [18]. The higher surface roughness generated by the first laser pulse activates scattering of the laser light and the local field enhancement upon irradiation by the second laser pulse, leading to the formation of much more pronounced high spatial frequency structures on the (100) surface as compared to (110) one.

1.3 LIPSS formation approaches

1.3.1 Brief history

Close to the modification energy threshold of most materials, it is possible to generate a periodic alignment of surface ripples, often referred to as "LIPSS" or "ripples". These laser-induced structures have been observed since the mid-1960s, but have been the subject of increasing interest since the advent of ultrashort lasers. These lasers allow us to reach periodicities well below the laser wavelength, ranging from a few tens of nanometers to a few microns, and this on all types of materials, even those with a band-gap higher than the laser wavelength [48]. These structures can reach a few hundred nanometers in amplitude and offer tribological, optical, or wettability perspectives of interest to the fundamental and applied scientific community [31]. The current issues are mainly related to the control of the amplitude and periodicity of the structures, depending on the laser parameters and the irradiated material.

LSFL $\Lambda > \lambda/2$		HSFL $\Lambda < \lambda/2$		2D-LIPSS $\lambda/10m < \Lambda < \lambda$	
LSFL-I	LSFL-II	HSFL-I	HSFL-II	2DL-I	2DL-II
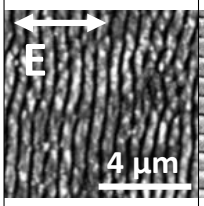	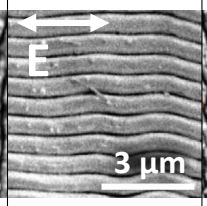	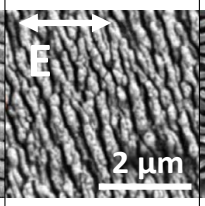	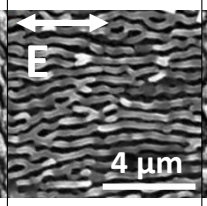	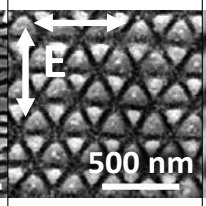	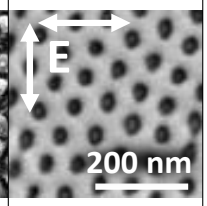
$\Lambda \simeq \lambda$ $\perp$ to Pol.	$\Lambda \simeq \lambda/n$ $\parallel$ to Pol.	Deep HSFL A > 1	Shallow HSFL A < 1	$\Lambda \simeq \lambda/m$	$\Lambda \simeq \lambda/10m$ 1 < A < 4

Table 1.2: General classification of laser-induced periodic surface structures LSFL, high spatial frequency HSFL and two-dimensional periodic structures 2D-LIPSS. m presents an integer number to show that the size of 2DL-II are approximately 10 times smaller than 2DL-I. Adapted from [49].

Furthermore, LIPSS are divided into two groups in table 1.2, based on their spatial period in relation to the utilized laser wavelength λ: Low-spatial frequency LIPSS (LSFL) with $\Lambda > \lambda/2$ and high-spatial frequency LIPSS (HSFL) with $\Lambda < \lambda/2$. During laser matter interaction, the electronic structure of the material determines the period of the structures and their orientation with respect to the beam polarization direction, which are used to further categorize and sub-classify the LSFL. These structures are mainly observed by a period $\Lambda \simeq \lambda$ and their orientation are perpendicular to the beam polarization for strong absorbing materials, such as metals and semiconductors, and they are named LSFL-I. However, LIPSS are generated with $\Lambda \simeq \lambda/n$ parallel to the beam polarization on some large bandgap materials, such as fused silica. The refractive index of the corresponding dielectric material is represented by n. On the other side, analogous variety of LIPSS were observed with a periodicity and size far below than the optical diffraction limit, known as high-spatial frequency LIPSS or HSFL. They are classified into two categories based on the depth-to-period

aspect ratio A: HSFL-I, with A > 1, and HSFL-II, with A < 1 [49].

Material	LSFL		HSFL		2D-LIPSS		References.
	Λ (nm)	Ori.	Λ (nm)	Ori.	Λ (nm)	Ori.	
Ag	625	⊥					Vorobyevet al. 2008[9]
Al	500-530	⊥					Golosov et al. 2011[50]
Al			20-220	n.s.			Bashir et al. 2012[51]
Au	580	⊥					Vorobyev et al. 2007[52]
Br	800	⊥					Huang et al. 2009[53]
C					80-100	2DL-II, Nanobumps	Matteo et al. 2021[54]
Cu	500-700	⊥	270	⊥			Sakabe et al.2009[55]
Co					500-700	2DL-I, Sphere	Jalil et al. 2019[19]
Co					380-700	2DL-I, Triangle	Jalil et al. 2019[19]
Co					680-780	2DL-I, Rhombus	Jalil et al. 2019[19]
Cr	460-550	⊥					Albu et al. 2013[56]
Mg	480-520	⊥					Guan et al. 2014[57]
Mo	580-720	⊥					Okamuro et al. 2010[58]
Nb	450-700	⊥	290-350	∥			Pan et al. 2014[59]
Ni	750-760	⊥					Garrelie et al. 2011[28]
Ni			70-90	∥			Sedao et al. 2016[60]
Ni					20-60	2DL-II, Nanocavities	Abou Saleh et al. 2020[21]
Ni					80-110	2DL-II, Nanobumps	Nakhoul et al. 2021[22]
Ni					20-100	2DL-II, Nanopeaks	Nakhoul et al. 2022[34]
Pt	580-780	⊥					Okamuro et al. 2010[58]
St(316L)					300-600	2DL-I, Triangle	Fraggelakis et al. 2019[61]
St(316L)	660	⊥					Dusser et al. 2010[31]
St(100Cr6)	420-780	⊥					Tsidibis et al. 2018[62]
St(100Cr6)			100-220	∥			Bonse et al. 2018[49]
Ti	405-700	⊥	65-90	∥			Bonse et al. 2013[63]
V	540-700	⊥					Fule et al. 2015[64]
W	580-780	⊥					Okamuro et al. 2010[58]
Zn	500	n.s					Chen et al. 2014[65]
Zr	390-820						Ali et al. 2017[66]

Table 1.3: Literature survey of LIPSS reported on common metals upon fs-laser pulse irradiation under nearly normal incidence in air or vacuum. LIPSS orientation: ⊥, ripples aligned perpendicular to polarization; ∥, ripples aligned parallel to polarization; n.s, not specified. Adapted from [4].

Recent investigations show that two orthogonal linear polarization states can cancel polarization dependence of nanopatterns alignment. Controlling ultrafast laser pulse polarization, inter-pulse delay, and laser fluence creates unique 2D surface morphologies. Several studies focused on near-submicron 2D-LIPSS have revealed the appearance of rhombus,

triangle and spherical structures on cobalt[19], while others have reported triangular and square nanostructures by using double linearly crossed polarized and counter-rotating circularly polarized pulses on stainless steel with a time-delays in the picosecond range [20]. These periodic nanostructures were created by scanning the surface and have a periodicity close to the laser wavelength and named in this thesis as 2DL-I. However, none of these studies have reported such symmetry features at the nanoscale. Driven by near-field light enhancement, periodic patterns have reached ultimate sizes of tens of nanometers on a (001)-oriented Nickel surface. A self-organizing array of nanocavities with a diameter of 20 nm and a periodicity of 60 nm was developed by delaying cross-polarized laser pulses, this technique overcomes the anisotropic polarization response of the surface, allowing for self-arranged nanoscale topography in advanced technological areas [21, 22]. These nanostructures are named in table 1.2 as 2DL-II.

Furthermore, table 1.3 provides a literature survey of LIPSS reported on common metals upon femtosecond laser pulse irradiation. This table display the recently revealed 2D-LIPSS type I and II which will be discussed in section 1.4.

1.3.2 Electromagnetic approach

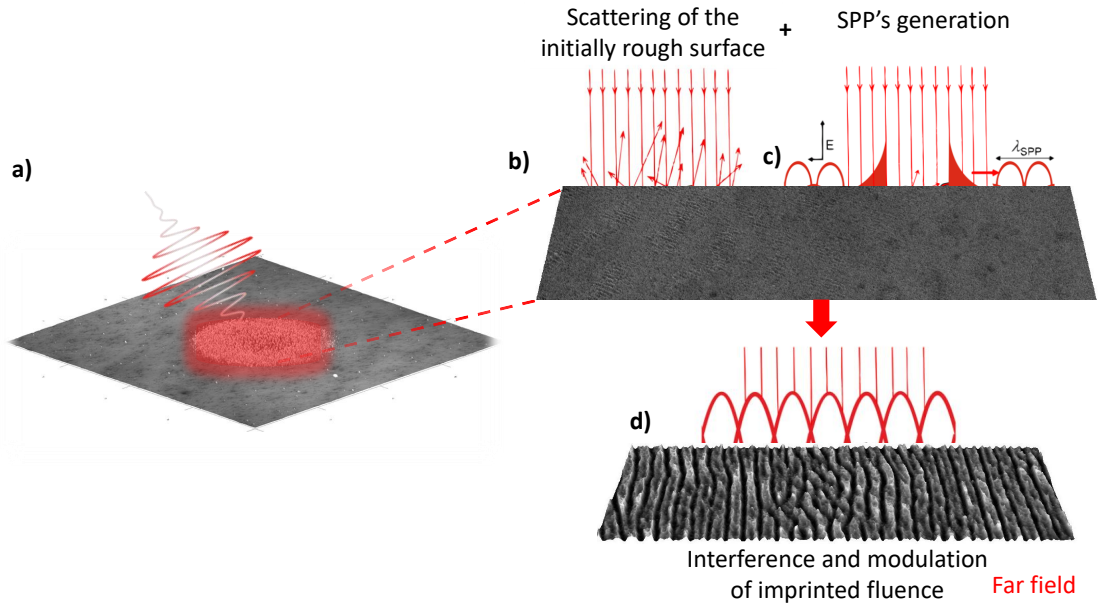

Figure 1.9: Scheme of electromagnetic formation mechanisms of LIPSS. a) Scheme of the interaction of the incident laser beam with a rough surface. b) Optical scattering that may lead to the excitation of b) SPPs that interfere with the incident light and modulate the absorbed fluence pattern "imprinted" in the material. c) Finally, modulated ablation results in periodic surface structures. Adapted from [67]

.

During the 1980s of the previous century, detailed electromagnetic theories on the creation of LIPSS, based on the interference of electromagnetic radiation scattered at the microscopic rough surface, were developed [68–70]. The fundamental concept underlying

these ideas is depicted in Figure 1.9. During laser irradiation, incident light scatters at the roughness of the sample surface (Figure 1.9 (a)) via elementary Huygens waves generated coherently. Other surface excitation modes, such as surface plasmon polaritons SPPs, presented in Figure 1.9 (c), may be additionally stimulated at specific conditions. The interference of the incident radiation with that emerging from scattering and SPPs leads to a spatial modulation of the local energy distribution that—via absorption—is imprinted to the sample material (Figure 1.9 (d)). For strong laser excitation, the creation of the eventual periodic surface relief is subsequently triggered, for instance, by spatially modulated material removal (ablation). In addition to the interference between the incident laser radiation and the electromagnetic field of the plasmons creating the primary LIPSS grating, the interference of (counter) propagating SPPs may result in additional second-order contributions [67, 71].

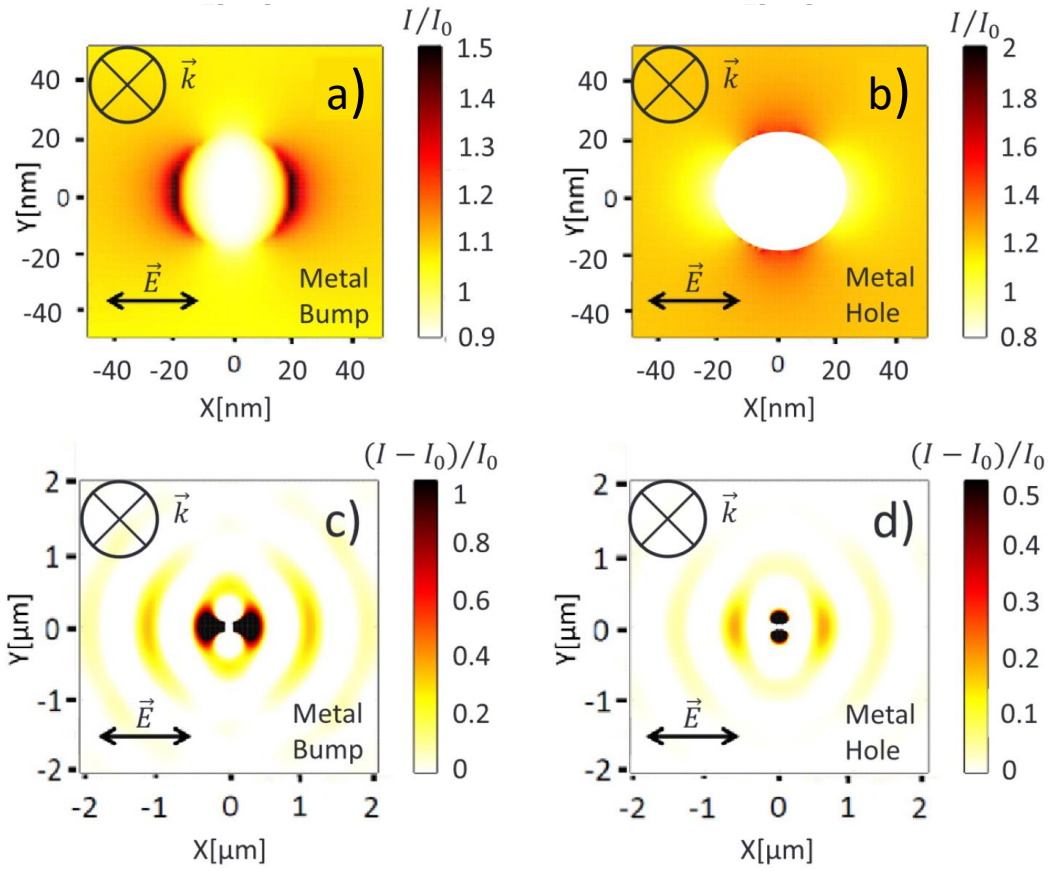

Figure 1.10: (a-b) Energy deposition below metal surface in the transverse plane (a) with a bump R = 20nm, (b) with a hole R = 20 nm. (c-d) Absorbed energy in the transverse plane on metal surface with (c) a bump, (d) a hole of R = 20 nm. Light interaction exhibit contrasting polarization-sensitive interference patterns (in the micrometer scale) depending on the optical material properties and the nature of imperfections. Adapted from [15].

On the other hand, Rudenko et al. have calculated and analyzed the intensity near-field reactive and radiative patterns resulted from the interference of the incident light with light scattered by individual subwavelength holes and bumps on the surface of metallic materials [15]. Figure 1.10 presents the energy deposition and the relative absorbed intensity

in the transverse plane of metal surface with bump and hole. Figure 1.10 (a) illustrates the intensity distribution beneath a metallic surface. The energy here is not deposited on the top of the metallic bump, but only on the surface dominantly in the direction parallel to laser polarization. This study indicates that laser ablation does not necessarily remove the bump, but rather creates a more pronounced imperfection. Furthermore, the energy is still mostly deposited inside the nanometric hole, and similar dependencies of local field maxima perpendicular to laser polarization are revealed in Figure 1.10 (b) for stainless steel. As a result, material ablation promotes the formation of deep ellipsoidal holes that are elongated perpendicular to the laser polarization.

Moreover, Figure 1.10 (c-d) shows the main features of both radiative and non-radiative fields scattered by subwavelength imperfections on the surface. The interference patterns are more pronounced in parallel direction on metal surface. In contrast to local near-field, the orientation of the radiative patterns does not depend on the nature of the imperfections. The distances between the intensity maxima positions and the emission centers, on the other hand, reveal a striking difference. This is due to the various phase retardation of surface waves scattered by holes and bumps. As a result, the first far-field maxima (as opposed to the local near-field) are further away from the bump than from the hole for metal surfaces. It should be noted that the difference is directly related to charge accumulation at the interface of imperfection and, thus, to local near-field distributions. For metals, the symmetry is broken due to additional contribution of surface plasmon wave in the direction parallel to the electric field with spacing $\approx \lambda$ in Figure 1.10 (c-d).

1.3.3 Coupling electromagnetic to hydrodynamic approach

Recently, a model combining three-dimensional electromagnetic and hydrodynamic approaches was developed. This model enables self-consistent investigation of the multipulse evolution of surface relief by recalculating the energy distribution on the corrugated surface at the beginning of each pulse and taking into account both liquid melt flow and ablation processes. Here, compressible Navier-Stokes equations have been solved supplemented by the equation of state and consider the deformable free surface. This allows the consideration of pressure wave propagation induced by a temperature gradient as well as ablative recoil pressure acting on a liquid layer. Furthermore, Maxwell equations computed inhomogeneous absorption on surface roughness enable a wide range of initial perturbations and anisotropic temperature gradients for the generation of hydrothermal waves and forced liquid melt flows.

The surface dynamics was studied after laser irradiation with Gaussian femtosecond pulses up and down the Z axis and laser polarization along the X axis, as shown in Figure 1.11. Furthermore, the laser wavelength is 800 nm, and the pulse duration is set in numerical calculations to be 80 fs. They were interested in surface topography modifications at the nanoscale caused by liquid melt flow and material removal. The density snapshots in these simulations are obtained 100 ps after irradiation. During this time, it is assumed that the ablated material has been removed and the fluid movement has been finalized. Further computations have no effect on material redistribution and reveal quick cooling and resolidification tendencies. For example, in Figure 1.11, material redistribution above the original

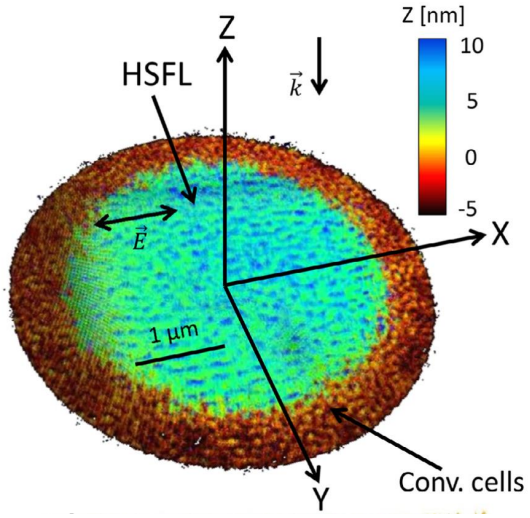

Figure 1.11: Numerical simulations show the surface topography upon single pulse irradiation of nickel, where the structures of interest are indicated: HSFL (high-spatial frequency LIPSS) and convection cells in form of nanoholes. The colors correspond to the surface depth Z. Adapted from [72].

surface results in the creation of periodic surface structures with periods (lambda) 150 nm parallel to the laser polarization in the center of the laser-irradiated zone. This conclusion is consistent with prior research [21, 60]. Convection cells in the form of nanoholes form on the borders of the laser-heated zone. The lowest energy dose corresponds to hexagonal nanoholes with spacings of 80 nm and diameters of 20 nm. HSFL oriented parallel to laser polarization with periods of 150 nm are observed closer to the center of the laser-irradiated zone. Finally, LSFL with periods of 600 nm oriented perpendicular to laser polarization occupy the center of the laser-irradiated zone. Furthermore, a parallel HSFL sequence can be observed between neighbor LSFL crests, forming a mixed structure of crossed LIPSS.

Moreover, 3D simulations of the energy deposition and material modification on the Ni surface were performed in chapter 5. The absorbed energy density was calculated based on the solution of Maxwell equations (for electric and magnetic fields $\vec{E}$ and $\vec{H}$) by using the finite-difference time-domain (FDTD) method with the auxiliary equation for polarization current $\vec{J}$ (Drude model for Ni metal with ω_{pl} and ν plasma and collision frequencies) [73] as follows:

$$\begin{cases} \dfrac{\partial \vec{E}}{\partial t} = \dfrac{\nabla \times \vec{H}}{\epsilon_0} - \dfrac{1}{\epsilon_0}\vec{J} \\ \dfrac{\partial \vec{H}}{\partial t} = -\dfrac{\nabla \times \vec{E}}{\mu_0} \\ \dfrac{\partial \vec{J}}{\partial t} + \vec{J}\nu = \epsilon_0 \omega_{pl}^2 \vec{E}. \end{cases} \tag{1.3}$$

The absorbed energy was defined as $I\alpha_{abs}$, where $I = \frac{1}{2}\sqrt{\frac{\epsilon_0}{\mu_0}}\left|\vec{E}\right|^2$ is the intensity and α_{abs} is the absorption coefficient related to the extinction coefficient k as $\alpha_{abs} = 4\pi k/\lambda$. Then, a two-temperature model (TTM) was implemented to resolve electron-ion heat transfer and

diffusion [74] and compressible Navier-Stokes equations [72, 75] were applied as follows

$$\begin{cases} C_e \dfrac{\partial T_e}{\partial t} = \nabla \cdot (k_e \nabla T_e) - \gamma_{ei}(T_e - T_i) + I\alpha_{abs} \\ \rho C_i \left[\dfrac{\partial T_i}{\partial t} + \vec{u} \cdot \nabla T_i \right] = \nabla \left(k_i \nabla T_i \right) + \gamma_{ei}(T_e - T_i) \\ \dfrac{\partial (\rho \vec{u})}{\partial t} + (\vec{u} \cdot \nabla)(\rho \vec{u}) + (\rho \vec{u}) \nabla \cdot \vec{u} = \\ = -\nabla (P_e + P_i) + \mu \nabla^2 \vec{u} + \dfrac{1}{3} \mu \nabla (\nabla \cdot \vec{u}) \\ \dfrac{\partial \rho}{\partial t} + \nabla \cdot (\rho \vec{u}) = 0, \end{cases} \tag{1.4}$$

Based on this work and prior theoretical research, Table 1.4 summarizes the types of periodic structures typically observed on metal surfaces, their precursors, the origins of their periodicity and orientation, and feasible feedback mechanisms for their creation.

Types of LIPSS	Precursors	Origin of orientation	Origin of periodicity	Feedback
HSFL-∥	Laser-induced cavities or LSFL hollows	Hydrothermal waves induced by non-radiative fields	Marangoni convection instability	Melt flow
HSFL-⊥	Pristine bumps or laser-induced protrusions	Hydrothermal waves induced by non-radiative fields	Marangoni convection instability	Melt flow + Possible ablation
LSFL-⊥	Holes, bumps, nanoparticles	Radiative plasmonic or(+) non-plasmonic fields	Interference	Ablation
Grooves-∥ (electromagnetic)	Irregular LSFL hollows / bumps	Radiative fields Hydrothermal waves induced by LSFL non-radiative fields	Interference Maranoni convection instability	Melt flow
Grooves-∥ (hydrodynamic)	LSFL hollows	Radiative fields Hydrothermal waves induced by LSFL non-radiative fields	Interference Maranoni convection instability	Melt flow
Hexagonal nanostructures	Hot spots in thin melt layer destabilized by rarefaction	-	Marangoni convection instability	Melt flow + Cavitation
Hexagonal microstructures (spike)	Hot spots in thick melt layer destabilized by recoil pressure	-	Marangoni convection instability	Melt flow + Ablation
High aspect-ratio nanopeaks	Hot spots in thick melt layer destabilized by recoil pressure	-	Marangoni convection instability	Melt flow + ridges

Table 1.4: Types of periodic surface structures on metals and their formation mechanisms. Adapted from [72].

It was noticed that surface inhomogeneity is the precursor to all organized structures. On laser-excited surfaces, energy is anisotropically distributed due to light interference with scattered fields from surface topography. The absorbed energy distribution is a consequence of non-radiative (short-distance and confined to nanoscale features) and radiative (long-distance and laser wavelength related) optical responses of rough surface [12, 15]. Two major multipulse feedback scenarios are then possible to drive the matter into

self-organized nanostructures. The electromagnetic scenario is based on the selection of a unique wavelength-related frequency for surface topography, where light follows the topography and the topography is morphed by light pulse-by-pulse by material removal at the regions with the most absorbed energy [11, 76]. This is possible due to coherent nature of the radiative optical response, but also due to positive feedback, resulting in the amplification of patterns with particular periodicity. The (radiative or non-radiative) optical response, on the other hand, can be considered as the polarization-dependent perturbation required for the development of hydrodynamic instability. In this case, the frequency of the resultant patterns is determined by material properties, and, therefore, the amplification and the multipulse feedback is possible following the hydrodynamic scenario.

1.3.4 Surface oxidation enhancing LIPSS formation

Even more complex situations than surfaces of distinct types of bulk materials can be examined using FDTD. Florian et al. recently demonstrated this [77], as they studied the effect of a laser-induced oxide layer generated at the surface of oxidation-prone, strongly absorbent materials such as a CrN ceramic, as presented in Figure 1.12. It has been observed that the oxide layer is a significant parameter that substantially influences the formation of a regular intensity pattern at the interface to the underlying material, which probably leads to the formation of LSFL structures parallel to the laser polarization. Moreover, the thickness of the oxide layer should be in the order of 100 nm to allow the production of a regular intensity pattern that can be imprinted at the interface between the superficial oxide layer and the underlying material (CrN), as suggested in [78].

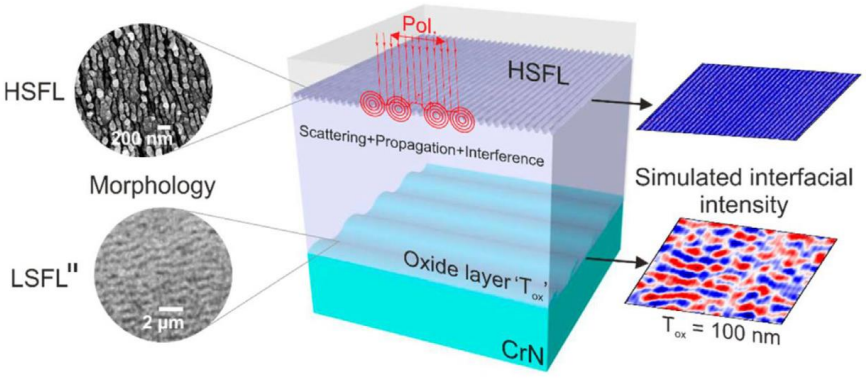

Figure 1.12: Scheme of the formation of interfacial LSFL parallel to the linear beam polarization in an oxidation prone material. [77].

Furthermore, they found that the presence of superficial sub-wavelength HSFL on the oxide layer is fundamental to the formation of near-wavelength LSFL parallel. Finally, the intensity pattern with spatial $LSFL_{\parallel}$ characteristics is formed by the combined action of electromagnetic scattering, propagation, and interference effects and does not require the

presence of a partially metallic oxide layer via laser-excited conduction band electrons or nano-plasmas scattering from localized defects [13], as illustrated in Figure 1.12. According to the research, these effects can be observed on strong absorbing materials that are prone to oxide development.

1.3.5 Theory of self-organisation

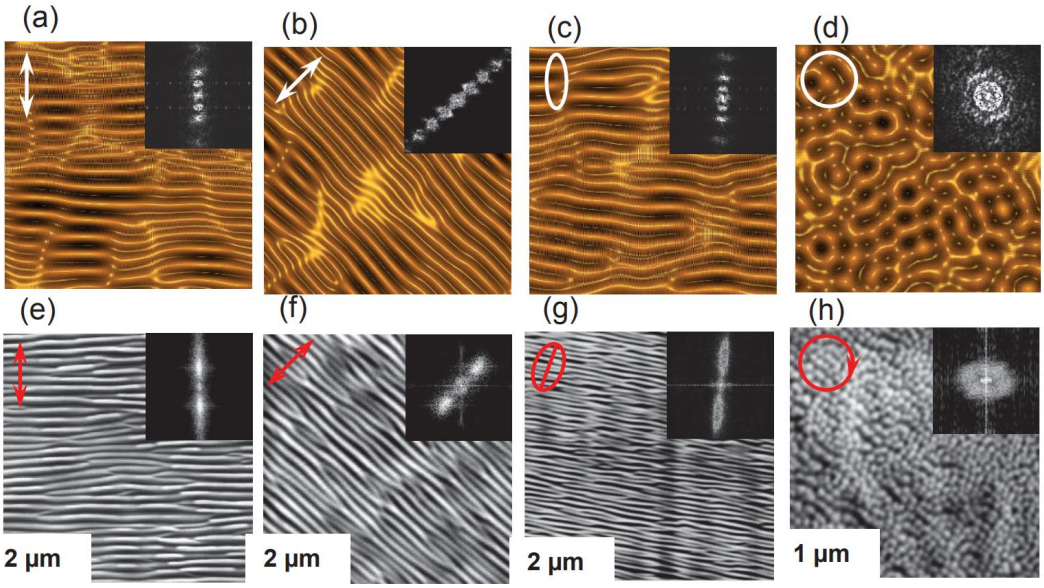

Figure 1.13: The upper row (a-d) presents numerically calculated surfaces showing the surface morphologies with various parameters. The lower row (e-h) exhibits SEM micrographs of a CaF_2 surface irradiated by 5000 pulses at intensity $8x10^{12}$ W/cm² with linear (e-f), elliptical (g) and circular (h) polarization; here the direction of incident electrical laser field is indicated with double arrows, ellipse and circle, correspondingly. The corresponding 2D-FFT images are presented in the inserts. Adapted from [79].

The self-organization process was first proposed in the 1990s to theoretically explain a specific class of periodic laser-induced structures that differed qualitatively from LIPSS in that their orientation was unrelated to the laser polarization and the structure period was not directly correlated to the exciting radiation wavelength. Later, Reif et al. employed self-organization to explain the creation of LIPSS on wide bandgap materials using a nonlinear-dynamic erosion/smoothing model, similar to that used in ion sputtering, to simulate surface pattering during multi-pulse femtosecond laser ablation [79–81]. The model is used to account for how laser polarization affects nanostructure features, as presented in Equation 1.5. Based on a Kuramoto-Snivashinsky nonlinear equation, it is demonstrated that directional anisotropy in pattern generation may result from spatial anisotropy of the initial excitation/energy-coupling process, such as resonant coupling to surface plasmons/polaritons or electron diffusion features.

$$\frac{\partial h}{\partial t} = -\nu(h)\sqrt{1+(\nabla h)^2} - D\Delta^2 h \tag{1.5}$$

It was demonstrated that the correlation of ripple topography and orientation with laser polarization can be characterized within a model in which the polarization creates an asymmetry in the deposited energy distribution and causes symmetry breaking on the surface. The numerically predicted patterns formed by this model and the experimental results acquired by femtosecond laser ablation of diverse materials with linear, circular, and elliptical polarized pulses were found to be in good agreement. The model accurately describes the basic properties of surface structures.

1.4 Formation of 2D-LIPSS

1.4.1 2D LIPSS-I, on the hundreds of nanometers scale

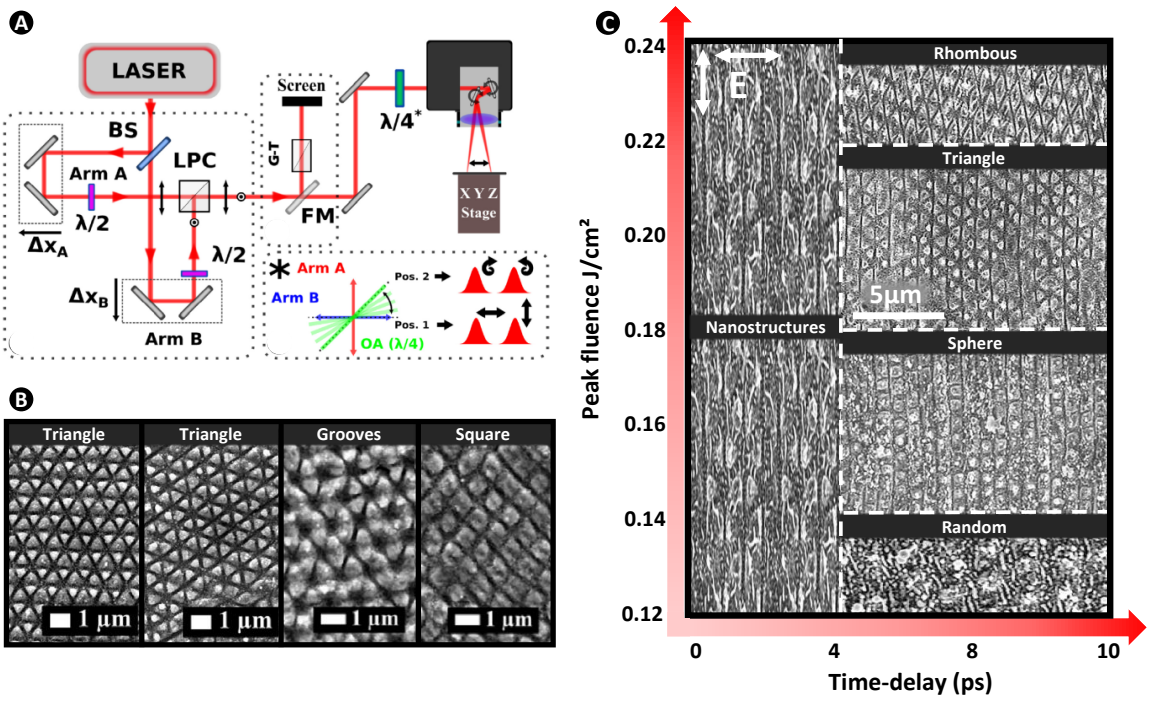

Figure 1.14: A: Experimental setup for 2DL-I, using Mach-Zehnder interferometer coupled with Galvo scanner. B: SEM images of stainless steel surface irradiated with two different polarization configuration and time delays. Adapted from [20]. C: Morphological map of 2DL-I surface with different laser fluences and time delays, under irradiation of two temporally delayed femtosecond laser beams on Cobalt. Adapted from [19].

Since 2019, Fraggelakis et al. have reported a unique type of nanostructures on the hundreds of nanometers scale called 2D-LIPSS [20]. These nanostructures are created using a Mach-Zehnder interferometer combined with two circular or cross polarizations and

coupled with a galvo scanner as presented in Figure 1.14 (A). They have a periodicity on the scale of hundreds of nanometers and are named in this 2DL-I. As observed in Figure 1.14 (B), time-delay and laser polarization both play a crucial role in creating these type of nanostructures on stainless steel. Triangle structures were observed using two circular polarization at J/cm² and ps and using cross polarization at J/cm² and ps. However, grooves and square nanostrucres were revealed at time delays of few nanoseconds. Moreover, other researchers were also working on discovering different types of 2DL-I on other materials owing to the good industrial potential of these structures. In the same year, Jalil et al. revealed the appearance of rhombus, triangle, and spherical structures on cobalt using a similar experimental procedure presented in Figure 1.14 (A). As observed in Figure 1.14 (C), the time-delay and laser fluence both play a significant role in controlling the 2D surface morphology [19].

1.4.2 2D LIPSS-II, on the tens of nanometers scale

Recently, another types of 2D-LIPSS has been revealed on Diamond surface by Matteo et al. in 2021 [54], by using a Michelson-like interferometer to generate two time-delayed cross polarized double pulses as presented in Figure 1.15.

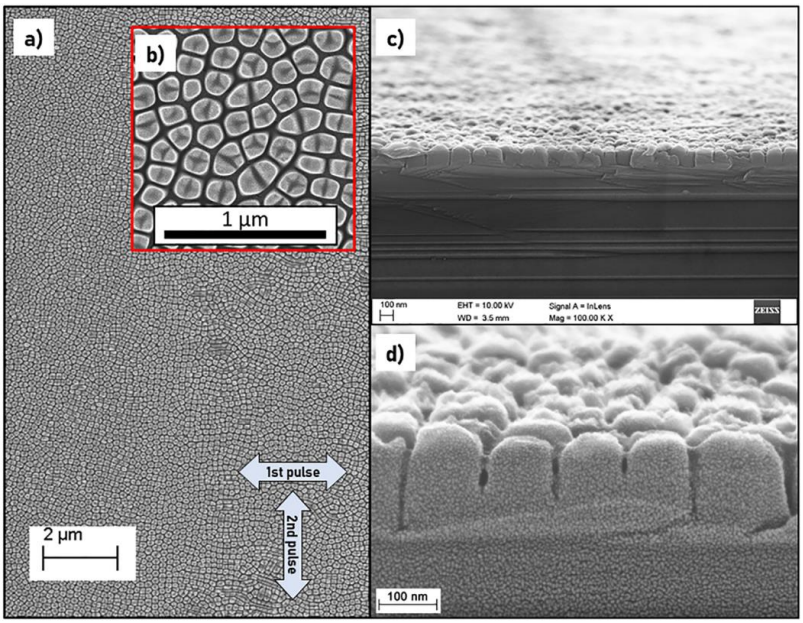

Figure 1.15: Top view (a, b) of the nanotextures obtained at Φ_{ASB} = 216 J/cm², $\Delta\tau$ = 500 fs, scanning speed of 0.75 mm/s. Cross-section view at different magnifications (c,d). The arrows indicate the polarization directions. Adapted from [54].

It was observed the formation of 80 nm 2D-LIPSS on single-crystal and polycrytalline diamond surfaces. The periodicity of these nanostructures can be controlled in the range $\lambda/4 \geq \Lambda \geq \lambda/10$. These 2D laser-induced periodic surface structure exhibited remarkable anti-reflection properties after removing surface debris by chemical etching, which increased the scattering rate of visible light by 50 times.

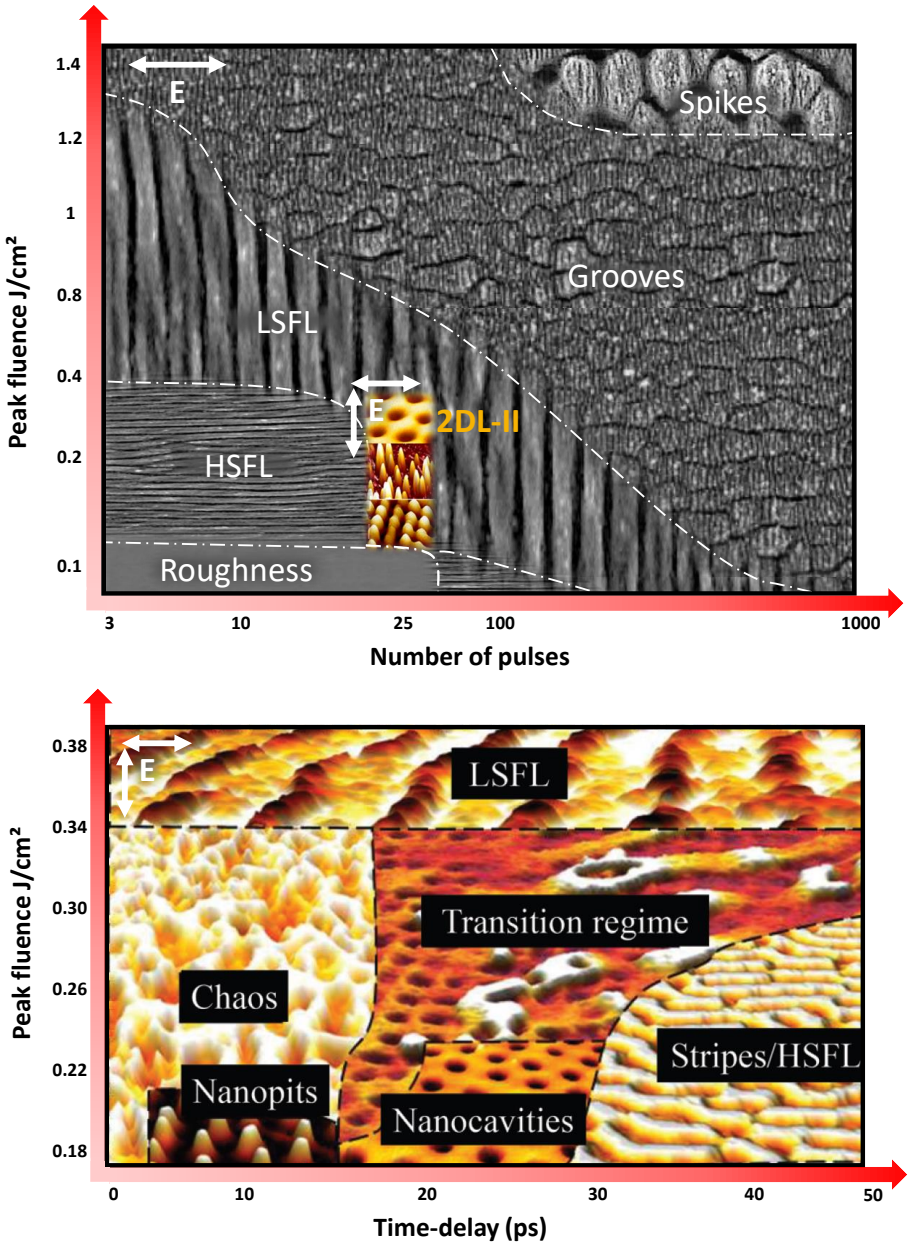

Figure 1.16: A: Morphological map of characteristic surface morphologies (HSFL, LSFL, grooves, and spikes) formed on 100Cr6 steel surfaces upon line-wise fs-laser area scanning at different irradiation parameters. Adapted from [82]. B: LIPSS formation as a function of the peak fluence and time-delay imposed between the pulses of a double pulse sequence with Number of Double-Pulse Sequences (N_{DPS}) = 25. The different regimes of nanostructure formation in terms of symmetry, dimensions and periodicities are limited by the dashed lines. The favorable window for regular 2D-nanostructuring is relatively narrow. Adapted from [21].

On the other side, Abou Saleh et al. have revealed in 2020 a smaller types of nanostructures on (001)-oriented Nickel surface by using Mach-Zehnder interferometer double pulses with a time delay of few ps (explained in Chapter 2). These nanopatters were pro-

duced by breaking the surface isotropy through crossed polarization, but their scale is tens times smaller than the conventional observed 2DL-I; therefore, we refer to them as 2DL-II [83].

Figure 1.16 (A) presents surface morphologies formed on 100Cr6 steel surface by using singular polarization, with different peak fluences and number of pulses. The aim of this graph is to position the 2DL-II with respect to the conventionally observed HSFL, LSFL, grooves and spikes. The 2DL-II are observed with several time-delays and laser fluence on Ni(001), as presented in Figure 1.16. The main 2D nanostructures consist of hexagonally organized nanoholes with a diameter of 20 nm separated by a distance of approximately 60 nm. The results indicate that the formation of nanohole array structures requires a time-delay window of $\approx$ 20 ps between the delayed pulses, which is influenced slightly by the incident fluence. Nanoholes are also shown to be polarization dependent. This regime has opened the door for the exploration of several self-oragnized nanostrucures, which will be presented and discussed in this manuscript [22, 34].

1.5 Conclusion

In this chapter, we have reviewed the principle mechanisms of femtosecond-metal laser interaction, since metals were in our scope of focus in this thesis. Different types of LIPSS were presented based on their size and periodicity. Also, we briefly discussed the influence of crystalline orientation on LIPSS and defects generation. Finally, we shed the light on the 2D nanostructures, which were classified and categorized into two types based on their nanoscale size. In the next chapter, we will begin with a description of the experimental setup used in this study as well as a presentation of the different instruments employed to analyze our results.

Part II

Beyond the State of the Art

Chapter 2

Experimental methods

When you find in yourself how to turn your weakness into a virtue, success stops being an option and becomes a certainty

– Maria Georges Zakhem

2.1 Introduction

The aim of this chapter is to describe the various experimental and characterisation tools that were employed for the different experiments. The first section discusses sample preparation processes, such as mechanical and electrolytic polishing, as well as the types of targets irradiated in this work. The second section describes the laser setup that has been used for surface irradiation. This entails producing femtosecond pulses of energy close to a millijoule via the laboratory's laser equipment, where double-pulse train generation using a Mach-Zehnder interferometer as well as single pulse train generation are demonstrated. The Liu method for determining laser fluence is also explained [84]. Atomic force microscopy AFM, scanning electron microscopy SEM, and transmission electron microscopy TEM are also employed to analyze LIPSS features.

2.2 Sample preparation

In order to accomplish high-quality and precise laser processing of metal surfaces, it is often impossible to utilize the sample as-is. Surface preparation to reduce the initial surface roughness must precede laser irradiation and microscopy examinations. The major purpose is to minimize the micro-roughness in order to dramatically reduce the risk of dirt or other deposits adhering to the surface. Thus, sample preparation is required prior to laser irradiation of the surface. All sample preparations were performed at the metallurgy laboratory of EMSE.

2.2.1 Samples

In this work, a mono-crystalline Nickel (Ni) sample oriented in (001) direction was mainly used in order to discover the appearance of several nanostructures and to understand their role with the main laser parameters. Single crystals are preferred to ensure the uniformity of the structuring process. The Ni (001) bar was grown by directional solidification and cut into 10x10x10 mm^3 cubes by using a wire saw. Crystal orientations were checked by X-ray diffraction prior to laser irradiation to ensure the uniform cutting direction. Moreover, a poly-crystalline titanium alloy sample (TA6V) was polished and nanostructured for antibacterial experimentation.

Different polishing processes have been applied during these experiments in order to have different surface topographies. It was essential in this stage to study the effect of initial surface roughness on femtosecond laser double pulse nanostructuring, and it was important to determine the roughness threshold (Ra_{th}) that allows the creation of uniform nanostructures. Therefore, different types of mechanical and electrochemical polishing have been tried during our experiments.

2.2.2 Mechanical polishing

Automatic polishing

Automatic polishing requires a special type of preparations. It is more complex than the manual rapid polishing, but it provides uniform and reliable results due to its controlled parameters as pressure, duration and speed. For preparation, samples should be mounted in a special resin (ProntoFix, 40200108) mixed by a hardener solution with a ratio of 2/1 at 2 Bar pressure for 20 minutes. After assuring the good quality of plastic mounting, the Automatic polishing can start on "Buehler Automet 250" as presented in Table 2.1 for Nickel and Table 2.2 for Titanium:

Nickel			
Silicon Carbide (SiC) Polishing	Duration	Speed	Pressure
P240	2 min	150 RPM	3 daN
P320	3 min	150 RPM	3 daN
P600	3 min	150 RPM	3 daN
P1200	3 min	150 RPM	3 daN
P2500	3 min	150 RPM	3 daN
Diamond Polishing	Duration	Speed	Pressure
3 µm	5 min	300 RPM	6 daN
1 µm	5 min	300 RPM	6 daN
Colloidal Silica (SiO_2) Polishing	Duration	Speed	Pressure
0.05 µm	10 min	150 RPM	6 daN
Water Rinsing	Duration	Speed	Pressure
H_2O	10 min	300 RPM	6 daN

Table 2.1: Automatic polishing procedure for Nickel. RPM refers to Revolutions Per Minute and daN refers to DecaNewton.

It is very essential to apply an ultrasonic bath for few minutes between each step, in order to clean the surface and have a better quality of polishing.

Vibrometer Polishing with Colloidal Silica:

Additional procedure is also required by applying the Colloidal Silica (SiO_2) polishing with the Vibrometer "Buehler Vibromet 2" for few hours. These conditions can guarantee a very low surface roughness and a sample ready for characterization by EBSD, if needed.

However, the above processes should be definitely followed by a special cleaning method in order to remove the SiO_2 stuck on the surface, which can deviate the experiments accuracy.

Colloidal Silica cleaning method:

Titanium			
Silicon Carbide (SiC) Polishing	Duration	Speed	Pressure
P240	2 min	150 RPM	3 daN
P320	3 min	150 RPM	3 daN
P600	3 min	150 RPM	3 daN
P1200	3 min	150 RPM	3 daN
P4000	3 min	150 RPM	3 daN
Diamond Polishing	Duration	Speed	Pressure
6 µm	5 min	300 RPM	6 daN
3 µm	5 min	300 RPM	6 daN
1 µm	5 min	300 RPM	6 daN
Colloidal Silica (SiO_2) Polishing	Duration	Speed	Pressure
0.05 µm + 3% H_2O_2 + 3% NH_4OH	10 min	150 RPM	6 daN
Water Rinsing	Duration	Speed	Pressure
H_2O	10 min	300 RPM	6 daN

Table 2.2: Automatic polishing procedure for Titanium alloy. RPM refers to Revolutions Per Minute and daN refers to DecaNewton.

It is essential to apply this method immediately after completing the polishing on the Vibromet machine. This method consists of a manual cleaning cycle as per the below:

1. Ultrasonic bath with alcohol.
2. Ultrasonic bath with hot water.
3. Manual polishing with a new non-abrasive disc lubricated with hot water and liquid soap.
4. Ultrasonic bath with alcohol
5. Ultrasonic bath with hot water

Note: This cycle should be applied 4-5 times in order to remove all the stuck SiO_2 from the surface.

Manual polishing

Manual polishing process has also been applied in order to create samples with different arithmetic roughness. We used papers with different abrasive particles of silicon carbide (SiC). The procedure starts with a coarse paper than moves gradually to the finest P600, P800, P1000, P2500. For a given paper, polishing direction should be kept constant. However, we cross the direction from a paper to another. Procedure will be completed by an ultrasonic bath for few minutes.

2.2.3 Electrolytic polishing

Electropolishing is a chemical technique of surface treatment by electrolytic action consisting in removing ion by ion the metal from the surface of a metal object. It is also used for deburring, brightening and passivation. This method does not cause distortion since electropolished samples are not subjected to mechanical or thermal stress, as abrasives would produce. Thus, the primary objective is to minimize the microroughness as much as possible and to obtain a smoother surface without any surface hardening zone.

Electropolishing process consists of removing metal from a component immersed in an electrolyte of a certain composition while an electric current flows through it. The anode is connected to the sample, while the cathode is connected to an appropriate conductor. Two poles are immersed in an electrolyte to complete the electrical circuit. As it is submerged in the electrolytic bath, the metal component acquires a positive charge (anode). Applied current turns the conductive electrolyte into a "tool" that removes metal ions from the part. The ions are attracted to the cathode, while the majority of the dissolved metals stay in solution. Some ions settle as mud on the cathodes, necessitating regular cleaning to keep the system running smoothly. The release of oxygen on the metal's surface improves the electrolytic action even more. The equipment is a microprocessor-controlled LectroPol-5 polishing machine, delivered by Struers company.

After selecting the electrolyte, the polishing voltage must be determined. To accomplish this, we shall utilize the scanning feature integrated in the machine. Once the sample is positioned on the polishing table, the current density curve is determined by scanning a specified voltage range. This curve is used to estimate the polishing voltage for the polishing or thinning process. Other parameters that must be specified are polishing time and flow rate. Once the polishing parameters have been established, they can be saved to the database and applied to subsequent polishing processes. Several electrolytes can be utilized to polish a variety of materials. The best option depends on the material's composition and the intended analysis. Table 2.3 presents the electrolytic parameters used for polishing Ni and Ti samples.

Electrolytic parameters			
Sample	Duration (s)	Voltage (V)	Electrolyte
Ni	60	25	Ethanol 95% + perchloric acid 5%.
Ti	10	25	Methanol 60% + ethylene glycol monobutyl ether 34% + perchloric acid 6%.

Table 2.3: Electrolytic parameters used for polishing Ni and Ti samples

2.2.4 Comparison between different polishing procedures

After presenting the different types of polishing, we present in this section a comparison between four different polishing procedures for the Nickel material. Procedure 1 consists of an automatic polishing with SiC, followed by diamond and colloidal silica polishing as

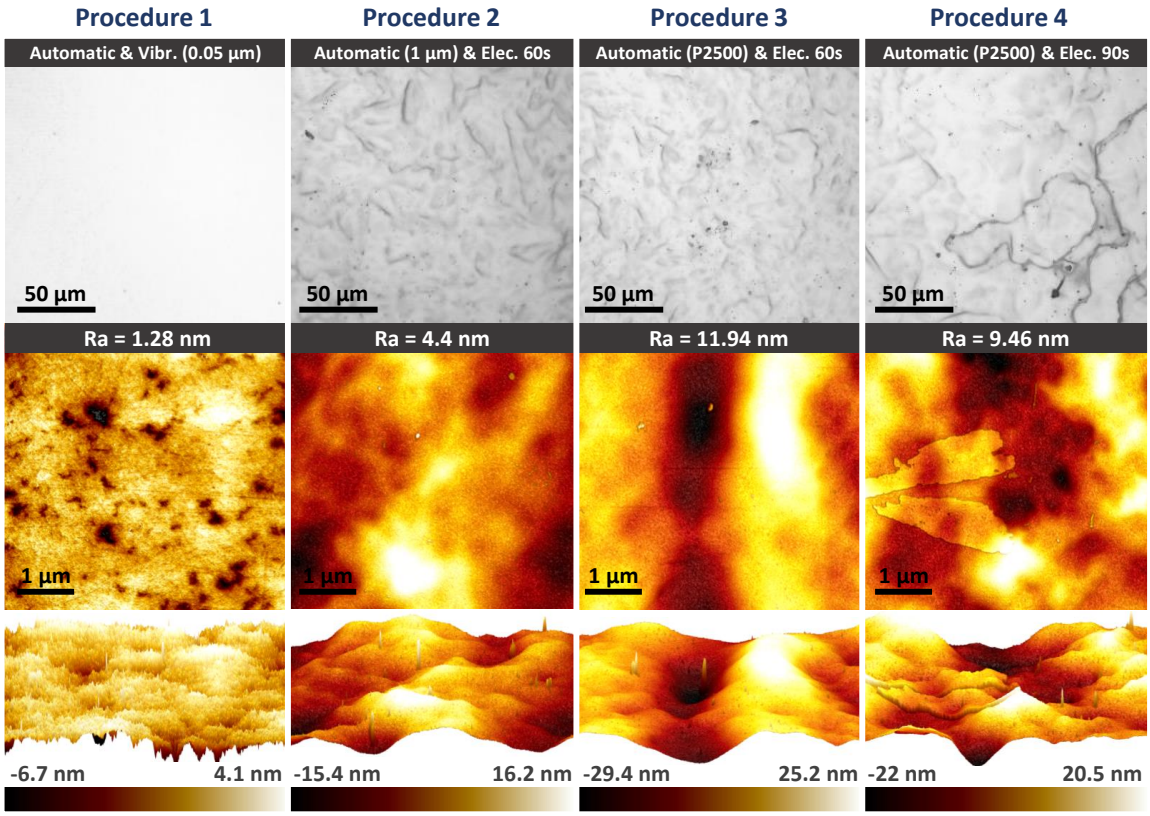

Figure 2.1: Comparison of surface topography of Nickel and arithmetical mean roughness (R_a) between four different polishing procedures prior to laser irradiation. The first row presents images taken by optical microscopy. The second and third rows present 2D and 3D AFM images respectively.

described in Table 2.1. Procedures 2, 3 and 4 consist of mechanical polishing followed by electrochemical polishing. For procedure 2, we began with the same automatic mechanical polishing as procedure 1, but followed with electrochemical polishing for 60s rather than vibratory polishing with colloidal silica. However, procedures 3 and 4 began with automatic polishing with SiC but were not followed by diamond (2 and 1 µm), and they were followed by electrochemical polishing for 60s and 90s for procedures 3 and 4, respectively.

Figure 2.1 compares the surface topography of the four different polishing procedures used prior to laser irradiation. The first row presents images taken by optical microscopy. We can clearly observe the difference between procedure 1, which is a clear mirror surface, and the other three surfaces, which are followed by electrochemical polishing. We can observe the presence of waves and also chemical corrosion on surface 4 since the electrochemical polishing was high (90s) compared to procedures 2 and 3.

AFM characterizations enable us to observe the surface roughness on a small scale of 5 μm^2 and also determine the minimum/maximum height and the arithmetical mean roughness (R_a) as well. We can conclude from AFM images of Figure 2.1 that surface 1 was more flat compared to wavy surfaces 2, 3 and 4. Figure 2.2 summarizes the R_a, minimum and

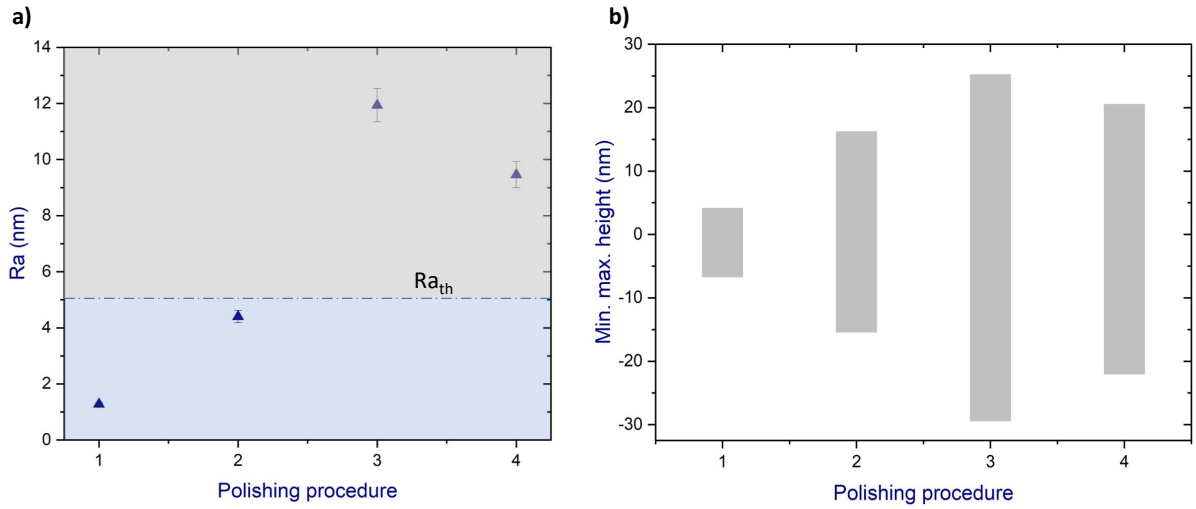

Figure 2.2: (a) Comparison of the arithmetical mean roughness between the four different polishing procedures prior to laser irradiation, with respect to Ra_{th}. (b) Comparison of minimum and maximum height of surfaces between the four different polished surfaces.

maximum height of surfaces. The arithmetical mean roughness threshold (Ra_{th}) has determined after different experiments. It is mandatory to have initial R_a < 5 nm in order to create self-organised nanostructures, as presented in the following chapters.

2.3 Femtosecond laser setup

2.3.1 Mach-Zehnder interferometer

A Coherent Legend Elite Series Ti: Sapphire laser was utilized. It provides linearly polarized pulses with a minimum pulse duration around 40 fs. The ultrafast amplifier delivers a 1 kHz repetition rate, 3 W output power, and a λ = 800 nm center wavelength. The ejection of the ultrashort pulse amplified by the pump laser is performed by a pulse picker.

Using a modified Mach–Zehnder interferometer, cross-polarized irradiation promotes self-organization by inducing isotropic energy deposition on the surface. The effect of crossed polarization is combined with an inter-pulse delay, which controls laser-induced structure creation. First, the incoming laser beam is divided in two by a non polarizing beam splitter with 50/50 ratio, represented by BS1 in Figure 2.3. These beams traverse two optical routes or arms before recombining at a second beam splitter BS2. A motorized stage controls the moveable arm's length, which leads to a temporal control between the first and second beam in the picosecond regime. Both arms energy can be controlled, as well as polarization, using $\lambda/2$ and polarizer.

At $\Delta t = 0$, temporal overlap occurs when the two optical pathways have the same length. The spatial overlap is verified on the autocollerator when the polarization angle is 0°. Each arm has a polarizer (P) to control the polarization angle between the two beams to

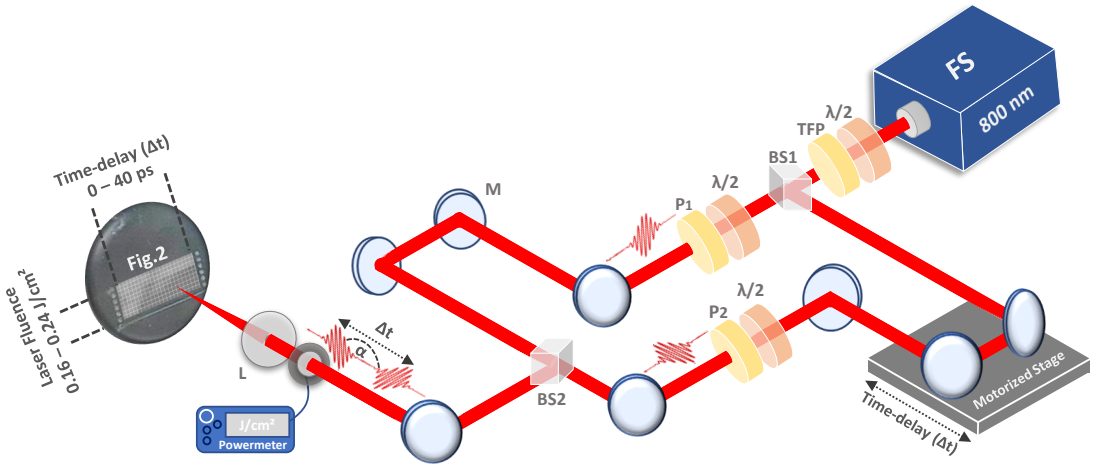

Figure 2.3: Schematic illustration of femtosecond laser double pulse setup with a temporal control. FS represents the femtosecond laser, BS1 and BS2 for the beam splitters, $\lambda/2$ for the half-wave plate. TFP for the thin film polarizer, P for the polarizer, M for the mirror and L for the lens with a focal distance of 25 cm from the sample.

.

Wavelength	Repetition rate	Pulse duration	Laser fluence	Time delay	N_{DPS}
800 nm	1 kHz	100 - 500 fs	0.16 - 0.24 J/cm²	0 - 40 ps	1 - 50

Table 2.4: Summary of the main irradiation parameters

achieve cross-polarization. The cross polarization is ensured by a polarizing beam splitter combined with a camera to assure the cross polarization with less time and more precision.

The light inside the Mach-Zehnder travels two different paths and recombines before being collimated by a 25 cm lens and irradiates a sample at normal incidence. The Gaussian profile at ($1/e^2$) has a spot size of $2w_0 \approx 60$ µm, where w_0 is the beam waist radius. The size of the laser spot is always measured before irradiation by the D² method [84]. A thin-film polarizer (TFP) which separates s and p polarization coupled with a $\lambda/2$ allows us to control the energy of pulses measured by a powermeter just before the Lens (L). Table 2.4 presents a summary of the main irradiation parameters

Larger irradiated surfaces were also carried out in this study in order to evaluate certain properties at larger scales, such as the wettability properties of surfaces after irradiation. In this case, the irradiations were made using a scanner from the SCANLAB company. The beam is sent into the scanner which treats, with point-by-point scanning, the surface of the sample positioned in a normal plane at its arrival. The scanner has a 88.2 mm F-theta scanning lens to keep the spot diameter as regular and as small as possible over the entire irradiation area. The scan is performed vertically (without round trip) with a non-synchronization of the beam frequency to that of the scanner. The parameters that can be modified in this configuration are: the overlap rate and coverage percentage (thanks to the distance separating the vertical and horizontal impacts), the number of laser shots per

point and the number of laser passes on the total surface. The scanning direction can also be modified to irradiate the surface horizontally or diagonally.

2.3.2 Laser fluence determination by Liu or D² method

The laser fluence is a critical parameter when irradiating a material under circumstances that might lead to ablation. In order to determine the irradiation parameters specific to each sample, it is first necessary to know the response of these samples to laser irradiation. For this, the theoretical diameter of the impacts as well as the damage thresholds of a sample were determined before irradiation by a method published by Liu [84]. This method, which is also called the D² method, makes it possible, by carrying out laser impacts at different energies, to obtain the threshold fluence of the material by measuring the diameter of the spots these impacts. This method makes it possible to obtain the theoretical diameters and threshold fluences at a given number of shots.

We first note F the surface fluence in J/cm², E the energy deposited on the irradiated surface in J and S this treated surface in cm². The fluence is then expressed in the following way:

$$F = \frac{E}{S} \tag{2.1}$$

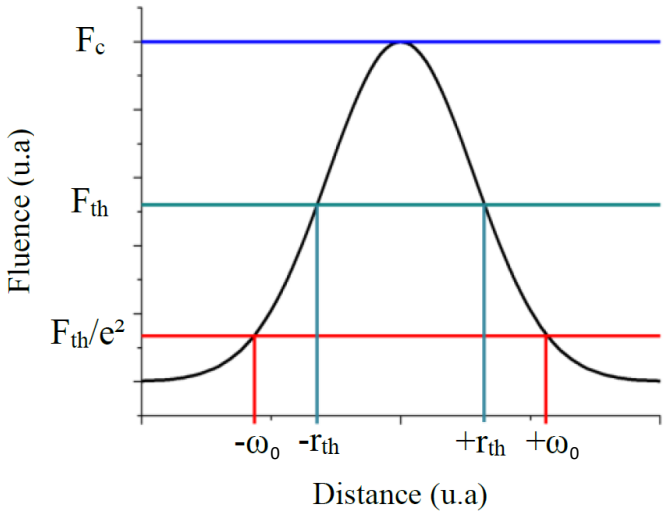

Figure 2.4: Radial distribution of the laser fluence. F_c represents the peak fluence, while F_{th} represents the ablation threshold fluence.

The fluence is a Gaussian function of the radius of the irradiated zone. It is represented in Figure 2.4 with remarkable points such as the peak fluence F_c (maximum fluence or peak fluence) and the threshold fluence F_{th} of the damage zone studied. We thus note:

$$F(r) = F_c\, e^{-\frac{2r^2}{w_0^2}} \tag{2.2}$$

with w_0 the radius of the laser spot.

Thus, F_c the maximum fluence of the Gaussian is written as follows:

$$F_c = \frac{2E}{\pi w_0^2} \tag{2.3}$$

Thus, we have:

$$F_{th} = \frac{2E}{\pi r_{th}^2} = \frac{2E}{\pi w_0^2} \tag{2.4}$$

We then note at the damage threshold:

$$F_{th} = F(r_{th}) = F_c\, e^{-\frac{2r_{th}^2}{w_0^2}} \tag{2.5}$$

Therefore:

$$r_{th}^2 = \frac{1}{2}\, w_0^2\, \ln(\frac{F_c}{F_{th}}) \tag{2.6}$$

And:

$$D_{th}^2 = 2\, w_0^2\, \ln(\frac{F_c}{F_{th}}) \tag{2.7}$$

As D^2 is a linear function of ln(E), and by extension of ln(F), we can then express w_0 the theoretical radius of the laser spot as a function of the slope of the line which we will denote a. From where:

$$w_0 = \sqrt{\frac{a}{2}} \tag{2.8}$$

The spallation, damage or ablation threshold fluence depends on which diameter is recorded during the characterizations of the impacts carried out. In the case of this study, the threshold fluence of interest is the threshold fluence of visible damage (by SEM) to the material. It is possible to determine the values of energies threshold (and therefore of fluences threshold) thanks to the exploitation of the curves $\mathbf{D^2 = f(ln(E))}$. In fact, by noting **a** and **b** respectively the slope and the ordinate at the origin of the straight line drawn for material 1 (for example), we have at the threshold:

$$a \times \ln(E_{th}) + b = 0 \tag{2.9}$$

Thus:

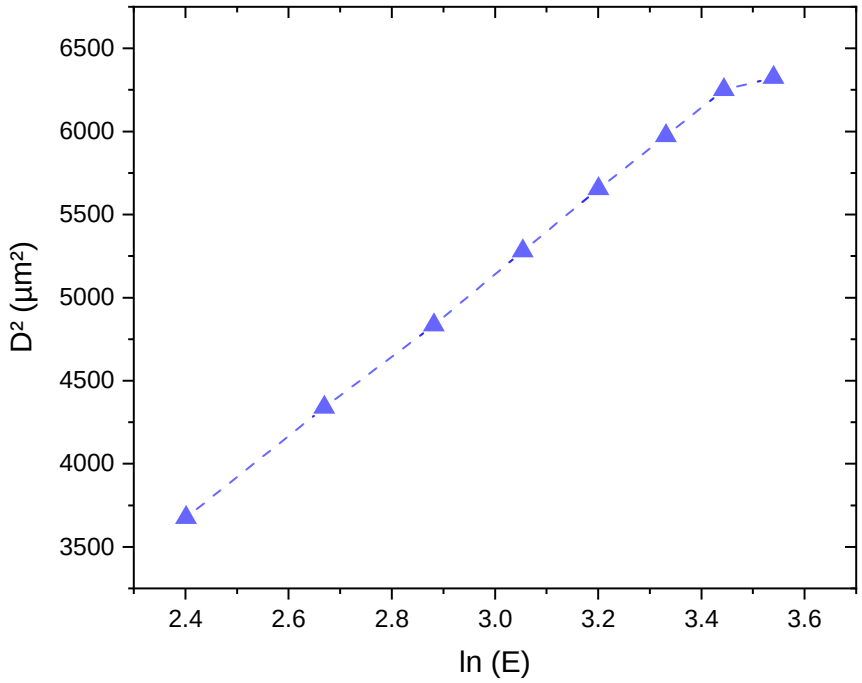

Figure 2.5: Linear regression performed on laser-induced ablation craters on a Ni sample at the focal plane in order to determine the beam waist using Liu method [84].

$$E_{th} = e^{-\frac{b}{a}} \tag{2.10}$$

For all the experiments, a method of realization has been implemented. This method includes four main steps, namely: characterization of the surface roughness of the samples before irradiation, measurement of the damage threshold fluence, determination of the irradiation parameters (fluence, number of shots, etc.), post-irradiation characterizations at the microscopic or macroscopic scale.

The first two steps, corresponding to the characterization of the surface state of the sample and the determination of the theoretical spot radius and the damage threshold energy, have been described previously. From the threshold energy E and the theoretical radius, it is possible to determine the threshold fluence F_{th} by:

$$F_{th} = \frac{2E_{th}}{\pi w_0^2} \tag{2.11}$$

For all the irradiations, the fluences are then defined and the corresponding energies are calculated. The equivalent powers are thus deduced, by dividing the energies by the repetition rate of the laser which is noted f:

$$P_{mes} = E \times f \tag{2.12}$$

In the case of this thesis, the rate being fixed at 1 kHz, the average P_{mes} power to be measured (in mW) is obtained by multiplying the energy (in µJ) by 1000 Hz. The average powers are then measured using a Gentec type power meter with a sensitivity of 200 mW. After the realization of these irradiations, the characterizations at different scales of the properties of the irradiated samples can be carried out.

2.4 Microscale and nanoscale characterization

The samples were characterized by a set of analytical methods, making it possible to obtain numerous information on the surface topography at nanometric scale. Different characterizations analysis and techniques making it possible to acquire topographic information at scales ranging from ten nanometers for scanning microscopy analyzes to the atomic scale with analyzes carried out by atomic force microscopy and transmission electron microscopy. The complementarity of these microscopy techniques is essential here, because when coupled, these methods can trace the evolution of surface roughness, their profiles before and after laser irradiation and depict the multi-scale structures that can be obtained by ultrafast laser irradiations.

2.4.1 Optical microscopy

The optical microscope is used as a preliminary characterization method after each femtosecond laser materials irradiation experiment, and also used to calculate the spot diameter to determine the beam waist radius. Optical microscopy provides quick and immediate access to the various impacts, allowing the selection of interesting results to be analyzed using high-resolution scanning electron microscopy. The optical microscope used is a Zeiss optical microscope with a DFC 32O digital color camera and "AxiovisionLE" software developed in a ZVI Carl Zeiss image format. The microscope used has a magnification range of 50 to 1000, depending on the samples to be studied.

2.4.2 Scanning electron microscopy SEM

The SEM (scanning electron microscopy) is a microscopic characterization tool providing much more resolved images, and at higher magnifications than a simple optical microscope. The secondary and/or backscattered electrons emitted during the passage of an electron beam scanning the surface of the material are analyzed by various detectors thus making it possible to characterize a great depth of field, a highly resolved image of the surface and sub-surface of the analyzed sample. As part of this study, a SEM FEI NOVA nanoSEM 2000 was used, allowing to obtain laterally resolved images up to ten angstroms. The working voltages used varied between 10 and 15 kV for working distances close to 5 mm. The

images were taken perpendicular or with surface tilt up to 30°, by analysis of the secondary electrons.

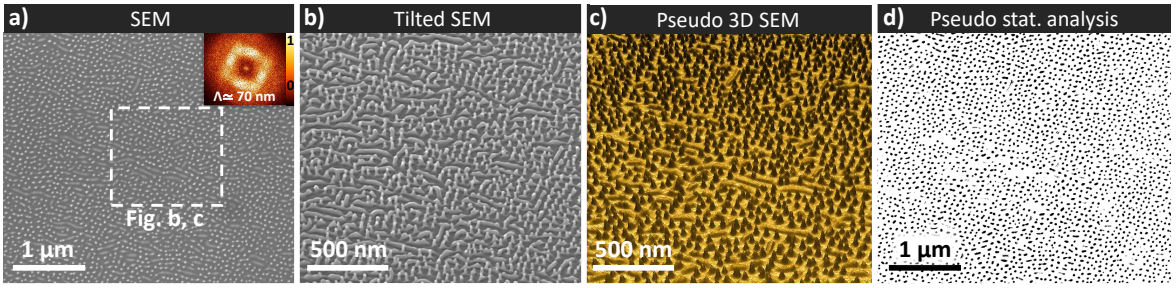

Figure 2.6: (a-d) Comparison between SEM (a) and tilted SEM images (b) with post treated SEM images, such as pseudo-3D SEM (c) and statistical analysis (d).

Figure 2.6 presents different SEM (a, b) and pseudo-SEM images (c, d). In this thesis, surface morphology is presented in different form, aiming to display complementary information and data. Figure 2.6 (a, b) presents SEM image and tilted SEM images respectively, presenting high aspect ratio nanostructures. However, Figures 2.6 (c, d) present post or pseudo-treated SEM images. Morphological analysis was performed by Gwyddion 2.55, which allowed us to visibly understand the shape of the nanostructures before verification by Atomic Force Microscopy, as presented in Figure 2.6 (c) . Figure 2.6 (d) displays statistical analysis performed using a function to count the number of items or observations based on [85]. This method examined in input an 8-bit image considering the values 0 for the background and 255 for the observation. The input image was then converted into a labeled image. The pixels values of the output image were between 0 and $N-1$, where N is the number of items (nanopeaks in Chapter 4), by associating input pixels equal to 255 spatially connected owing to decision trees. The analyzed size was 5x5 µm² and the error bars were represented by B-Spline and Bezier methods. Furthermore, 2D-FT was calculated also by using Gwyddion software, which gave us the periodicity of the self-organised nanostructures as presented in Figure 2.6 (a).

2.4.3 Atomic force microscopy AFM

Since the SEM does not provide quantified information on the scales of topographic surface roughness, analyzes were also carried out with an atomic force microscope. Probing the surface point by point using a tip located at the end of a cantilever moving through a piezoelectric module, the interactions (adhesion and repulsions) between the tip and the surface are recorded in order to recreate a three-dimensional image of the latter. In addition to providing a resolved image at the angstrom scale, quantitative information on the roughness profile and different surface properties can be obtained, such as electrical or mechanical properties (conductivity, Young's modulus, etc.). Although having the advantage of having very high spatial resolutions, AFM has the disadvantage of the acquisition time and the size of the maps produced, which are directly correlated. In addition, the lateral resolution is limited to the characteristics and quality of the tip used.

In order to produce the maps presented in this thesis, an AFM Dimension ICON from the company Bruker was used. Several maps were carried out on mainly non-irradiated samples in order to obtain the roughness profile as well as the peak-to-peak distances between the minimum and maximum roughness. Mappings of 5 µm, 1 µm, 500 nm and 200 nm scan ranges were therefore produced using the Scan Assist in Air mode using a tip specific to this mode in silicon nitride, with a scan frequency of 1 Hz and a resolution of 2 nm.

Scan Assist / Air			**HR Super-Sharp / Tapping**		
Cantilever	Tip	AFM Scan	Cantilever	Tip	AFM Scan
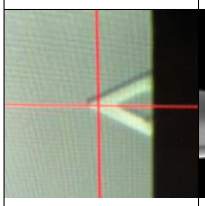	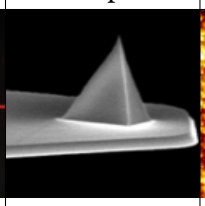	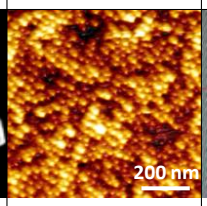	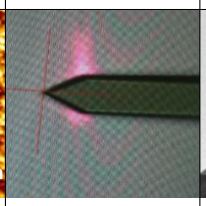	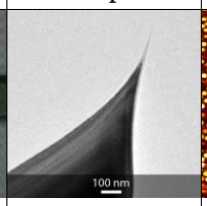	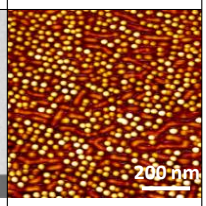
B.s. coating: Aluminum	**Shape:** Triangular	**Structures:** Nanopeaks	**B.s. coating:** Gold	**Shape:** Super-Sharp	**Structures:** Nanopeaks

Table 2.5: Comparison between the Scan Assist Air and HR Super-Sharp probes. The comparison Cantilever shape and back side coating, Tip shape and finishing, same nanopeaks characterized by two different probes.

However, it was not possible to characterize high aspect ratio nanopeaks with the scan assist probe due to its limitation. After investigations, we have found the optimal probe to characterize these type of structures in tapping mode, which is the OPUS "240AC-SG". Comparison between the two probes is displayed in table 2.5. Thanks to its super sharp tip, it was possible to characterize the surface morphology in 3D in tapping mode. The probe cantilever was gold coated to ensure high and stable laser reflectivity with a diamond-like spike designed for high resolution AC mode AFM imaging of soft samples and a resolution < 1nm. Topographical interpretations were performed using NanoScope Analysis software.

2.4.4 Transmission electron microscopy TEM

Combined, scanning and atomic force electron microscopes make it possible to obtain highly resolved images by coupling qualitative information on the surface and sub-surface of the sample with quantitative information on the relief of roughness and topography present on the surface. On the other hand, they unfortunately do not provide any information on the interior of the specimen, except in the case of studies carried out on cross-sections. As these sections are relatively difficult to obtain by direct cleavage in the context of this study, FIB (Focus Ion Beam) sections were preferentially produced by focused gallium ion beam in order to extract thin sections to be analyzed by transmission electron microscopy.

The TEM (Transmission Electron Microscopy) and STEM (Sanning Transmission Electron Microscopy) modes are similar image acquisition modes used during analyzes with a transmission electron microscope. To do this, an electron gun delivers a beam of high en-

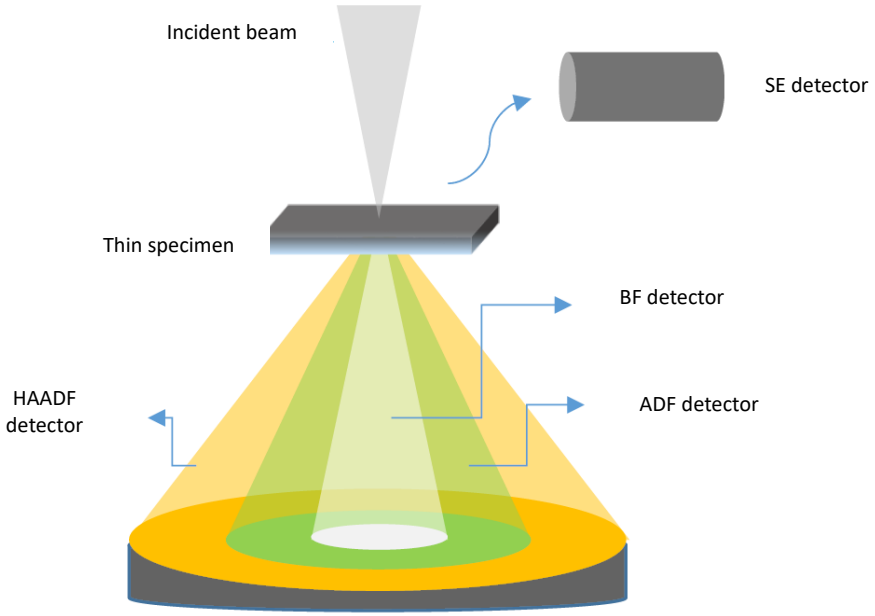

Figure 2.7: Schematic of the HAADF, conventional annular dark-field (ADF) and BF detectors in a TEM.

ergy electrons projected through a thin sample not exceeding 100 nm in thickness. Thus, an image visualized in two dimensions of an area observed and analyzed in three dimensions is obtained, and sometimes provides key information on the interior of the material studied. In our study, the images obtained were characterized using the TEM NEO-ARM from Jeol in STEM mode at 200 kV with different detectors. The main detectors used are BF (Bright Field) and HAADF (High-Angle Annular Dark-Field). They are both very complementary, thus making it possible to have information on topographic and chemical contrasts, structural changes or even on the presence of crystalline defects. Overall, the images acquired have a much higher lateral resolution than that of the SEM, thus being able to go up to 1 to 2 Angstroms. On the other hand, the main drawback of the analyzes carried out by transmission microscopy remains the sample preparation step, which is relatively long and complex. Figure 2.7 presents a schematic of the HAADF, conventional annular dark-field (ADF) and BF detectors in a TEM.

2.5 Physico-chemical analysis

Physico-chemical analysis aims to compare the wetting behavior of a sample surface, before and after texturation by measuring the contact angle of water droplet on the surface. The contact angle measurement reports the ability of a liquid to spread on a surface by wettability. In practice, a drop of liquid with a volume of ≈ 3 µl, usually ultrapure distilled water, is deposited with a syringe on the surface of the sample to be analyzed. Each measurement of the contact angle is carried out for a period of 30 to 60 seconds in order to verify the occurrence of the thermodynamic equilibrium (stability of the drop on the substrate surface).

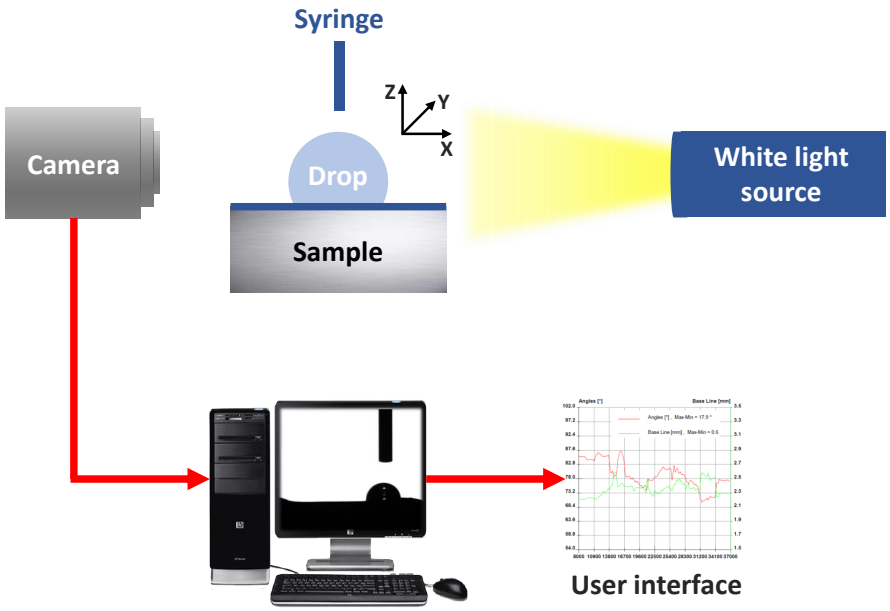

Figure 2.8: Photography of the dropping device and diagram of the operating principle.

During the measurement a 360° rotation of the sample holder is performed which allows a measurement of the contact angle at each point around the drop. The first step of the drop dispensing protocol is to adjust the sharpness of the camera by focusing on the needle of the syringe whose external diameter is known, which will then allow to calibrate the resolution of the image. Once the calibration is done, a determined volume of liquid is injected. Finally, we drop on the surface of the substrate. The measurement of the angle is done from images captured by a PC via a camera (Figure 2.8). The Digidrop operating software from GBX allows the automatic extraction of the contact angle, using different algorithms (automatic methods of interpolation by polynomial or by arcs of circles, semi-automatic methods or manual methods).

2.6 Biological functionalization

The antibacterial tests were performed at SAINBIOSE. Sterilization process: the samples received an ultrasonic bath cleaning (Triton 3% in demineralized water; 15 min and demineralized water; 15 min) and an autoclaving treatment (120°C; 30 minutes). Staphylococcus aureus ATCC 43866 strain was isolated on brain–heart infusion (BHI) agar plates at 37°C and grown in a BHI broth for 24 hours at 37°C under agitation (160 rpm). 1 mL of S. aureus broth diluted at 2.107 CFU/mL was incubated over titanium samples at 37°C under agitation (160 rpm). After 24 hours of incubation, BHI broth was removed; bacteria were stained with calcein AM (Invitrogen; C3099) at 10µg.mL^{-1} in Phosphate-Buffered Saline (PBS) for 20 min at 37°C; washed with PBS and fixed with Paraformaldehyde 3.7% for 40 min at RT; washed and kept in PBS. Fluorescent microscopy (ZEISS LSM 800 Airyscan, Oberkochen,

Germany) was used to image stained-bacterial samples. Bacterial images analysis was performed with the ImageJ software by measuring mean fluorescence in 15 areas (90 mm^2) per condition and making a percent ratio with local polished control. Statistical analyses were performed using GraphPad Prism 8 software. Bacterial data are presented as mean $\pm$ SEM, statistical analyses were performed using Mann-Whitney U test.

2.7 Conclusion

In this chapter, we have outlined the various experimental approaches used in this work to investigate the competition between laser-induced privileged order of matter and nanostructures evolution. The first section focused on sample polishing (both mechanical and electrolytic polishing) and surface preparation for laser irradiation. The second section described the laser components, followed by an illustration of the laser setup that allows for fs-double pulse creation utilizing a Mach-Zehnder interferometer. The Liu method for determining laser fluence is also explained. Atomic force microscopy AFM, scanning electron microscopy SEM, and transmission electron microscopy TEM are also employed to analyze LIPSS and nanostructures features. Finally, physico-chemical analysis is performed to identify the hydrophilic or hydrophobic character of the irradiated samples.

Chapter 3

Self-organization regimes in the tens of nanometer scales

Perseverance leads to achievements,
Achievements leads to fulfillment &
Fulfillment fuels Perseverance

– Marie Ramez Nakhoul

3.1 Introduction

Laser-irradiated surface is the paradigm of a self-organizing system, as coherent, aligned, chaotic, and complex patterns emerge at the microscale and even the nanoscale. A spectacular manifestation of dissipative structures consists of different types of randomly and periodically distributed nanostructures that arise from homogeneous metal surface. The noninstantaneous response of the material reorganizes local surface topography down to tens of nanometers scale modifying long-range surface morphology on the impact scale. Under ultrafast laser irradiation with a regulated energy dose, the formation of nanopeaks, nanobumps, nanohumps and nanocavities patterns with 20-80 nm transverse size unit and up to 100 nm height are reported. We show that the use of cross polarized double laser pulse adds an extra dimension to the nanostructuring process as laser energy dose and multi-pulse feedback tune the energy gradients distribution, crossing critical values for surface self-organization regimes. Strongly influencing the light coupling, we reveal that initial surface roughness and type of roughness both play a crucial role in controlling the transiently emergence of nanostructures during laser irradiation.

3.2 Influential parameters on nanostructure formation:

3.2.1 Polarization angle

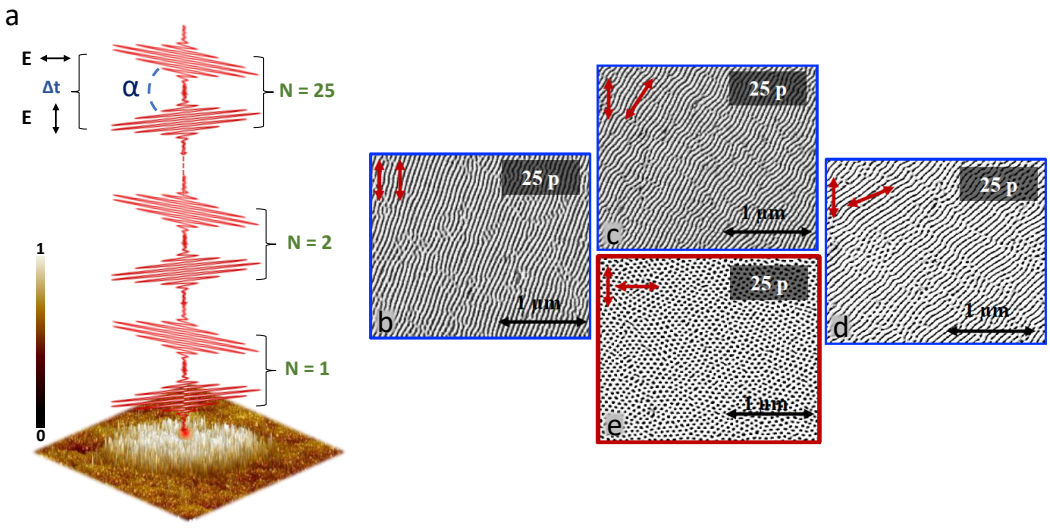

Figure 3.1: a) Schematic illustration of ultrafast laser double pulses at a fixed N_{DPS} of 25, time delay Δt of 24 ps, laser fluence of 0.24 J/cm² and different angle α . b-e) SEM micrographs of four different impacts, with different polarization angle α. b-c) Nanostripes structures at $0° \leq \alpha \leq 45°$. d) Transformation regime of nanostripes and organised nanocavities at α = 45°. e) Formation of self-organised nanocavities at α = 90°. Adapted from [21].

A cross-polarization strategy is used to promote isotropic energy deposition that fosters self-organization. The polarization state of the incident pulses in the double-pulse sequence has a major influence on the nanostructures created. As previously described in Chapter 2, the polarization angle is controlled by using a half-wave plate into the Mach Zehnder interferometer paths. Figure 3.1 shows SEM images of several nanostructures created using fs-double pulse sequences with varied laser polarization. The time-delay between the two pulses is 24 ps, with a N_{DPS} of 25 at a peak fluence of 0.24 J/cm².

Figure 3.1 (b-e) present the development of self-organised nanocavities on the surface of Ni (001) as a function of laser polarization. When 25 double pulse sequences impinge on the surface with the same polarization (α = 0°), nanoripples with periodicities close to 60 nm are created parallel to the incident polarization as shown in Figure 3.1 (b). When the polarization of the second pulse is rotated by a half-wave plate ($0° \leq \alpha \leq 45°$), the nanoripples pattern appears, with no preference to the polarization orientation as presented in Figure 3.1 (c). The nanoripples shape has changed in Figure 3.1(d) when the polarization angle has increased $45° < \alpha < 90°$, and a transition regime is observed as nanocavities appeared between the nanoripples. At α = 90°, or when the polarization of the two-delayed pulses is crossed, self-organised nanocavities are generated on the surface.

3.2.2 Number of double pulse sequences

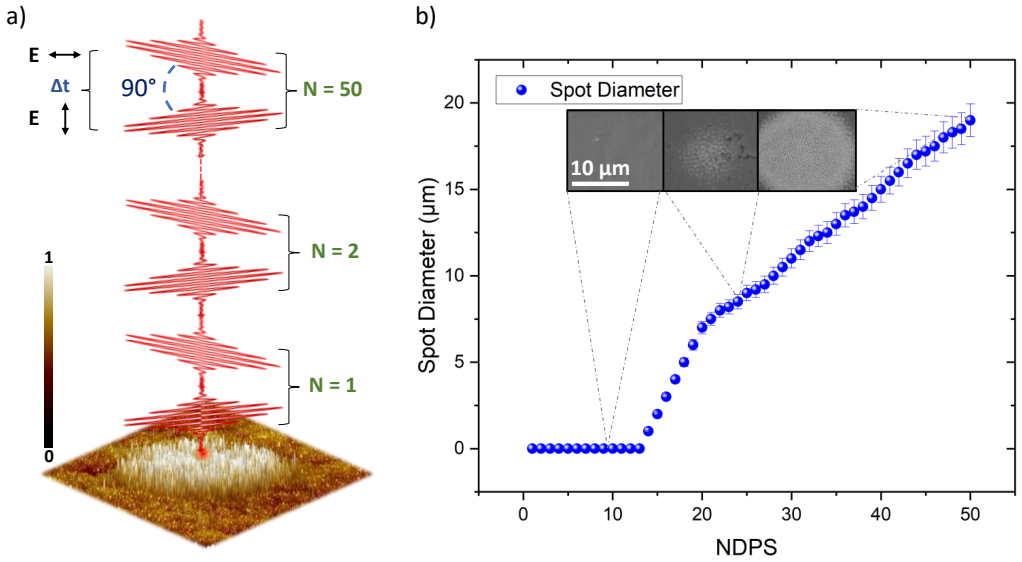

Figure 3.2: a) Schematic illustration of experimental self-organization regimes induced by bursts of ultrafast laser double pulses at a fixed polarization angle of α = 90°, time delay Δt of 8 ps, laser fluence of 0.18 J/cm² and different number of double-pulses sequences $1 \leq N_{DPS} \leq 50$. b) Spot diameter evolution with increasing N_{DPS} that underlines the role of laser dose in controlling the impact area. SEM micrographs of three different impacts are also presented with distinct number of double pulse sequences (10 , 25 and 50 pulses).

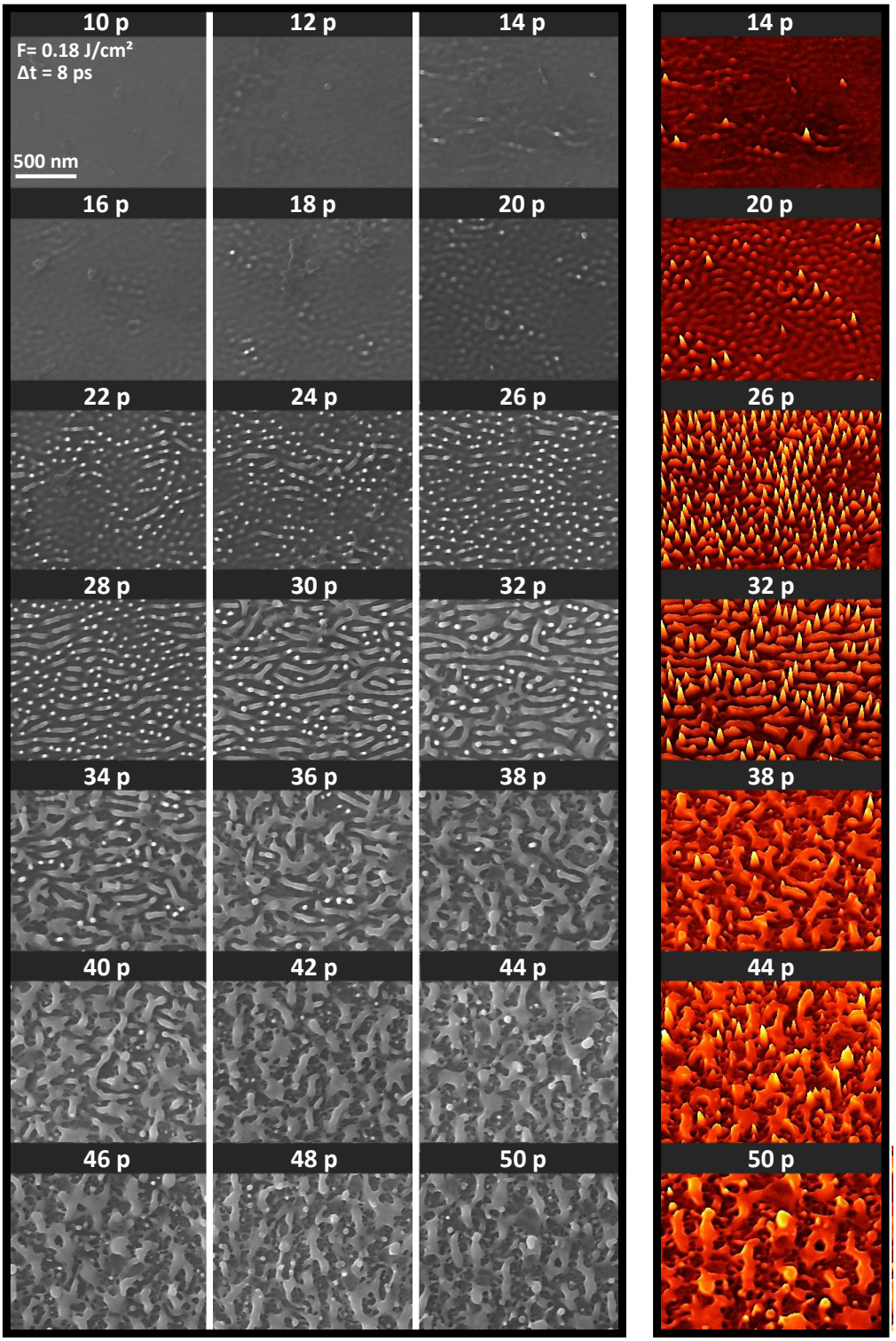

Figure 3.3: Pseudo-3D (right column) and scanning electron microscopy of a Ni(001) crystal irradiated by different number of double pulse sequences N_{DPS} between 10 and 50 pulses at an incident laser fluence of 0.18 J/cm² and a time delay of 8 ps between both laser crossed polarizations. Pulse-to-pulse dynamics of the nanopeaks formation.

As previously stated, laser polarization plays an important role in controlling surface topography and nanopatterns morphology. The laser dosage is also important in producing diverse patterns. By setting the peak fluence to 0.18 J/cm² and the time delay to 10 ps, Figure 3.2 illustrates the spot diameter evolution with increasing N_{DPS} that underlines the role of number of double pulses sequences in controlling the impact area. As observed in Figure 3.2 (b), the impact diameter started increasing from N_{DPS} > 12 p to reach a diameter of 5 µm at N_{DPS} = 12 p and 10 µm at N_{DPS} = 30 p. The impact diameter continues increasing while increasing the N_{DPS} to reach ≈ 20 µm at 50 pulses.

Figure 3.3 presents pseudo-3D and scanning electron microscopy irradiated at the same parameters presented in Figure 3.2. In this section, we would like to shade the light on the critical role of N_{DPS} in nanostructures formation and organisation. Thus, the laser fluence was fixed here at 0.18 J/cm² and the time-delay Δt to 8 ps. The N_{DPS} was varied between 0 and 50 pulses, aiming to understand its crucial role in nanostructures self-organization. For example, increasing the number of pulses from 28 to 30 p can completely change the nanostructures type and concentration. More pulse-to-pulse dynamics will be discussed in Chapter 4.

For a 1 p $\leq N_{DPS} \leq$ 10 p, there is no nanostructures observed and higher number of double-pulses sequences are required, here the total irradiated energy was below surface modification or nanostructures formation threshold. However, for 12 p $\leq N_{DPS} \leq$ 14 p, some nanoroughness has appeared on the irradiated surface without any special organization. The pseudo-3D image at N_{DPS} = 14 p shows the appearance of few peaks on the surface. By increasing the number of double-pulses sequences to 16 p $\leq N_{DPS} \leq$ 20 p, we started to observe some organization of small peaks, and their concentration and height increase progressively at N_{DPS} = 26 p.

Furthermore, while increasing the number of double-pulses sequences to 28 p $\leq N_{DPS}$ $\leq$ 32 p, the peaks concentration has decreased and other structures started appearing at N_{DPS} = 34 p. Finally, for 38 p $\leq N_{DPS} \leq$ 50 p, the organized nanostructures has disappeared and they were replaced by chaotic nanostructures. Therefore, in the following studies, we fixed our number of double-pulses sequences close to the organization regimes, at $N_{DPS} \approx$ 25 p.

3.2.3 Laser fluence

Laser fluence plays an essential role in controlling surface topography. As described in the experimental procedure previously, the D²-method is performed by controlling the laser fluence and calculating the impact diameter. Moreover, different regimes can be controlled by laser fluence as presented previously in Figure 1.3.

Increasing laser fluence over the melting threshold but below the phase explosion threshold causes cavitation and spallation, the separation of a molten layer from the bulk of the material. Thus, cavitation weakens the mechanical stability of the area, causing liquid to eject from the target. Local fluence changes in a Gaussian beam laser and spallation dynamics may disturb liquid layer stability. In this work, we are controlling the surface morphology by using low laser fluence before spallation and ablation regimes.

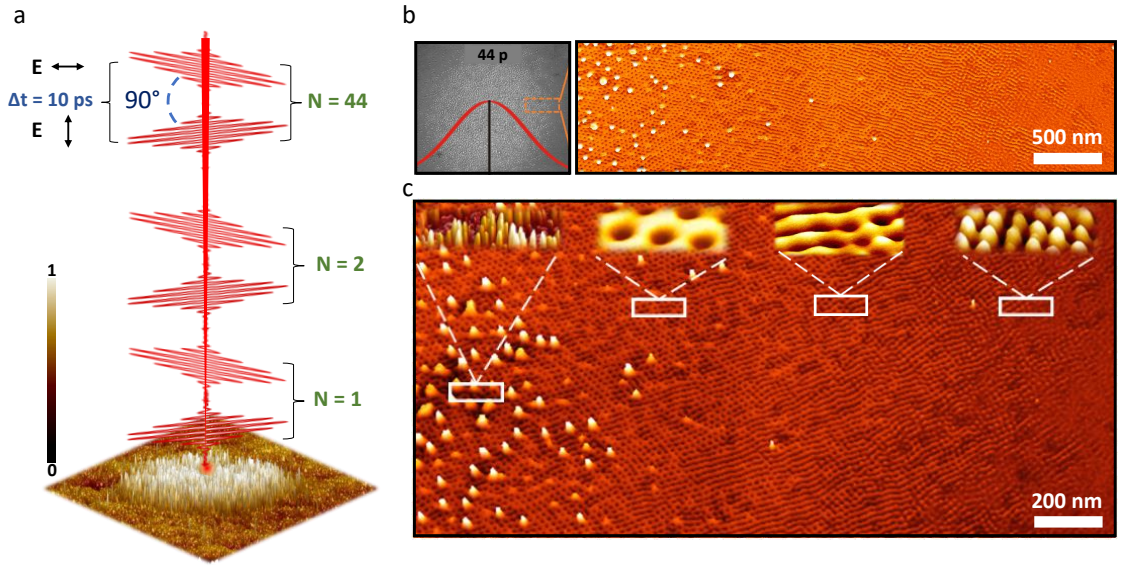

Figure 3.4: a) Schematic illustration of ultrafast laser double pulses at a fixed Δt = 10 ps, N_{DPS} of 44, laser fluence of 0.18 J/cm² and polarization angle α of 90°. b) SEM image of the Gaussian laser spot at the same laser parameters presented in (a). c) The right region of the Gaussian laser spot of (b), showing the significant role of laser fluence in controlling different types of nanostructures as presented in the 3D AFM images.

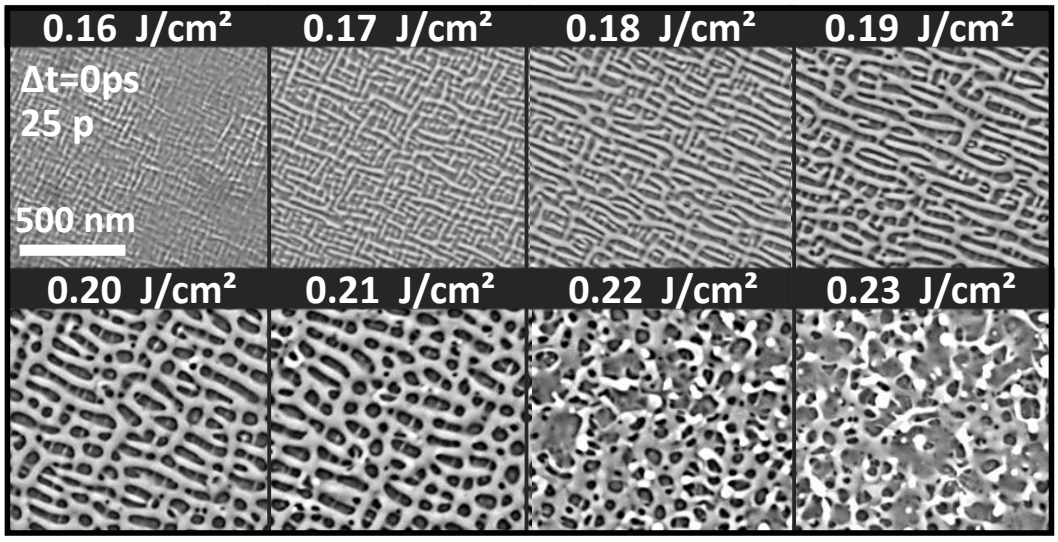

Figure 3.5: Scanning electron microscopy of a Ni(001) crystal irradiated at a Δt = 0 ps, N_{DPS} of 25, polarization angle α of 90° and different incident laser fluences between 0.18 and 0.24 J/cm². Different self-organisations regimes are presented and controlled by laser fluence.

Figure 3.4 (b) presents a Gaussian laser spot diameter at a fixed Δt= 10 ps, $N_{DPS} = 44$ and laser fluence at 0.18 J/cm². Figure 3.4 (c) depicts the right region of the Gaussian laser spot of (b), demonstrating how nanopatterns can be easily controlled by varying the laser

peak fluence (Gaussian). The presence of distinct nanostructures on the laser spot periphery emphasizes the importance of laser peak fluence in the formation of diverse surface topographies, which are clearly presented in the 3D AFM images.

Figure 3.5 presents the formation of analogous surface topography by only varying the laser fluence between 0.18 and 0.24 J/cm², at a fixed N_{DPS} of 25 ps, Δt of 0 ps and polarization angle α of 90°. At 0.16 J/cm², some roughness started to appear on the irradiated surface. While increasing the fluence to 0.17 and 0.18 J/cm², crossed organized nanostructures appeared on the surface. At higher laser fluence of 0.21 J/cm², the crossed nanostructures has transformed to organized nanostructures with voids. Furthermore, while increasing the laser fluence to 0.23 and 0.24 J/cm², the organization has disappeared and chaotic nanostructures appeared. Therefore, the role of laser fluence is not only to control the material phase, but also to control surface topography and nanostructure shape. Thus, laser fluence is has key role in controlling surface organization on the nanoscale.

3.2.4 Time delay (Δt)

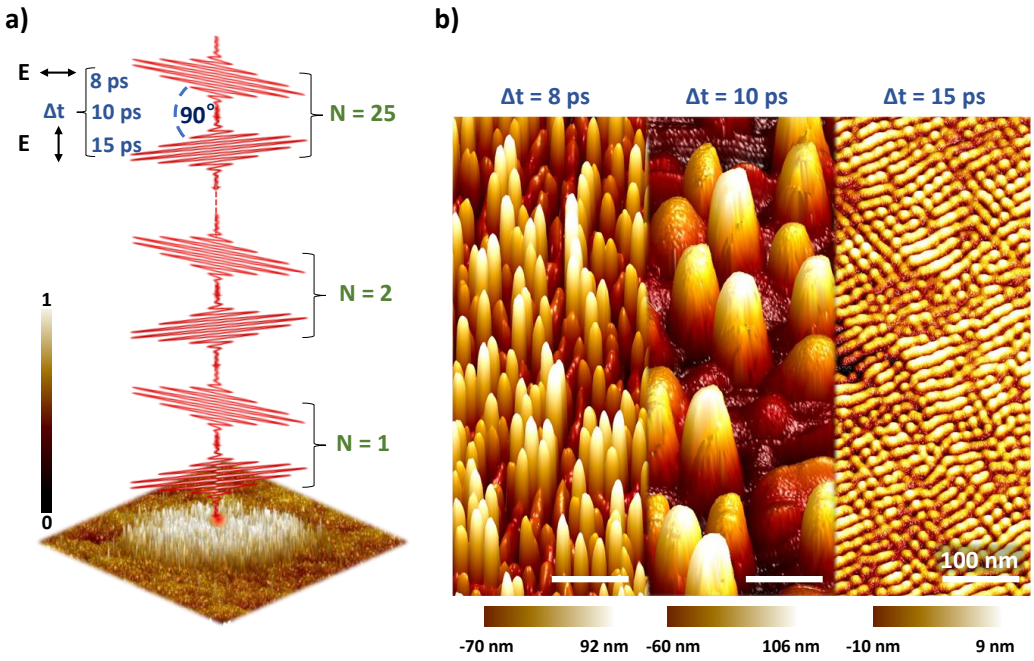

Figure 3.6: a) Schematic illustration of ultrafast cross-polarized laser double pulses at a fixed laser fluence of 0.19 J/cm², $N_{DPS} = 25$, polarization angle α of 90° and time delay Δt of 8 ps, 10 ps, 15 ps and 25 ps. b) 3D AFM images of three types of nanostructures at the same laser parameters, just by controlling the time delay between 8, 10 and 15 ps.

To investigate the substantial time-delay role in nanopattern control, the laser peak fluence F and N_{DPS} were set at 0.19 J/cm² and 25 respectively, as shown in Figure 3.6. As previously described in Chapter 2, the Mach-Zehnder interferometer allows us to alter the temporal delay between the first and second pulses, giving us fine control of the surface

morphology. Figure 3.6(b) shows three distinct nanostructures created with the same laser fluence and N_{DPS} of 0.19 J/cm² but at three different time delays 8, 10 and 15 ps.

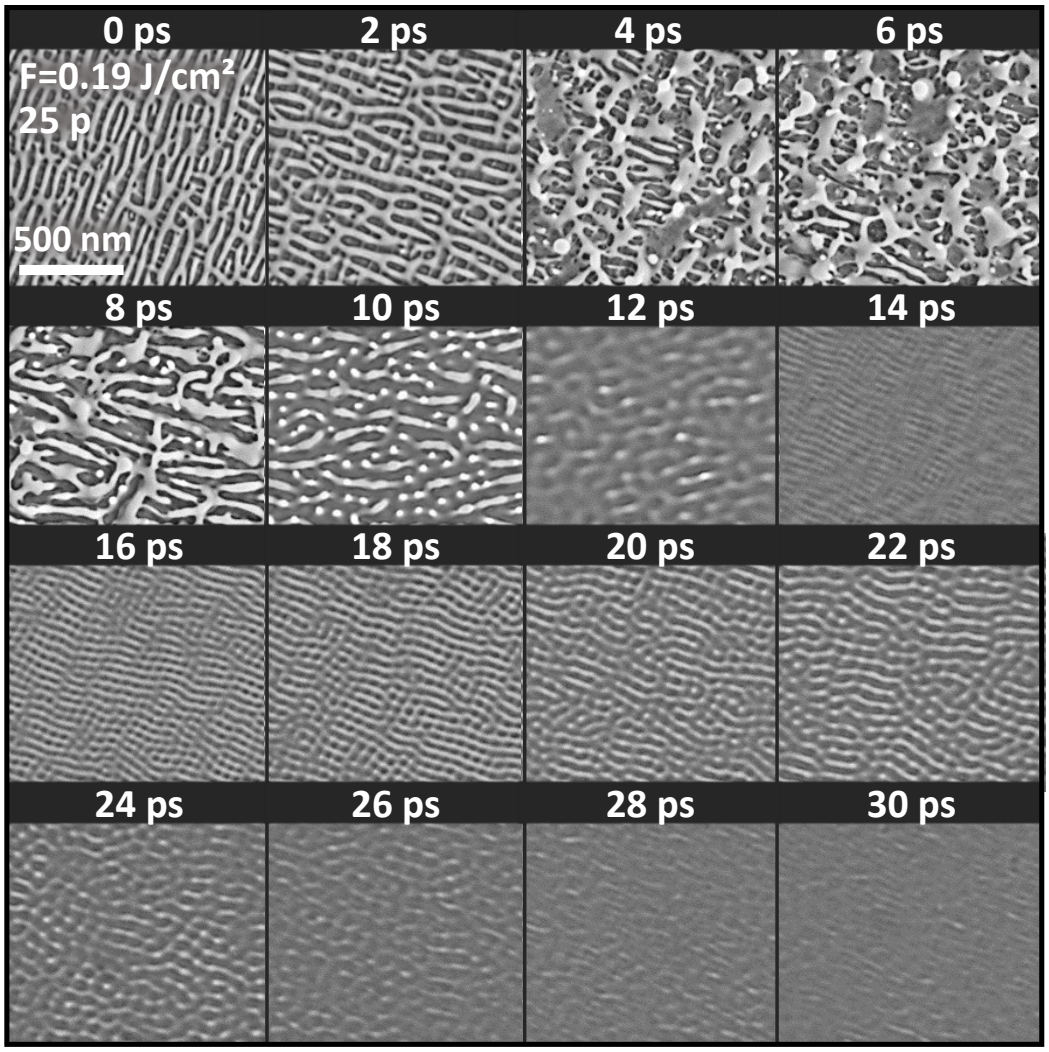

Figure 3.7: Several organization regimes controlled by different time-delay Δt between the two cross-polarized pulses at a fixed number of double-pulses sequences of 25, a pulse duration of 150 fs and fixed laser fluence of 0.19 J/cm².

Several organization regimes are presented in Figure 3.7 controlled by different time-delay Δt between the two cross-polarized pulses at a fixed number of double-pulses sequences of 25 and fixed laser fluence of 0.19 J/cm² for Figure 3.7. It is so clear that time delay can finely control the surface topography, just by increasing the time delay of 2 ps, the nanostructures organizations and shape can be tuned. For example, crossed nanostructures are observed at Δt = 0 ps. At larger time-delay between 4 ps $\leq \Delta t \leq$ 8 ps, chaotic nanostructures are observed. At larger time-delay of 10 ps peaks are observed which will be transformed on cavities at 16 ps.

Thus, the time delay is considered as a key parameter to break the surface isotropy and the formation of self-organized nanopatters at different time delays by using crossed polarization. The time-delay has a significant role since it controls the hydrodynamic state

of the liquid metal before resolidification. An interplay between laser fluence and time delay will be presented in the following sections, after defining and fixing other significant parameters such as pulse duration and initial surface roughness.

3.2.5 Pulse duration

During the early discovery of the self-organised nanostructures, the laser pulse duration was often compressed to about 150 fs. In general, low pulse duration allows the production of organized nanostructures such as nanocavities and nanopeaks, but high pulse duration in the nanosecond range does not.

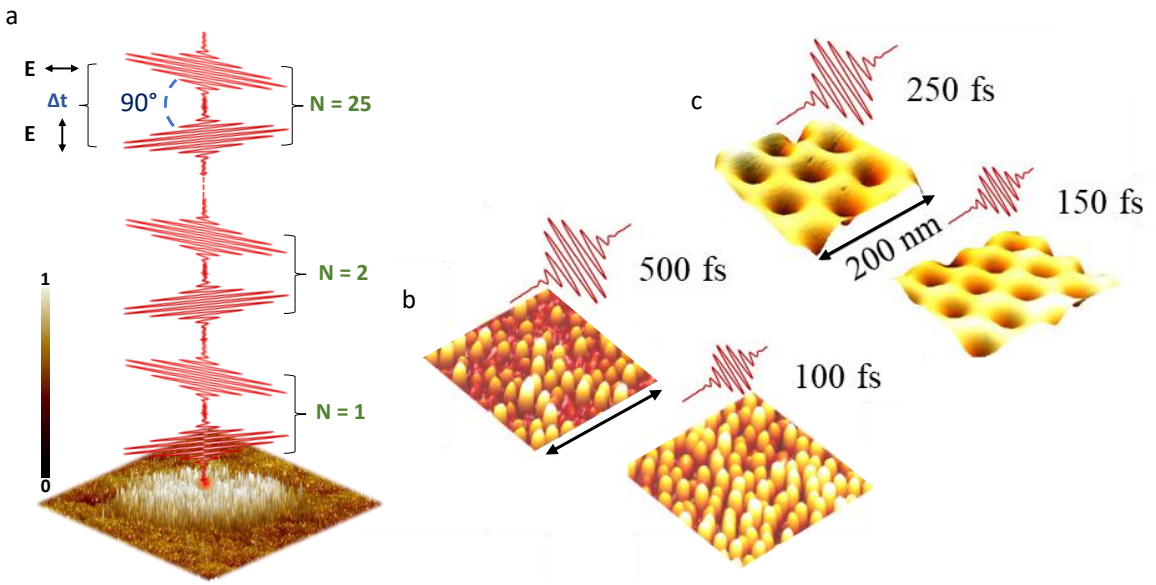

Figure 3.8: a) Schematic illustration of ultrafast laser double pulses at a fixed laser fluence, time delay, N_{DPS} of 25 and polarization angle α = 90°. b) 3D AFM images of nanopeaks at different pulse duration of 500 and 100 fs, showing different distribution and concentration on the surface. c) 3D AFM images of nanocavities at different pulse duration of 250 and 150 fs, showing different periodicity and width on the surface.

Several experiments were performed to understand the role of pulse duration in controlling surface morphology. Figure 3.8(a) depicts the influence of pulse duration at fixed time delay, laser fluence, and N_{DPS}. The nanopeaks concentration has been controlled by the pulse duration, as shown in figure 3.8(b). We can observe that by lowering the pulse duration from 500 to 100 fs, the concentration has almost doubled. Concerning the nanocavities, the concentration and shape of the cavities has changed from 50 nm depth to 25 nm simply by lowering the pulse duration from 250 to 150 fs, as presented in figure 3.8(c).

As a result, pulse duration is also an important factor for determining the form and concentration of the produced nanostructures, making them suitable and feasible for various applications.

3.2.6 Initial surface roughness

Initial surface topography plays an essential role in nanostructure formation. Several polishing procedures were developed to obtain distinct initial surface topographies with different initial arithmetic surface roughness (R_a). Figure 3.9 depicts the effects of initial surface roughness when all laser settings are maintained constant (laser fluence = 0.18 J/cm², N_{DPS} = 25, Δt of 25 ps, pulse duration of 150 fs and α = 90°). Irradiation in these conditions will, in general, result in the creation of self-organized nanocavities.

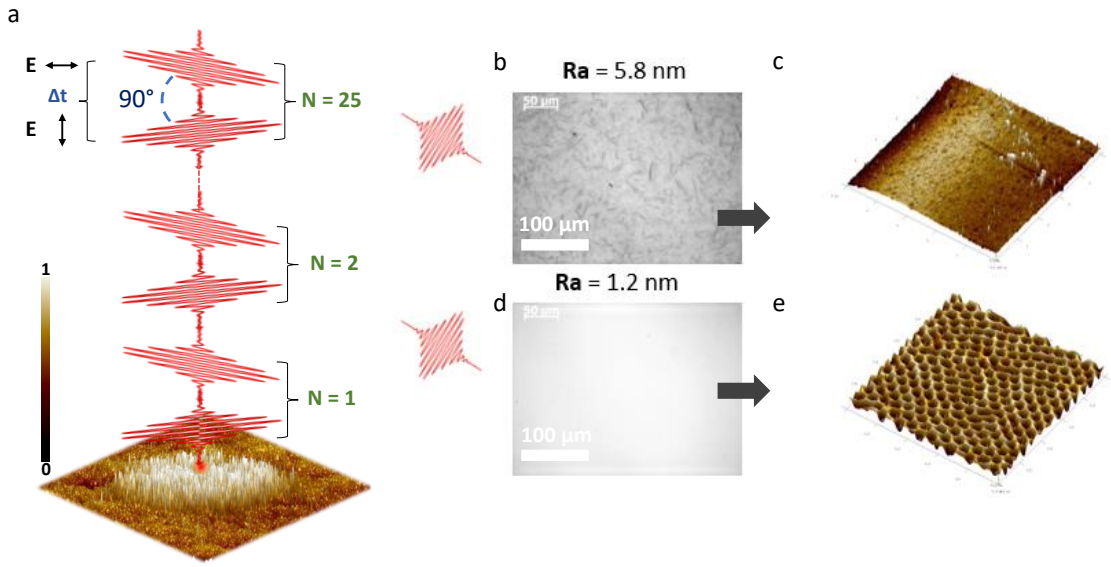

Figure 3.9: a) Schematic illustration of experimental organization regimes induced by bursts of ultrafast laser double pulses at a fixed laser fluence = 0.18 J/cm², N_{DPS} = 25, Δt of 25 ps, pulse duration of 150 fs and α = 90°, varying the initial surface roughness prior to laser irradiation. b) Optical microscopy image of initial surface prior to laser irradiation with a high initial arithmetic surface roughness R_a = 5.8 nm. c) 3D AFM image of surface topography after laser irradiation of (b). d) Optical microscopy image of initial surface prior to laser irradiation with a low initial arithmetic surface roughness R_a = 1.2 nm. e) 3D AFM image of surface topography after laser irradiation of (d).

In Figure 3.9(b), we present an image of initial surface prior to irradiation taken by optical microscopy, showing a manually polished surface. The image presents a rough surface, the arithmetic surface roughness was tested by AFM and present an R_a of 5.8 nm. Irradiating in these conditions did not lead to any nanostructures formation. However, for a well polished surface by conventional method previously explained in Chapter 2, we have obtained a well organised network of nanocavities.

Therefore, the R_a threshold Ra_{th} was found to be 5 nm on AFM, on a scan of 5×5 µm². A R_a > 5 nm, will not permit the formation of different types of the presented nanohumps and nanocavities previously.

3.2.7 Initial type of surface roughness

Initial surface topography plays a crucial role in the creation of nanostructures. Several polishing procedures were created in order to achieve a variety of initial surface topographies and arithmetic surface roughness values (R_a). A R_a greater than 5 nm prevents the production of previously described nanopeaks and nanocavities.

As presented in Figure 3.10(b) and (c), the initial R_a values of samples 1 and 2 are greater than Ra_{th}. Sample 1 was mechanically polished with coarse paper up to P2400, followed by diamond polishing of 3 µm and 1 µm and vibratory polishing with colloidal silica of 0.05 µm for several hours, which guarantees a mirror surface with a very low arithmetic roughness. Kurtosis (K_u) statistical characteristics were utilized to define the type of initial surface roughness and spike sharpness. If K_u is greater than 3, the surface is considered "spiky," and if it is less than 3, it is considered "bumpy." If K_u = 3, the surface's surface roughness is fully random. For sample 1, the K_u value is 7.54, indicating a spiky surface with Ra < Ra_{th}

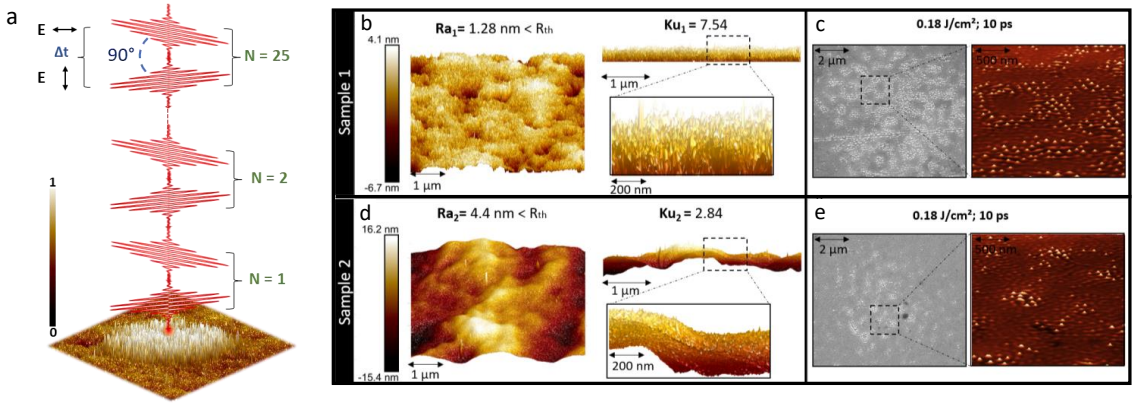

Figure 3.10: a) Schematic illustration of ultrafast laser double pulses at a fixed N_{DPS} of 25 and angle α = 90°. Initial surface topography of two different samples polished by different procedures (Mechanical polishing in (a) and Electrochemical in (c)). Arithmetic roughness (Ra) and Kurtosis (K_u) were measured and compared for both samples. (b) and (d) present 2D and 3D SEM images of (a) and (c) respectively after laser irradiation. The crucial role of initial type of roughness is observed by comparing the nanostructures concentration in the SEM.

In contrast, sample 2 was electropolished using an electrolyte formulated for polishing Ni at 25 Volts for 60 seconds. The surface has an arithmetic roughness of Ra = 4.4 nm (< Ra_{th} = 5 nm) and a K_u value of 2.84, making it a bumpy surface.

The change in nanobumps concentration is clearly visible when comparing the SEM images of Figures 3.10(b,d). The spiky surface of sample 1 has a greater surface absorbance than the bumpy surface of sample 2, which increases nanostructure concentration. The initial roughness type is critical in determining surface absorbance and reflectance. Furthermore, AFM characterizations reveal a variation in the height of the produced nanostructures in the two samples. The highest nanobumps height in sample 1 was 89 nm, whereas it was only 22.3 nm in sample 2. Thus, in addition to laser settings, the initial surface type

of roughness plays an important role in regulating surface topography at the nanoscale.

3.3 Surface topography control by time-delay and laser fluence

As presented previously, femtosecond laser irradiations are performed by controlling several influential parameters. In this section, we are focusing on the role and interplay between the laser fluence and time delay for creating different types of nanostructures. Other substantial parameters have been presented previously such as the polarization angle between the two delayed pulses, number of pulses, pulse duration and initial surface roughness. Based on previous experiments, the chosen number of double-pulses sequences (N_{DPS}) was 25 pulses. A cross-polarized ultrashort double pulses is applied in order to break the surface isotropy, avoiding the formation of LIPSS. The relative polarization of the two pulses was fixed by an angle of 90°. The chosen pulse duration was 150 fs and the initial arithmetical mean roughness (R_a) was below 5 nm.

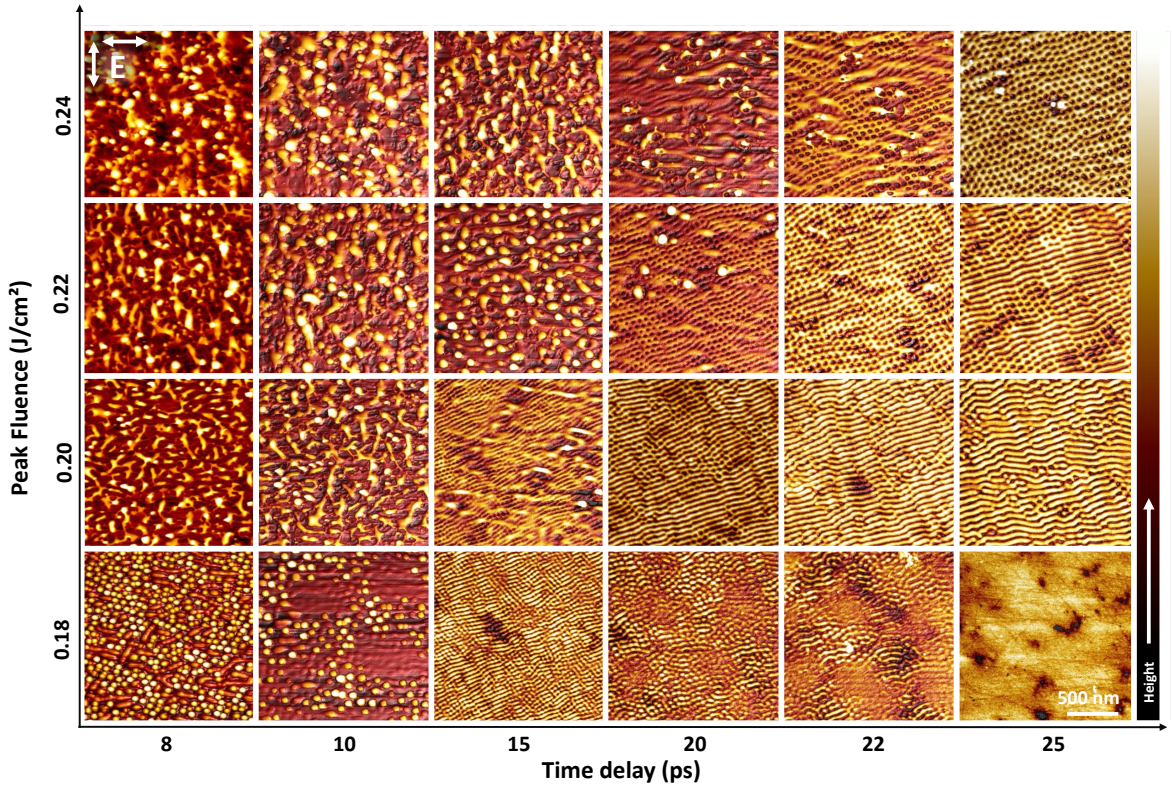

Figure 3.11: 2D AFM images of laser-induced nanopatterns formation on Ni(001) as a function of time delay and peak fluence at a fixed N_{DPS} of 25. The different zones of interest are nanopeaks, nanobumps, nanohumps and nanocavities. They are created progressively at different doses: (0.18 J/cm²; 8 ps), (0.18 J/cm²; 10 ps), (0.18 J/cm²; 15 ps), (0.24 J/cm²; 25 ps). The laser polarization E is indicated by the white arrow.

Figure 3.11 presents 2D AFM images of laser-induced nanopatterns formation by controlling the laser peak fluence from 0.18 J/cm² to 0.24 J/cm² and the time delay (Δt) from 8 ps to 25 ps. Laser parameters are chosen to be below LIPSS formation threshold, which requires a combined action of the double pulses. At low Δt (8 ps and 10 ps) and at a peak fluence above 0.20 J/cm², chaotic nanostructures were observed. They are also observed at (15 ps ; 0.24 J/cm²) and they are formed for a small time-delay between pulses. Energetically, it is somehow acting similarly to a single pulse process, at a cumulated absorbed fluence higher than the single-pulse absorbed threshold since the small delay leads to a slight decrease of Ni reflectivity with electronic thermal excitation before the second pulse [37]. At 0.18 J/cm^2, three different types of nanopatterns were observed at 8 ps, 10 ps and 15 ps. The tallest nanostructures were at Δt = 8 ps and has a shape comparable to a karst peak, so they are named as "nanopeaks". Nanostructures shape has changed at larger time delay of 10 ps. Their diameter has increased and their shape was similar to a bump, so they are named as "nanobumps". At Δt = 15 ps, nanostructures height was extensively decreased and they are named as "nanohumps". Nanostructures progressively disappeared while increasing the time delay from 15 ps to 25 ps. In this case, the cumulated energy was so small and the polarization memory was erased by thermal dissipation before the second pulse arrived. At 0.20 and 0.22 J/cm², we can observe the transition from chaotic structures to stripes, passing by a transition regime at (0.20 J/cm² ; 15 ps and 0.22 J/cm² ; 20 ps). This transition region has a short range order, which consists of locally nanobumps and chaotic nanostructures. However, at Δt = 25 ps, a labyrinthine pattern is observed [1], which are disordered spatial structures that show a short-range order. At 0.24 J/cm², we can observe the switch from disordered nanostructures to a pattern of nanocavities when Δt increases, passing by transition regime from 15 to 20 ps. The hexagonal array of nanocavities was observed previously at similar parameters [21].

3.3.1 Wide variety of nanostructure regimes

Figure 3.12(a-c) present 3D AFM images of the principal nanostructures, which correspond to the laser parameters of Figure 3.11 [a(0.18 J/cm²; 8 ps), b(0.18 J/cm²; 10 ps), c(0.18 J/cm²; 15 ps) and d(0.24 J/cm²; 25 ps)]. Figure 3.12(e) presents the maximum nanostructures height as a function of time delay and laser fluence. The maximum height was characterized on AFM for each parameter. It was classified into two different categories. One category of nanostructures with a maximum height of almost 110 nm presented in (a) and (b), marked by black and green circles respectively. The other category has a maximum height of almost 20 nm presented in (c) and (d), marked by blue and orange circles respectively. The material surface exhibits a significant swelling suggesting a frustrated ablation regime [86, 87].

It can be observed that (a) and (b) have respectively the shape of nanopeaks and nanobumps but with different width, organization and concentration. However, (c) and (d) present a hexagonal network of self-organized nanohumps and nanocavities on the surface. Interestingly, (c) exhibits a state with persistent dynamics with oriented stripes independent from the local polarization that may corresponds to "spiral defect chaos" [88].

The transition regimes between the two different nanostructures categories of (110 nm and 20 nm) are shown in an almost diagonal way in Figure 3.11 and Figure 3.12(e). It can be

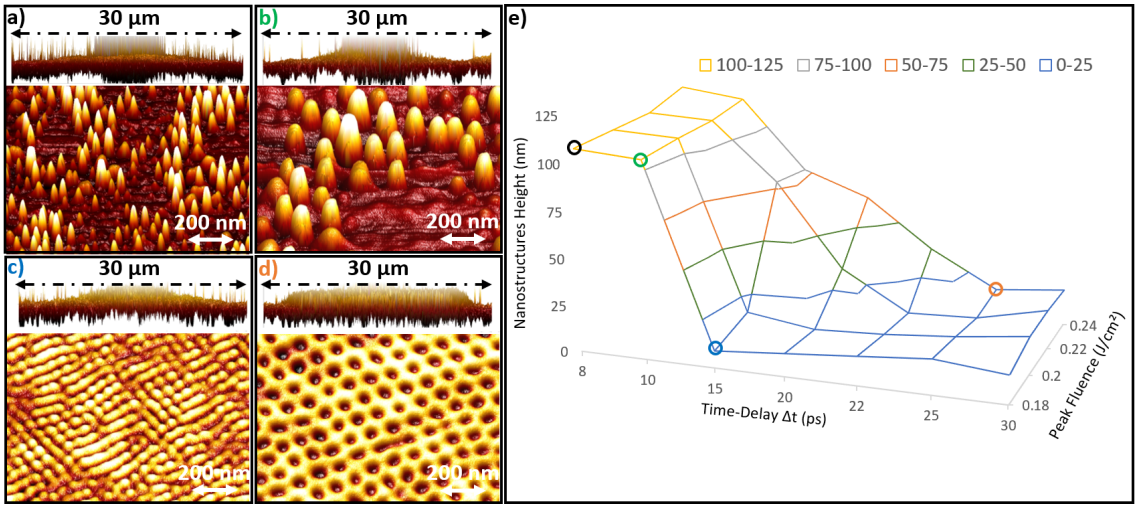

Figure 3.12: (a-d) presents the 3D AFM images of the laser spot topography in the spallation regime and the principal nanostructures types (nanopeaks, nanobumps, nanohumps and nanocavities). (e) Maximum nanostructures height as a function of time delay and laser fluence. The colored circles in (e) (black, green, blue and orange) present respectively the regions of (a, b, c and d) nanostructures.

understood that the lost energy by increasing the time delay was covered by the intensification of laser fluence to maintain the instability of the critical phase leading to the presence of these nanostructures. The laser spots images (a, b and c) confirm the occurrence of a spallation regime which exists above the melting threshold, while remaining below phase explosion threshold.

3.3.2 Wide variety of nanopatterns morphologies

Figure 3.13 presents the 3D AFM images of the principal nanopatterns (a-d) at different scanning scales. (a) presents a nanobumps shape comparable to a karst peaks. It has a width of ≈20 nm and a height of ≈100 nm and named as nanopeaks. At the same laser peak fluence of 0.18 J/cm², and just by increasing the time delay from 8 ps to 10 ps, the nanostructures have transformed from (a) to (b). In (b), it has a shape of nanobumps but totally different from that in (a). The diameter of the bump is ≈60 nm and the height is ≈100 nm. Moreover, by a slight increase of the time delay from 10 to 15 ps, the nanobumps scale was reduced to reach a height less than 10 nm in figure 3.13(c), which are named nanohumps. Those small hexagonal nanohumps have a periodicity of ≈50 nm. On the other hand, (d) presents a self-arranged hexagonal array of nanocavities with a periodicity of ≈85 nm and a depth of ≈25 nm.

In addition, the laser spot diameter for the nanopatterns (a, b and c) was $\leq$ 9 µm. However, the laser spot diameter for the nanocavities shown in (d) was $\leq$ 22 µm. Thus, laser fluence is a critical factor in determining the self-organized regime of nanostructures growth.

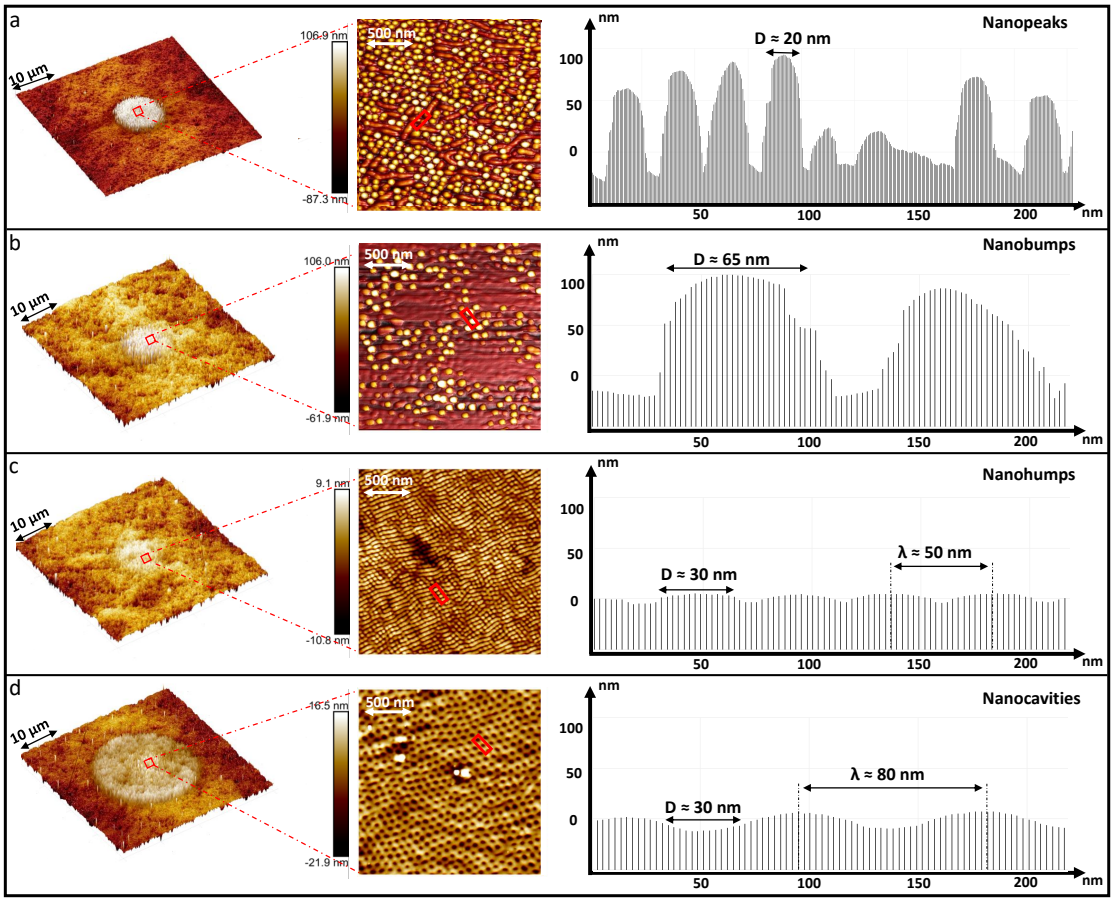

Figure 3.13: 3D AFM images of the principal nanopatterns (a-d) at different scales, presenting the laser spot region. A scan profile was performed for each type of the principal nanostructures presenting the shape and the periodicity of each type.

3.4 Conclusion

Various nanopatterns corresponding to distinct self-organization regimes induced by convection mechanism at the nanoscale were investigated on femtosecond laser-irradiated nickel surfaces. Forming far from equilibrium, complex patterns of structures are revealed caused by an intensive light energy exchange with a dissipative environment. The nanorelief is characterized by mounds and depressions where the unbalance and the respective predominance is shown to be tunable by the time-delay and the fluence. Observed for (0.18 J/cm^2; $\Delta t = 15$ ps) and (0.24 J/cm^2; $\Delta t = 25$ ps) both kind of nanostructures have 30 nm diameter and tens of nanometers height. Also, nanopeaks and nanobumps were observed at (0.18 J/cm^2; $\Delta t = 8$ ps) and (0.18 J/cm^2; $\Delta t = 10$ ps). The nanopeaks have 20 nm width and 110 nm height whereas the nanobumps exhibit a 65 nm width and 100 nm height. Successively implying emergence, growth, amplification and regulation of the pattern formation, laser parameters as peak fluence, time delay, and number of double-pulses sequences play a significant role on modifying surface morphology and topography. Furthermore, the initial surface roughness and type of roughness is another essential feature to be controlled

to switch from a regime of self-organization to an other one. The involved instabilities being expected in most of ultrafast-laser irradiated materials, the process reported in this manuscript is *a priori* generalizable to any metals in order to design a predefined surface morphology at the nanoscale. These results and related discussions have been published in Nanomaterials and Applied Physics A journals [22, 89].

Chapter 4

Formation of high-aspect ratio nanopeaks

We grow in direct proportion to the amount of chaos we can sustain and dissipate

– Ilya Prigogine, Order Out of Chaos: Man's New Dialogue with Nature "Recommended by J-P Colombier"

The capacity to synthesize and design highly intricated nanoscale objects of different sizes, surfaces and shapes dramatically conditions the development of multifunctional nanomaterials. Ultrafast laser technology holds great promise as a contactless process able to rationally and rapidly manufacture complex nanostructures bringing innovative surface functions. The most critical challenge in controlling the growth of laser-induced structures with sizes below the light diffraction limit is the absence of external order associated to the inherent local interaction due to the self-organizing nature of the phenomenon. In this chapter, we report high aspect-ratio nanopatterns driven by near-field surface coupling and architectured by timely-controlled polarization pulse shaping. The obtained high aspect-ratio surface nanotopography is expected to prevent bacterial proliferation, and have great potential for catalysis, vacuum to deep UV photonics and sensing.

4.1 Introduction

Structuring on extreme scales is experiencing revolutionary rapid progress thanks to the emergence of ultrafast laser sources exploiting energy confinement and near-field optical coupling. This chapter reveals the uniform formation of unconventional self-organized patterns on the 100 nm scale generated by focused ultrafast light. Irradiated surface turns to a forest of nanopeaks with the highest aspect ratio reported in the literature at the nanoscale (height 100 nm: width 20 nm with a sub-100 nm periodicity). Laser beam polarization is timely controlled to prevent anisotropic energy absorption and to synchronize the laser energy delivery rate with the material dynamic response. This strategy upgrades the energy coupling and the structure growth explained by a state-of-the-art Maxwell-hydrodynamic simulation. Initiated by convective instabilities at the nanoscale, it was demonstrated that the crossed pulses polarization cancels the individual response of each nanorelief due to near-field optical enhancement and enables a collective response of the dissipative structure. The uniformity of the patterns results finally from the regulation between growth and local ablation process.

The exploited nanostructuring strategy, relying on a timely-controlled polarization feedback, paves the way for the production of homogeneous high-aspect ratio structures for nanoengineering metamaterials. Nanostructuring of high aspect ratio regular and densely packed nanostructures, open up new avenues for improving bactericidal properties and high adhesive forces, antiphase and polarization state manipulation, localized surface plasmon resonance excitation, and extreme light confinement at the nanoscale, significantly improving surface nonlinear optical response. This chapter finally demonstrates that ultrafast laser process provides unrivaled control for creating suitable artificial media with nanofeatures that outperform those of naturally occurring surfaces, with promised novel applications.

4.2 Surface nanoengineering by polarization strategy

A (001) surface-oriented nickel surface was photoexcited by 100 fs laser pulses at the central wavelength of 800 nm controlling laser peak fluence, number of double-pulses sequences

(N_{DPS}) and polarization angle of single and double laser pulses. In the focal region, the laser-induced nanopatterns exhibit remarkable topographical complexity and consistency depending on the beam features as revealed by scanning electron microscopy (SEM) and atomic force microscopy (AFM) and shown in this section by using three different polarization strategies.

4.2.1 Single pulse, linear polarization

Uniform micro-spikes are usually obtained using a linearly polarized field near the ablation threshold at the micrometer scale with a high number of pulses to enhance positive feedback [90], while nonuniform nanospikes are obtained with a few numbers of pulses at high fluence to prevent LIPSS [91]. These two approaches do not allow to produce homogeneous spiky structures at the nanoscale. To provide a benchmark to compare the nanostructure features, linear polarization irradiations were performed for 1 and 2 pulses at a peak laser fluence between 0.2 J/cm^2 and 3 J/cm^2. A low value of N were operated to prevent LIPSS formation as presented in table 4.1.

Wavelength	Repetition rate	Polarization	Pulse duration	Laser fluence	N
800 nm	1 kHz	Linear	100 fs	0.2 - 3 J/cm^2	1 - 2

Table 4.1: Main irradiation parameters for single pulse sequences, linear polarization

Figure 4.1 presents the SEM and pseudo-3D images of irradiated Ni(001) surface, by single pulse with linear polarization induced by bursts of ultrafast laser at N = 1 & 2. For 1 pulse, at low fluence $\leq$ 0.5 J/cm^2, no structures were observed. At 0.6 J/cm^2, small spiky structures were obtained and marked in the red region in Figure 4.1(b). These structures disappeared when increasing the laser fluence to $\geq$ 1 J/cm^2, corresponding to the ablation regime for N = 1.

By increasing the N to 2 pulses, different topographies were observed as presented in Figure 4.1(d). For a low laser fluence $\leq$ 0.3 J/cm^2, we were below nanostructures formation threshold. However, at 0.4 J/cm^2, circular structures appeared on the surface surrounded by small spikes. The pseudo-3D image here present a low aspect ratio of these structures. By increasing the fluence to 0.5 J/cm^2, different topography was observed. The formation of spiky nanostructures were reported as presented in the green region. Here, additional investigations are essential to figure out if they are similar in aspect-ratio and concentration compared to the nanopeaks observed in Chapter 3.

Therefore, additional characterizations on AFM are performed to understand the height and shape of the newly observed peaks. As presented in Figure 4.1(b), the optimal pattern of nanostructures were obtained for a single state of polarization at a laser peak fluence of 0.5 J/cm^2. As presented in the SEM image of Figure 4.2(a), the 2D FT does not display any particular symmetry of these unorganized nanostructures. Although chaotic, a maximal nanostructures height of 55 nm has been estimated by the AFM analysis as shown in Figure 4.2(b-c).

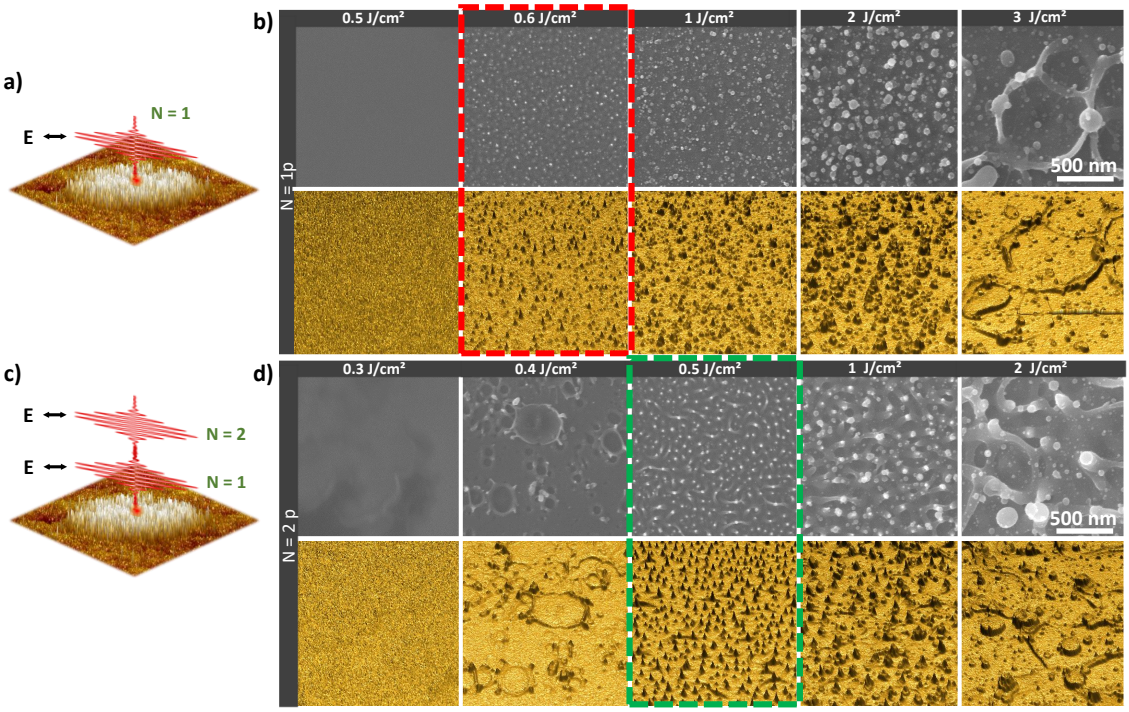

Figure 4.1: a & c) Schematic illustrations of experimental single pulse with linear polarization induced by bursts of ultrafast laser at N = 1 & 2 accordingly. b) Scanning electron microscopy and pseudo-3D images of irradiated surface at an incident laser fluence range of 0.5 - 3 J/cm^2 with 1 pulse. d) Scanning electron microscopy and pseudo-3D images of irradiated surface at an incident laser fluence range of 0.3 - 2 J/cm^2 with 2 pulses. The red and green regions show the potential for peaks formation.

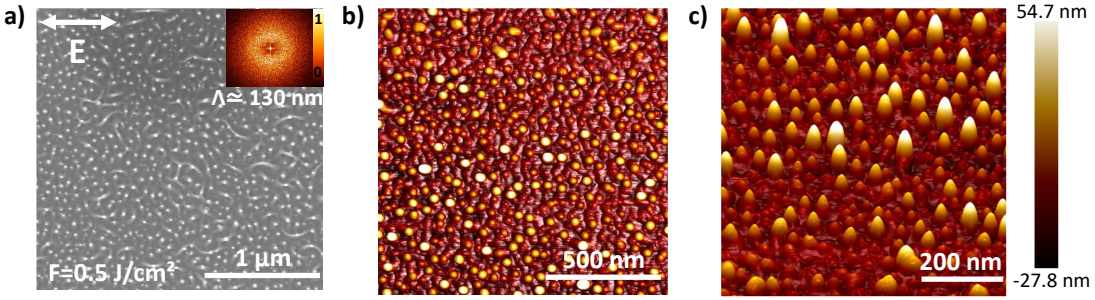

Figure 4.2: SEM Characterization of irradiated surface at an incident laser fluence of 0.5 J/cm^2 with 2 pulses by scanning electron microscopy with 2D Fourier Transform (a), 2D atomic force microscopy (b), and 3D atomic force microscopy (c). The laser polarization E is indicated by the white arrow.

4.2.2 Single pulse, circular polarization

Driven by near-field light enhancement on local surface nanoreliefs, organized patterns were recently discovered with an ultimate scale down to tens of nanometers such as nanopeaks, nanobumps, nanohumps and nanocavities at $N = 25$ [22, 83]. In order to avoid the formation of LIPSS, circular polarized pulses were applied to break the surface isotropy by controlling the laser peak fluence. The formation of analogous nanostructures was reported by using circular polarization on tungsten metal [92]. Consequently, Ni(001) surface irradiation has been performed with a circular polarization at a fixed $N = 25$ and a laser fluence between 0.1 J/cm^2 and 0.24 J/cm^2 as presented in table 4.2.

Wavelength	Repetition rate	Polarization	Pulse duration	Laser fluence	N
800 nm	1 kHz	Circular	100 fs	0.15 - 0.24 J/cm^2	25

Table 4.2: Main irradiation parameters for single pulse sequences, circular polarization

Figure 4.3 presents the SEM images of irradiated surface at an incident laser fluence range of 0.15 - 0.24 J/cm^2. At 0.15 J/cm^2 $\leq F \leq$ 0.16 J/cm^2, barely nanostructures are observed, their shape is comparable to ripples. However, HSFL are observed at 0.18 J/cm^2 as presented in the green region in Figure 4.3(b), which is the same laser fluence of nanopeaks formation in Figure 3.11 but with different polarization strategy. Moreover, while increasing the laser fluence $\leq$ 0.20 J/cm^2, chaotic structures appeared on the surface.

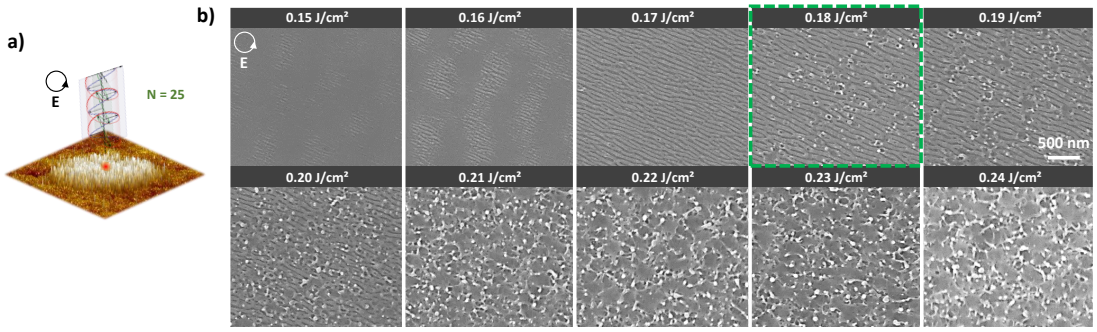

Figure 4.3: a) Schematic illustrations of experimental single pulse with circular polarization induced by bursts of ultrafast laser at $N = 25$. b) Scanning electron microscopy of irradiated surface at an incident laser fluence range of 0.15 - 0.24 J/cm^2. The green region presents the same laser fluence of nanopeaks generation by cross polarized double pulses.

Thus, nanopeaks nanostructures have not been observed using circular polarization, high spatial frequency LIPSS (HSFL) patterns are observed at 0.18 J/cm^2. Their periodicity $\Lambda \approx 75$ nm was measured on SEM micrograph and confirmed with the 2D FT. The observed HSFL have a diagonal direction of $\approx 45°$ as shown in Figure 4.4(a). Their height has been estimated by 2D and 3D AFM analysis of $\approx$ 30 nm as presented in Figure 4.4(b-c), which are identical to the observed ones on Cr [18].

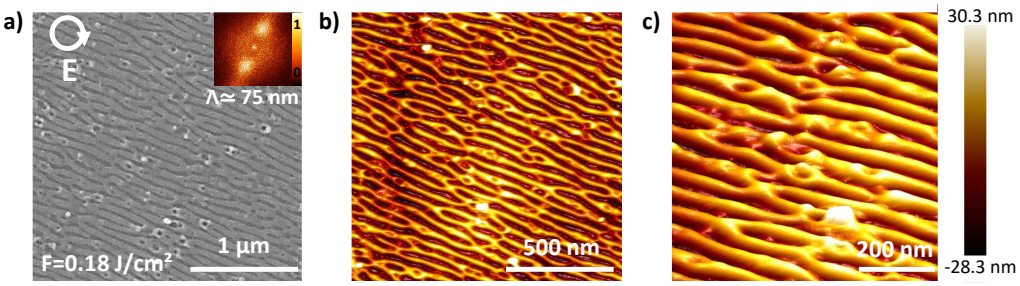

Figure 4.4: SEM Characterization of irradiated surface at an incident laser fluence of 0.18 J/cm^2 with 25 pulses by scanning electron microscopy with 2D Fourier Transform (a), 2D atomic force microscopy (b), and 3D atomic force microscopy (c). The laser polarization E is indicated by the white arrow.

4.2.3 Double pulse, orthogonal polarization

Spontaneous and well organized nanostructures, named as nanopeaks [22] are discovered at a specific laser fluence of 0.18 J/cm^2, a time delay of 8 ps and at N_{DPS} = 25 as presented in table 4.3 and the schematic illustration in Figure 4.5(a).

Wavelength	Repetition rate	Polarization	Pulse duration	Laser fluence	N_{DPS}
800 nm	1 kHz	Perpendicular	100 fs	0.18 J/cm^2	25

Table 4.3: Main irradiation parameters for double pulse, orthogonal polarization

The performed 2D FT displays a diagonal symmetry of the observed nanostructures with a periodicity $\Lambda \approx 70$ nm as observed in Figure 4.5(b). The revealed nanopeaks have a high concentration, good organisation and large maximal height of ≈ 92 nm as observed in the 2D and 3D AFM images in Figure 4.5(c) and Figure 4.5(d). Thus, this demonstrates that double pulse cross-polarization is a remarkably efficient strategy to boost the formation of high aspect ratio nanopeaks, able to functionalize uniformly the surface.

4.3 Formation of high-aspect ratio nanopeaks

The top-view of the central area at N_{DPS} = 25 is shown in the SEM image as presented in Figure 4.6(a). A series of transmission scanning electron microscopy images from the highlighted lamellas in Figure 4.6(a) are presented in Figure 4.6(c-d), displaying surface filled of boosted spontaneous nanopeaks with a diameter of $\approx$ 20 nm and elevation of $\approx$ 100 nm. Tilted SEM image of the irradiated zone is presented in Figure 4.6(b) showing a forest of nanopeaks. Nanopeaks periodicity in the STEM images confirms the periodicity calculated by the 2D FT in Figure 4.11 which is ≈ 70 nm.

The layering of crystals with initial orientation and laser-induced disorientions at the top of the peaks as presented in Figure 4.7(c-e) may result from very high cooling rates of up

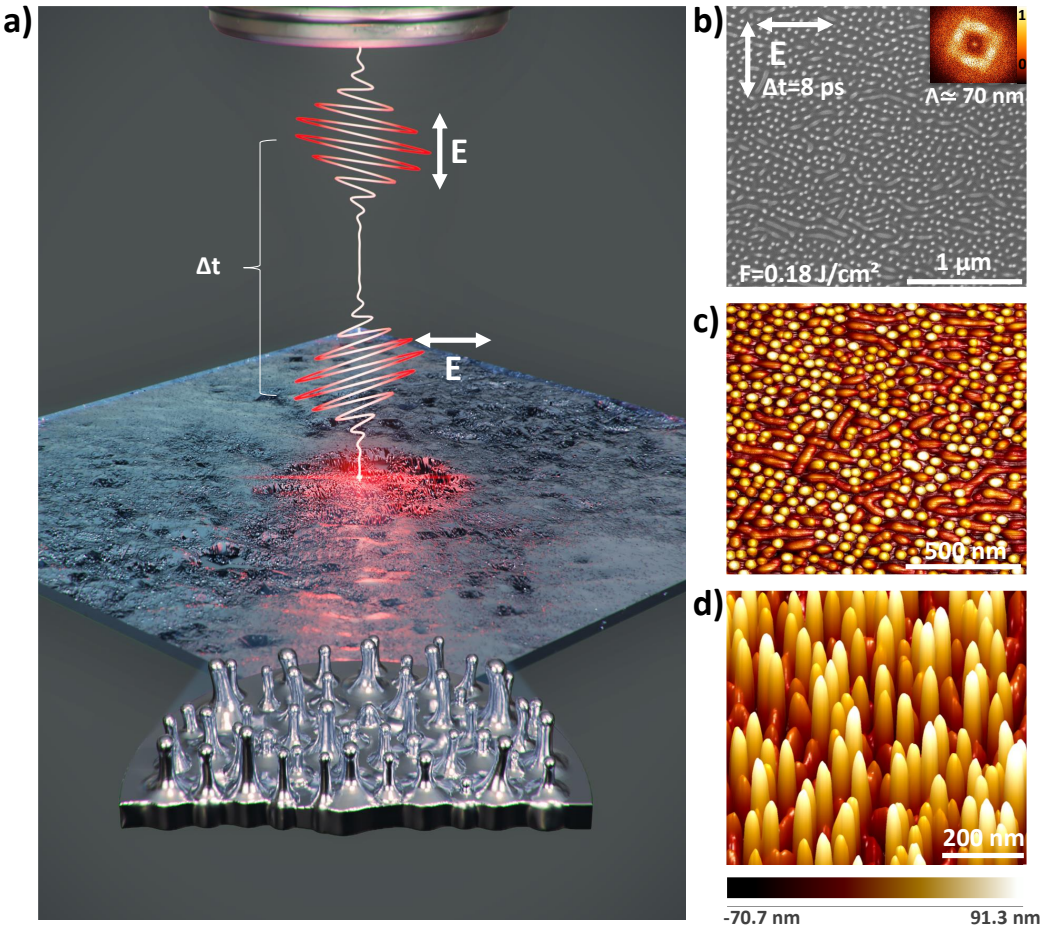

Figure 4.5: a) Schematic illustration of nanopeaks formation by femtosecond laser double pulse. b) Scanning electron microscopy with 2D Fourier Transform (FT). c) 2D atomic force microscopy. d) 3D atomic force microscopy of various surface morphologies irradiated at an incident laser fluence of 0.18 J/cm^2 with 25 pulses. The laser polarization E is indicated by the white arrow.

to 10^{12} K/s, bringing the molten structure to a state of strong undercooling below the equilibrium melting temperature [93]. The structural transformations could be created either by crystal twinning [60], stress-induced dislocations [94] or by inhomogeneous epitaxial regrowth [93].

Electron energy loss spectroscopy (EELS) entails the probing of core and valence level excitations caused by the laser absorption, where electrons are collected based on their energy after interacting with the specimen. This reveals electronic structure and bonding information at very high spatial resolutions down to single-atom levels. We have exploited EELS to investigate the extent of ultrafast laser-induced chemical modifications, in particular the uneven catalytic properties of hot nickel with oxygen due to inhomogeneous temperature resulting from non-uniform topography as presented in Figure 4.8.

STEM-ADF image of a single nanopeak, acquired simultaneously with electron energy loss spectroscopy (EELS) spectral data in a spectrum image, is presented in Figure 4.8. O

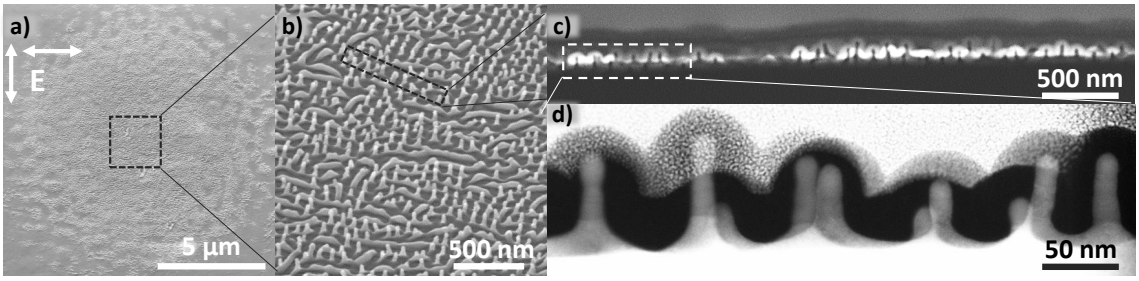

Figure 4.6: a) Scanning electron microscopy of a Ni(001) crystal irradiated by 25 double pulses at an incident laser fluence of 0.18 J/cm^2 and a time delay of 8 ps between the two crossed polarizations. b) Tilted SEM image of the irradiated zone in (a), presenting a forest of high-aspect ratio nanostructures. c-d) A series of scanning transmission electron microscopy (STEM) images from the highlighted lamella in (a), extracted by a site specific method using a focused ion beam. These cross-sectional views present the formation of nanopeaks and confirm their periodicity and their unique aspect ratio on a large surface.

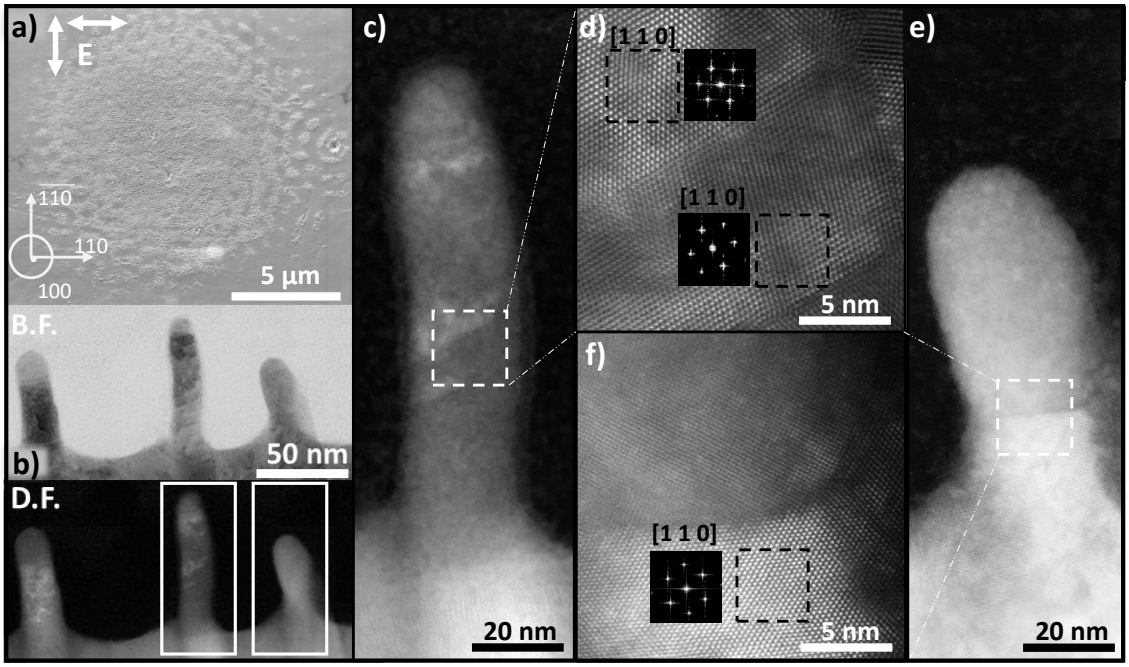

Figure 4.7: a) Scanning electron microscopy of a Ni(001) crystal irradiated by 25 double pulses at an incident laser fluence of 0.18 J/cm^2 and a time delay of 8 ps between the two crossed polarizations. Crystallographic axes are indicated. b-f) HR-STEM images of the nanopeaks area in, presenting the oriented and disoriented crystals of the formed nanopeaks. The presented Ni(110) orientation of the cross sectional plane corresponds to the initial Ni(001) orientation of the top plane.

K-edge and Ni L3-edge are presented in the green and red charts, for an energy losses of $\approx$ 535 eV and $\approx$ 855 eV, respectively. In the STEM-ADF image, a very small oxide layer is

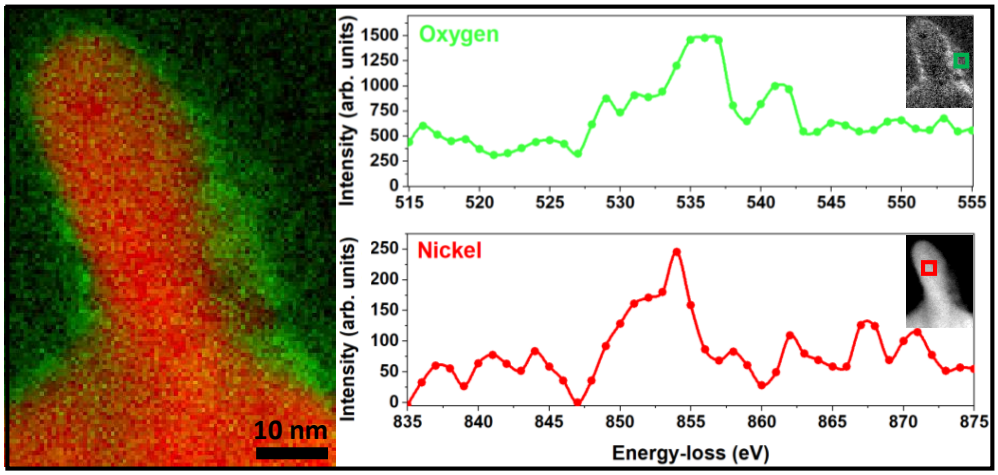

Figure 4.8: STEM-ADF image of a single nanopeak, acquired simultaneously with electron energy loss spectroscopy (EELS) spectral data in a spectrum image. O K-edge and Ni L3-edge are presented in the green and red charts.

observed (in green) on the top surface of nanopeaks (in red). This layer thickness does not exceed ≈ 7 nm. As a result, surface oxidation may not have played a significant role in the formation of nanopeaks.

4.4 Multipulse dynamics of nanopeaks generation

The nanopeaks revealed in Figure 4.5 might have an extraordinary potential in the application field. Understanding the physical mechanisms leading to the creation of these nanostructures is vital. Mechanisms comprehension has a key role in promoting the manufacturing process and enhancing the control of nanopeaks shape and concentration, which will certainly make them compatible and adaptable for different function. As a result, a pulse-to-pulse growth dynamics investigation has been carried out by setting laser peak fluence to 0.18 J/cm^2, time delay to 8 ps and pulse duration to 70 fs, varying the N_{DPS} from 10 to 50 as presented in Figure 4.9 and 4.10. The impacts are independent as performed on a different surface location at a fixed number of pulses value. They were observed ex-situ to progressively unveil the activation, triggering and development of nanopeaks.

A pseudo 3D reconstruction of the SEM images was performed for Figure 4.9, visibly presenting the transitions from a smooth initial surface to the formation of crests, nanopeaks, nanostripes and chaos for different N_{DPS}. The AFM images displays the nanopeaks formation at a higher magnitude, covering the missing height information of the 3D reconstructed SEM images, and presenting the formation of convection cells [72], crests and nanopeaks for different N_{DPS} as shown in Figure 4.10(a). To summarize, the nanopeaks counts per μm^2 vs. N_{DPS} chart displays the nanopeaks generation and concentration for different N_{DPS} as presented in Figure 4.10(b).

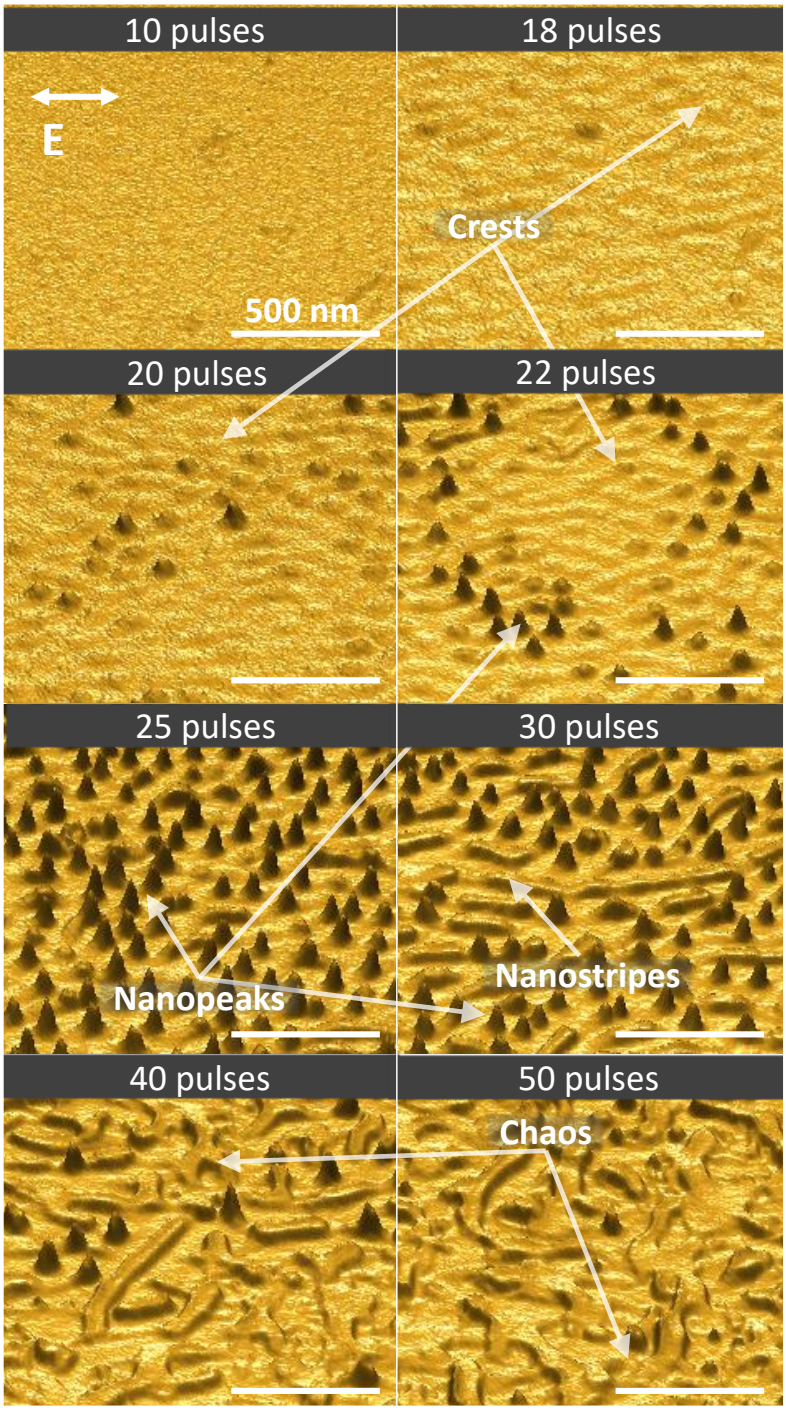

Figure 4.9: Pseudo-3D scanning electron microscopy of the irradiated surface by different pulses between 10 and 50 pulses at an incident laser fluence of 0.18 J/cm^2 and a time delay of 8 ps between both laser crossed polarizations. The pulse-to-pulse dynamics present the nanopeaks formation by displaying the transformations from ridges to nanopeaks, nanostripes and chaos.

At $N_{DPS} < 10$, the irradiated surface topography looks identical to the initial surface topography before laser irradiation. Differently, at $10 \leq N_{DPS} \leq 14$, convection cells ap-

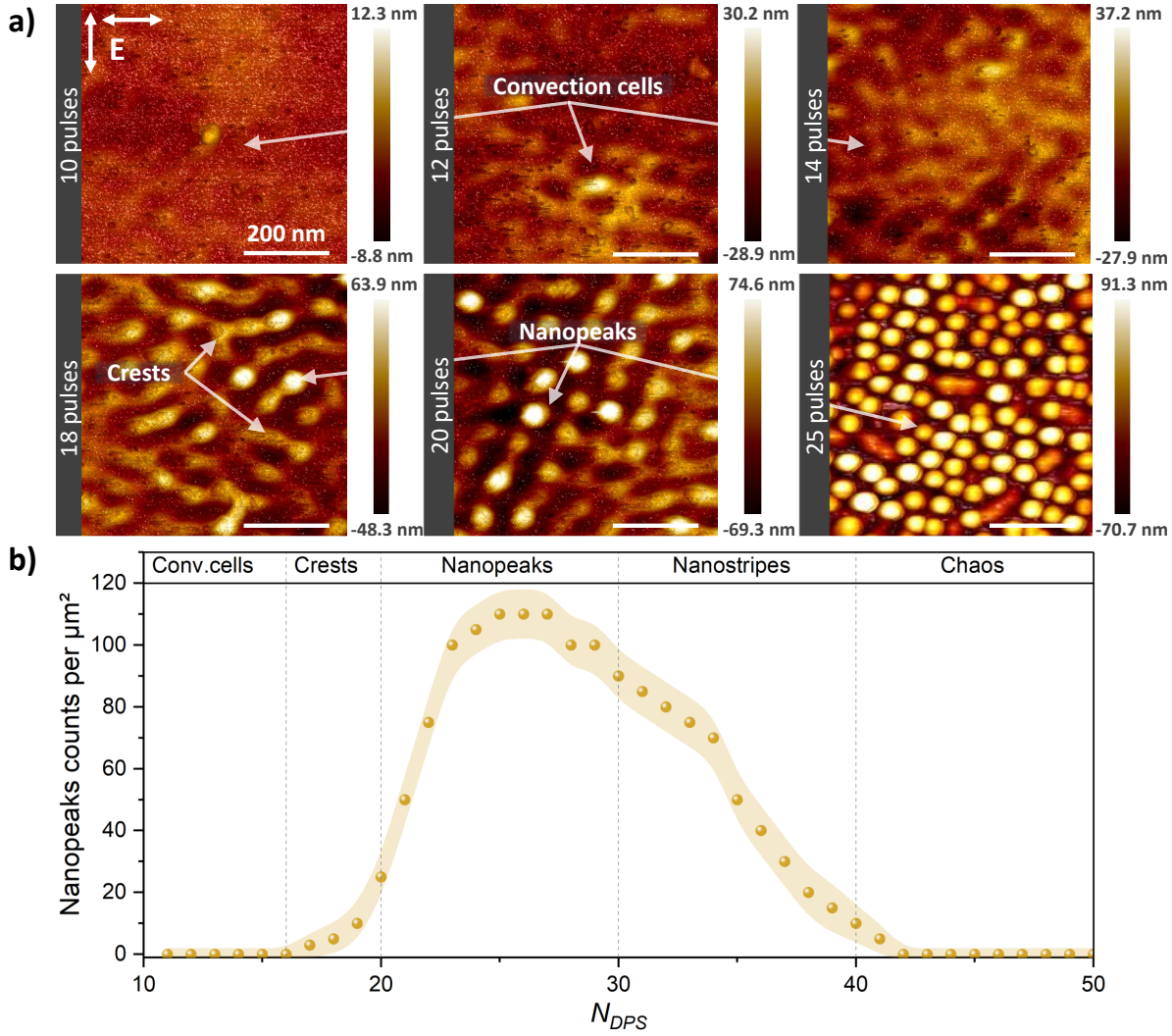

Figure 4.10: 2D atomic force microscopy of the laser irradiated surface by different pulses between 10 and 25 pulses at an incident laser fluence of 0.18 J/cm^2 and a time delay of 8 ps between both laser crossed polarizations. The pulse-to-pulse dynamics of the nanopeaks formation by displaying the transformations from convection cells to ridges and nanopeaks. b) Nanopeaks concentration evolution with the increasing N_{DPS} that underlines the role of laser dose to optimally synthesize a specific pattern.

pear on the surface with a diameter of $\simeq$ 70 nm and a maximum height of $\simeq$ 37 nm at 14 pulses as presented in Figure 4.10(a). Afterwards, the crests started to form on the convection cells at $18 \leq N_{DPS} \leq 20$. Subsequently, at $20 \leq N_{DPS} \leq 30$, the nanopeaks started to appear and grow from a height of $\simeq$ 64 nm to reach a maximum height of $\simeq$ 92 nm at N_{DPS} = 25. For this dose regime, the nanopeaks concentration reaches its optimal condition with a maximum counts of 110 per μm^2. The nanopeaks concentration decreases progressively while increasing the $N_{DPS} > 28$ and the nanopeaks are replaced by nanostripes at $30 \leq N_{DPS} \leq 40$. Chaotic nanostructures started to appear on the surface. Eventually, they are formed for higher N_{DPS}.

4.5 Nanopeaks aspect-ratio and distribution control

Controlling nanopeaks aspect ratio and concentrations will definitely make them compatible with several types of applications. The essential role of laser parameters in regulating nanopeaks shape and concentration for a constant laser peak fluence of 0.18 J/cm^2, a time delay of 8 ps and a N_{DPS} of 25 as presented in Figure 4.11 and 4.12, by varying the pulse duration between 70 fs and 500 fs progressively. The nanopeaks periodicity has slightly increased from 70 nm to 80 nm while increasing the pulse duration from to 70 fs to 500 fs as presented by the 2D FT of the Figure 4.11 . The nanostructures concentration was extracted from the SEM image and synthetized in the presented chart. The concentration has decreased from 14 % to 6.5 % while increasing the laser pulse duration from 70 fs to 500 fs accordingly, in agreement with the increase in the period of the 2D FT interpretation.

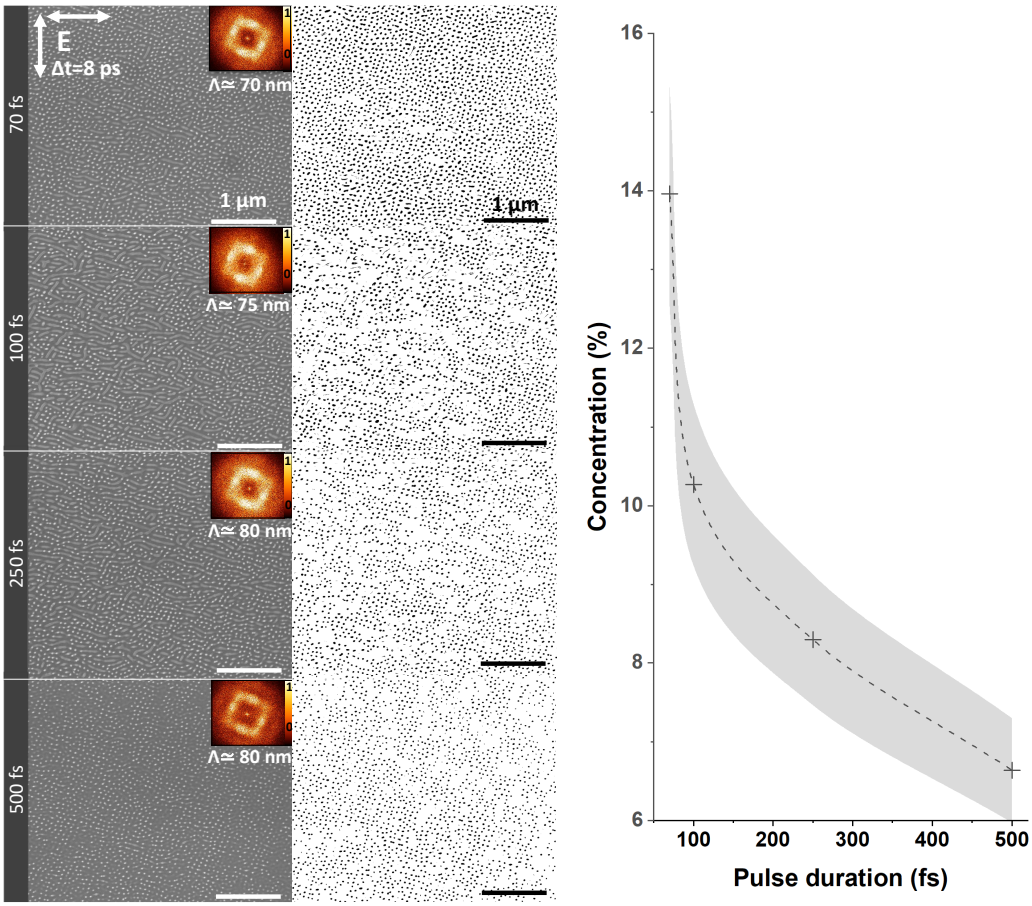

Figure 4.11: Scanning electron microscopy with 2D FT and concentration interpretation of scanning electron microscopy after irradiation by 25 double pulses at an incident laser fluence of 0.18 J/cm^2, time delay of 8 ps between the two crossed polarizations and pulse duration between 70 fs and 500 fs. The chart presents the crucial role of pulse duration in controlling the concentration of the formed nanopeaks.

The nanopeaks height was determined by an AFM analysis presented in Figure 4.12

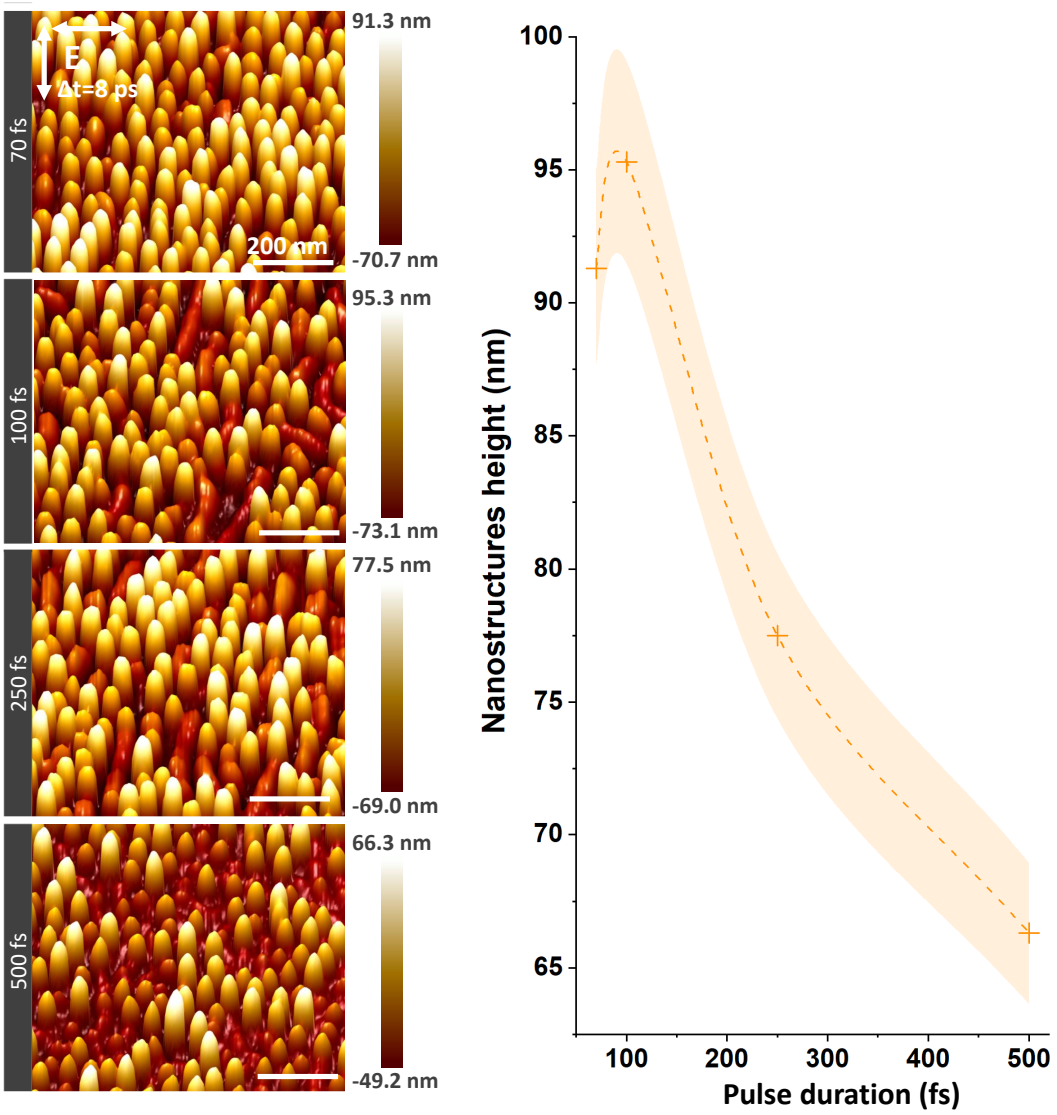

Figure 4.12: 3D atomic force microscopy images of the irradiated surface by 25 double pulses at an incident laser fluence of 0.18 J/cm^2, time delay of 8 ps between the two crossed polarizations and pulse duration between 70 fs and 500 fs. The chart presents the crucial role of pulse duration in controlling the height of the formed nanopeaks.

and averaged for each condition in the presented chart. Nanopeaks height has decreased of about 30% from a maximum height of 95 nm at 100 fs to 66 nm at 500 fs. This suggests that the mechanical momentum defined by pulse duration plays a crucial role in controlling the aspect ratio, the periodicity as well as the concentration of the formed nanopeaks.

4.6 Conclusion

We conclude by pointing out the proposed nanostructuring strategy, relying on a timely-controlled polarization feedback, opens the route for producing uniform high-aspect ra-

tio structures for nanoengineering metamaterials. A flat surface turns into a forest of nanopeaks with a remarkably high aspect-ratio (5:1) and a sub-100 nm periodicity. This nanopatterning could have a great impact in surface bioengineering as the size, shape and distance of the nanopeaks can prevent virus activation and determine the ability of cells to adhesion, proliferation and differentiation, establishing bactericidal performances [95, 96]. Engineering of high aspect ratio regular and densely packed nanostructures opens also broad optical opportunities towards phase and polarization state manipulation, metaphotonics with plasmonic metastructures and extreme light confinement at the nanoscale, strongly enhancing the surface nonlinear optical response in deep and vacuum UV spectral regions [97, 98]. Ultrafast laser process offers unprecedented control for manufacturing appropriate artificial media with nanofeatures surpassing those of any naturally-occurring surfaces with expected innovative applications in biomedecine, nanocatalysis, and metaphotonics. These results and related discussions have been published in WILEY, Advanced Science journal [34].

Chapter 5

Self-organised nanopatterns via hydrodynamics instability and non-linear dynamics

If everything was easy, success would not be satisfying. Difficulty is where the beauty of the work is appreciated

– Mathilde Claude Prudent

In this chapter, electromagnetic coupled with hydrodynamic simulations were performed to reveal why this unique optical manipulation allows peaks generation by inhomogeneous local absorption sustained by nanoscale convection. Moreover, we used non-linear dynamics and physics-guided machine learning, an emerging field of research that combines physical knowledge and machine learning to predict novel patterns by integrating partial physical knowledge in the form of the Swift-Hohenberg partial equation. The carried work not only advances the general goal of elucidating the complex multi-scale phenomenon of LIPSS formation, but it also opens a new experimental path to generate unconventional structures with extreme periodicities on different materials, opening up new possibilities for ultrafast laser processing functionalization of metals.

5.1 Introduction

Several nanopatterns representing unique self-organization regimes were studied by a femtosecond laser on nickel surfaces. An intense light energy exchange with a dissipative environment results in intricated 2D patterns of structures forming far from equilibrium. In the previous chapters, we demonstrated that a modest change in the amount and timeframe of energy delivery perturbs the system, leading to a transition from one stable self-organization regime to one with new features. The self-formation of nanobreath-figure, nanocrosshatch, nanopeaks, nanohumps, nanobumps, nanocavities and nanolabyrinthine patterns are reported. Irradiation conditions defined by peak fluence, time-delay, and the number of double-pulse sequences have a key role in selecting competing surface patterns by sequentially fostering emergence, growth, amplification, and regulation of pattern development. The degree of instability of such patterns is so high that the nanostructure shape organization can be altered by a few picoseconds delay change. These states are characteristic of attractors toward which the dynamical system tends to evolve in dissipative structures. The door is open to describe via hydrodynamic instability and nonlinear dynamics the laser-induced surfaces with models able to reproduce the variability of the patterns in the phase space and explore the origin of bifurcations.

5.2 Hydrodynamics

5.2.1 Hydrodynamics instabilities

Self-organization regimes may result from complex flows occurring in the transiently laser-induced molten surface. At the considered fluence below the ablation threshold, a thin liquid layer of 10-20 nm thickness is expected to be formed at the surface few ps after irradiating Ni surface. During the first picosecond, an early thermomechanical excitation of the electrons happens. During the relaxation stage, the confined temperature gradient of femtosecond laser irradiation induces a pressure wave on the top surface which is followed by a rarefaction wave [16]. Consequently, the melt layer is driven toward the free surface by the rarefaction wave in the same direction of temperature gradient as presented in Figure 5.1(a). It is exactly the reverse of destabilizing effect of the gravitational force on a liquid

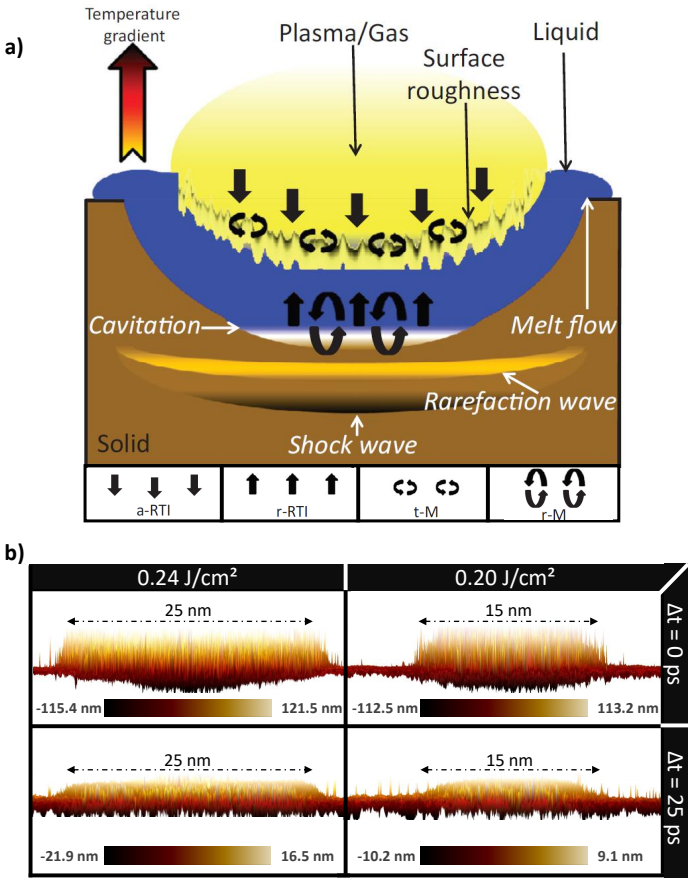

Figure 5.1: a) Ultrashort-laser induced instabilities in a liquid layer: ablative Rayleigh-Taylor instability induced by recoil pressure (a-RTI), Marangoni convection instability (hydrothermal waves) induced by transverse temperature gradients on surface nanoroughness (t-M), Rayleigh-Taylor instability induced by rarefaction wave (r-RTI), Marangoni instability driven by rarefaction (r-M). Straight arrows indicate the direction of fluid flow acceleration, curved arrows show the direction of convection velocities. b) Experimental 3D AFM images of the laser spot topography in the swelling regime presenting the role of laser fluence and time-delay in enhancing the hydrodynamic instabilities.

heated from below [99].

Guided by surface tension and rarefaction forces, hydrothermal flows develop a thermo-convective instability at the nanoscale, similar to well-known Rayleigh-Bénard-Marangoni instabilities. This mechanism represents a convincing scenario for generating hexagonal nanostructures (nanocavities or nanohumps on the surface) [100]. The Rayleigh-Bénard-like instability occurs since there is a density gradient between the top and the bottom surface, rarefaction wave acts trying to pull the cooler, denser liquid from the bottom to the top [101][102]. Therefore, a Bénard-Marangoni convection occurs along the unstable fluids interface, initiated by small flow perturbations due to recurring surface tension gradients. This Marangoni flow transports thermal energy, that can be characterized by the

Marangoni number, comparing the rate at which thermal energy is transported by this flow to the rate at which thermal energy diffuses. Modulated by near field coupling on local roughness, transverse temperature gradients are built parallel to the surface that turns to be unstable [83].

Figure 5.1(b) presents the experimental 3D AFM images of the laser spot topography in the swelling regime, displaying the role of laser fluence and time-delay in controlling the hydrodynamic instabilities. By comparing the laser fluences at fixed time-delay, we can understand that laser fluence plays a crucial role in enhancing and controlling the impact or nanostructured diameter. Since the impact diameter has increased from 15 to 25 nm by increasing the laser fluence from 0.20 to 0.24 J/cm² at fixed time-delays of 0 or 25 ps. Thus, we can assume that higher laser fluence in the swelling regime may enhance the cavitation diameter which can increase the surface of the liquid flow. Moreover, time-delay has also a significant role in enhancing the shock wave and rarefaction wave. By comparing the nanostructures height at a fixed laser fluence of 0.20 or 0.24 J/cm², we can observe that at $\Delta t = 0$, the nanostructures height are 5 to 10 times higher than the ones at $\Delta t = 25$. Which means that smaller time-delays may induce a stronger shock wave, followed by a stronger rarefaction wave leading to larger nanostructures. However, larger time-delays can reduce the shock wave intensity.

5.2.2 Surface dynamics for single and double pulses

Figure 5.2(A) presents the surface dynamics upon ultrashort laser irradiation with a single pulse and horizontal polarization. The process is started by inhomogeneous energy absorption, followed by the presence of electromagnetic pattern at t = 10 ps after electron-ion thermal equilibrium. Later on, at 15 ps $<$ t $<$ 25 ps, the lattice density is strongly influenced by an inhomogeneous shock wave and rarefaction wave. The destabilization occurs, the surface starts to melt inhomogeneously and the liquid flow is driven by transverse surface tension forces, rearranging the material from hot spots to colder regions on the surface [17]. Anisotropic temperature gradients generate hydrothermal waves and convection rolls in a disturbed thin liquid layer [103][104]. This generates Marangoni forces balanced by thermal diffusion that reorganize the material over the surface into the most compact hexagonal way. Therefore, the dimensions of the cell are correlated to the Marangoni number which is equivalent the ratio between the destabilizing Marangoni force and the viscous restrictive force.

In order to understand the surface dynamics of double pulses and the significant role of time-delay, Figure 5.2(B) was established based on the simulation presented in Figure 5.2(A) combined with experimental results. This Figure allows us to understand the transitions from 100 nm to 10 nm nanostructures height. Therefore, three different regions are presented in Figure 5.2(B), based on time-delay. The first region is surrounded by a blue dashed rectangle, it presents the low time-delay region where 0 ps $\leq \Delta t \leq$ 6 ps. In this region, the role of time-delay is less significant compared to other regions. Here the ultrafast laser act like a single pulse, but with crossed polarization. Thus, no typical HSFL were formed in this region. Breaking the surface isotropy at $\Delta t \approx 0$ ps has revealed the appearance of new types of nanostructures, named as nanocrosshatch and nanobreath-figure at 0.18 J/cm²

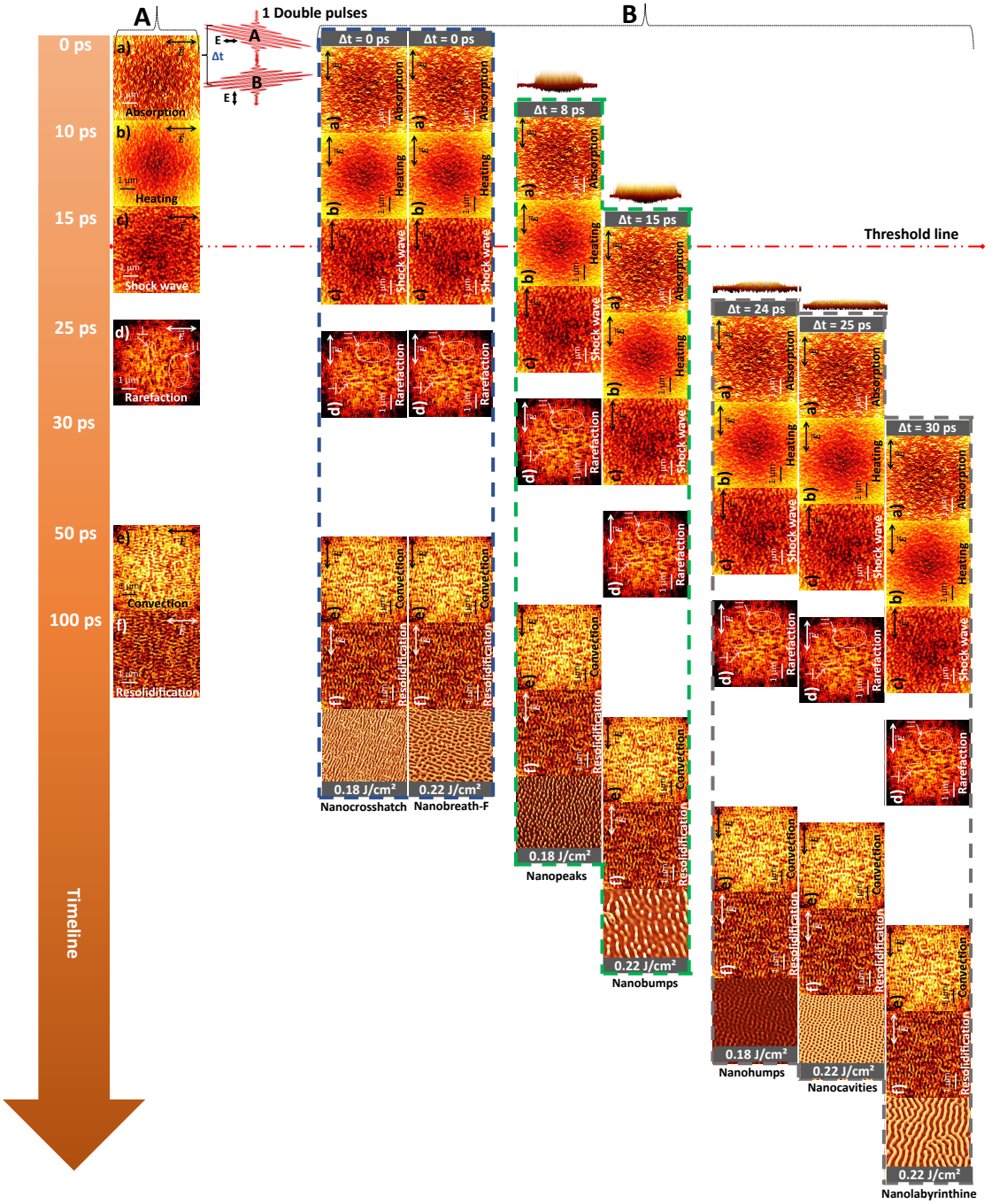

Figure 5.2: (A) Surface dynamics upon ultrashort laser irradiation with peak fluence F ¼ 0:5 J/cm². (a) Absorbed energy on the initial surface, (b) maximum temperature distribution, and density snapshots (c-f) in the transverse and (g) in the propagation plane are shown. (B) Surface dynamics of the second pulse presenting three different regions surrounded in blue for Δt = 0 ps, green for 8 ps $\leq \Delta t \leq$ 15 ps and gray for 24 ps $\leq \Delta t \leq$ 30 ps. A time-delay threshold was observed at $\Delta t \approx$ 16 ps, which transform the nanostructures height from $\approx$ 100 nm to $\approx$ 10 nm. This figure is assembled based on simulation [17] combined with our experimental results.

and 0.22 J/cm² accordingly. Therefore, increasing the laser fluence has induced a stronger shock wave followed by a more intense rarefaction wave, which lead to the transformation from nanocrosshatch to nanobreath-figure. Furthermore, the second region is surrounded by green dashed lines where 8 ps $\leq \Delta t \leq$ 15 ps. This region is particular since we had the formation of high aspect-ratio nanopeaks and nanobumps, the height of these two nanostructure is $\approx$ 100 nm. At t = 8 ps, the surface has absorbed the single pulse and started heating. In this moment, the second pulse has reached the surface to enhance the heating and created special convection cells at N = 14 p as stated in chapter 4, which they will be transformed to crests and nanopeaks at N = 25 p. More details are presented in the below section. At t = 15 ps, the shock wave has started at the same time when the second pulse has reached, leading to the formation of nanobumps with a height of $\approx$ 100 nm. However, just by increasing the time-delay above 16 ps, we observed a different types of nanostructures with low height, surrounded by gray dashed lines. The time-delay threshold line is identified at $\Delta t \approx$ 16 ps, just after the shockwave propagation. At 24 ps $\leq \Delta t \leq$ 30 ps, the second pulse has reached a surface in a rarefaction state in the opposite direction of ultrafast laser propagation, which lead to a reduction of the rarefaction wave intensity and form smaller nanostructures height, known as nanohumps, nanocavities and nanolabyrinthine. The transformation from nanohumps to nanocavities can be explained by the augmentation of laser fluence, which changes the liquid viscosity as discussed in the following section.

5.2.3 From nanohumps to nanocavities

The nature and the orientation of the resulting standing waves is defined by the dimensionless number of Prandtl, which expresses the ratio between the kinematic viscosity and thermal diffusivity and which is leading to hydrothermal waves perpendicular to transverse temperature gradients [103][105]. It makes it possible to understand whether the thermal phenomenon is more or less rapid than the hydrodynamic phenomenon. If the Prandtl number is small, then it should be understood that the phenomenon of thermal conduction is so fast that the velocity profile has little or no effect on the temperature profile.

However, for a large Prandtl number, the temperature gradient in the fluid will be strongly influenced by the local velocity of the fluid. It is demonstrated that there exists a critical Prandtl number [106] $P_r^c = 0.25$ such as: For $P_r < P_r^c$, the production of kinetic energy is intensified by isoenergetic redistributions of vorticity that lead to a concentration of the vertical velocity in the vicinity of the center of the cell. Therefore, the convection sets in as a pattern of hexagonal cells with downward motion in the center ($g-$hexagons) which are similar to the obtained nanocavities. On the other hand, for $P_r^c < P_r$, the intensification of kinetic energy production by expansion of the energy-producing temperature gradient constitutes the reason for the preference of l hexagons in high-Prandtl-number convection. Therefore, the conventional hexagonal cells with upward motion in the center ($l-$hexagons) appear at the onset of instability [107][108], which are similar to the obtained nanohumps.

In our case, the time delay plays a major role for controlling the viscosity of the liquid layer. For example, when the time delay is higher than 10 ps, the second pulse shock wave reacts with a surface that already was cooling down, promoting the formation of

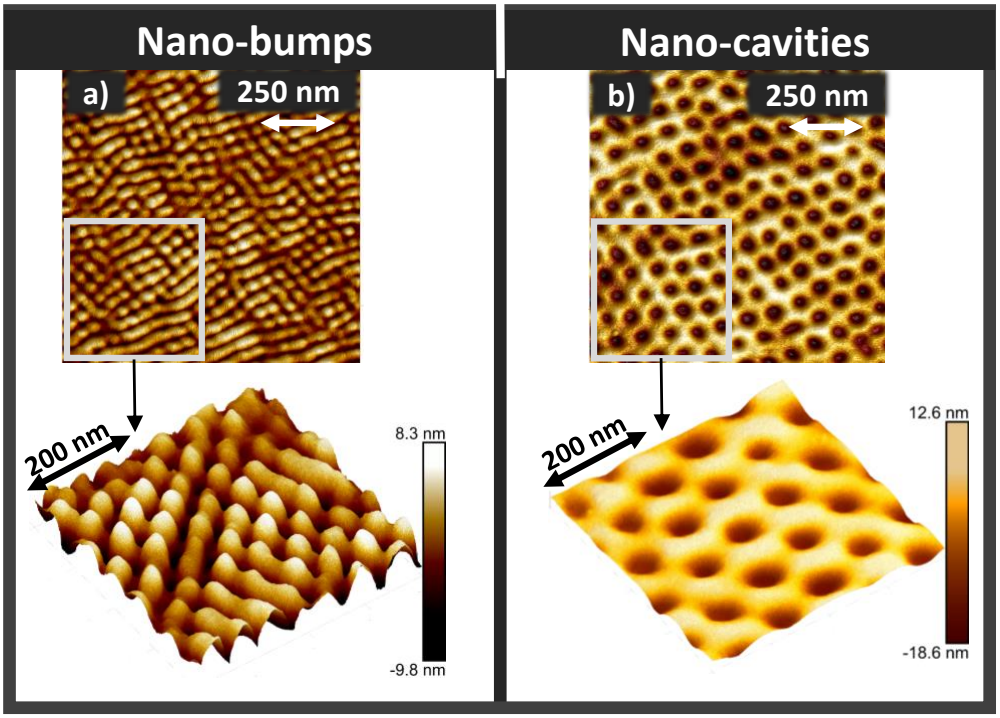

Figure 5.3: 3D-AFM images of the previsouly observed (a) nanobumps and (b) nanocavities.

nanohumps at low irradiation fluence. The mechanism ends up with resolidification of the liquid fluid, when surface lattice is cooling and the Marangoni forces decrease (after t = 100 ps) [17].

5.2.4 Formation of high aspect-ratio nanopeaks

3D simulations of the energy deposition and material modification on the Ni surface were performed. The absorbed energy density was calculated based on the solution of Maxwell equations (for electric and magnetic fields $\vec{E}$ and $\vec{H}$) by using the finite-difference time-domain (FDTD) method with the auxiliary equation for polarization current $\vec{J}$ (Drude model for Ni metal with ω_{pl} and ν plasma and collision frequencies) [73] as follows

$$\begin{cases} \dfrac{\partial \vec{E}}{\partial t} = \dfrac{\nabla \times \vec{H}}{\epsilon_0} - \dfrac{1}{\epsilon_0}\vec{J} \\ \dfrac{\partial \vec{H}}{\partial t} = -\dfrac{\nabla \times \vec{E}}{\mu_0} \\ \dfrac{\partial \vec{J}}{\partial t} + \vec{J}\nu = \epsilon_0 \omega_{pl}^2 \vec{E}. \end{cases} \tag{5.1}$$

The absorbed energy was defined as $I\alpha_{abs}$, where $I = \frac{1}{2}\sqrt{\frac{\epsilon_0}{\mu_0}}\left|\vec{E}\right|^2$ is the intensity and α_{abs} is the absorption coefficient related to the extinction coefficient k as $\alpha_{abs} = 4\pi k/\lambda$. Then, a two-temperature model (TTM) was implemented to resolve electron-ion heat transfer and

diffusion [74] and compressible Navier-Stokes equations [72, 75] were applied as follows

$$\begin{cases} C_e \dfrac{\partial T_e}{\partial t} = \nabla \cdot (k_e \nabla T_e) - \gamma_{ei}(T_e - T_i) + I\alpha_{abs} \\ \rho C_i \left[\dfrac{\partial T_i}{\partial t} + \vec{u} \cdot \nabla T_i \right] = \nabla \left(k_i \nabla T_i \right) + \gamma_{ei}(T_e - T_i) \\ \dfrac{\partial (\rho \vec{u})}{\partial t} + (\vec{u} \cdot \nabla)(\rho \vec{u}) + (\rho \vec{u}) \nabla \cdot \vec{u} = \\ = -\nabla (P_e + P_i) + \mu \nabla^2 \vec{u} + \dfrac{1}{3} \mu \nabla (\nabla \cdot \vec{u}) \\ \dfrac{\partial \rho}{\partial t} + \nabla \cdot (\rho \vec{u}) = 0, \end{cases} \tag{5.2}$$

where $\vec{u}$ and ρ are the fluid velocity and density, T_e and T_i are the electron and ion temperatures, P_e, C_e and k_e are the electronic pressure, the electron heat capacity and conductivity evaluated based on the results of ab initio calculations [109], P_i is the lattice pressure defined by the equation of state (EOS) [110], μ, C_i and k_i are the ion viscosity, heat capacity and thermal conduction.

Hexagonal distribution of nanocavities (half-spheres of radii $R \pm \Delta R = 30 \pm 15$ nm with centers on $Z = 0$ and inter-distances of $L \pm \Delta L = 80 \pm 10$ nm) was initially set on the Ni surface. The cross-polarized pulses with combined fluence of $F = 0.18$ J/cm^2 were applied with a delay of 8 ps as in experimental irradiation conditions.

Early in the feedback process, near-field enhancement on local depression turns to nanocavities that self-organize into an hexagonal 2D lattice. This results from hydrothermal flows guided by surface tension and rarefaction forces developping a thermoconvective instability at the nanoscale and, similarly to well-known Rayleigh–Bénard-Marangoni instabilities, generate convective cells as shown in Figure 4.10 [72, 83]. The growth of the laser-induced structures from quasi-hexagonal cavities to uniform nanopeaks is analyzed by combined electromagnetic and hydrodynamic approaches explained in numerical details section. The absorbed energy deposition on the Ni surface, nanostructured with some hexagonally arranged nanocavities, is firstly calculated by 3D Maxwell equations and shown in Figure 5.4(a,b) for cross-polarized ultrashort laser pulses. For the nanocavity concentrations observed in the experiments (sub-wavelength inter-distances of ≈ 80 nm), strong collective effects in quasi-periodic lattices are expected, deviating from the individual response of the nanocavities. For the sake of generality, nanocavity distributions with randomly varying depths and slight deviations of the centers from the exact hexagonal order were considered, in accordance to the experimental observations done in Figure 4.10(a). These small imperfections were shown to have negligible effects on the qualitative optical response of the quasi-periodic system. Nevertheless, the ratio between the intercavity distance and the cavity radius should be small enough (< 5) to support strong near-field enhancement, induced by neighbor nanocavities.

The distance between the closest nanocavities positioned perpendicular to laser polarization defines the dominating regime for each laser pulse. For instance, the intensity averaged over the period is amplified along the lines perpendicular to the polarization in Figure 5.4(a) if the distance is small enough. The enhancement along the diagonal axes is also present, though a weaker effect. In contrast, the intensity is amplified dominantly

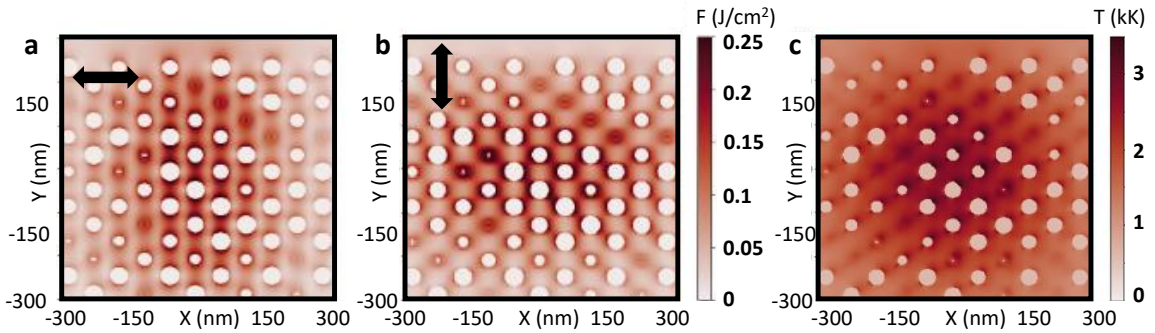

Figure 5.4: a-b) Energy density absorbed below Ni surface with hexagonal distribution of nanocavities by the first (a) and the second cross-polarized pulse (b). c) equilibrium temperature distribution after double pulses applied with a delay of 8 ps. Distributions are shown in the plane perpendicular to laser incidence (along Z) 10 nm below the upper surface level $Z = 0$.

along the diagonal axis when the inter-distance along the horizontal axis is wider in Figure 5.4(b). Furthermore, the application of cross-polarized pulses results in the uniform total absorbed energy deposition (and therefore, temperature distribution) in the vicinity of nanocavities, cancelling the paramount directional absorption from individual near-field effects. As a result, the combination of double pulses renders higher temperatures along one of the diagonal axis of the hexagonal cavities as shown in Figure 5.4(c) rather than perpendicular to one of the applied fields. The equilibrium temperatures along the diagonal axis are high enough to induce phase transitions, i. e. melting of the Ni surface. Their consequence might be seen in the experimental results prior to the formation of nanopeaks.

In the propagation plane, the combined action of cross-polarized pulses results in the increased temperatures on the top of the nanostructures. This is the consequence of the cancelling of directional individual responses of the nanocavities, which would amplify the intensity beneath the nanocavities if a single perpendicularly polarized pulse is applied. The fluid dynamics simulations are further performed in order to elucidate the driving mechanisms of the nanopeak growth.

The instantaneous pressure P and fluid velocities U_z are provided in Figure 5.5(a-h). The snapshots are taken at different stages of the structure evolution: heating by the first pulse (a, e), the surface state at the moment when the second pulse is applied (b, f), temperature equilibrium attained after heating by the second pulse (c, g) and, finally, the growth and saturation of the nanopeaks (d, h). The positive velocities indicate the potential material flow above the surface, whereas the negative values stand for the movement below the surface, for instance, shock wave propagation in the bulk of the material. The role of the delay between the cross-polarized pulses (here, 8 ps) becomes evident while comparing the pressure distributions (b) at first and (f) at second pulse energy deposition. The negative pressures of -3 GPa indicate the initiated melting processes at the top of the nanostructures, therefore, the second pulse starts heating the peaks in the liquid phase. The difference between ultrafast heating of solid and liquid Ni with a reduced density originates from the instantaneous drop in temperature keeping the density unchanged and elevated transition

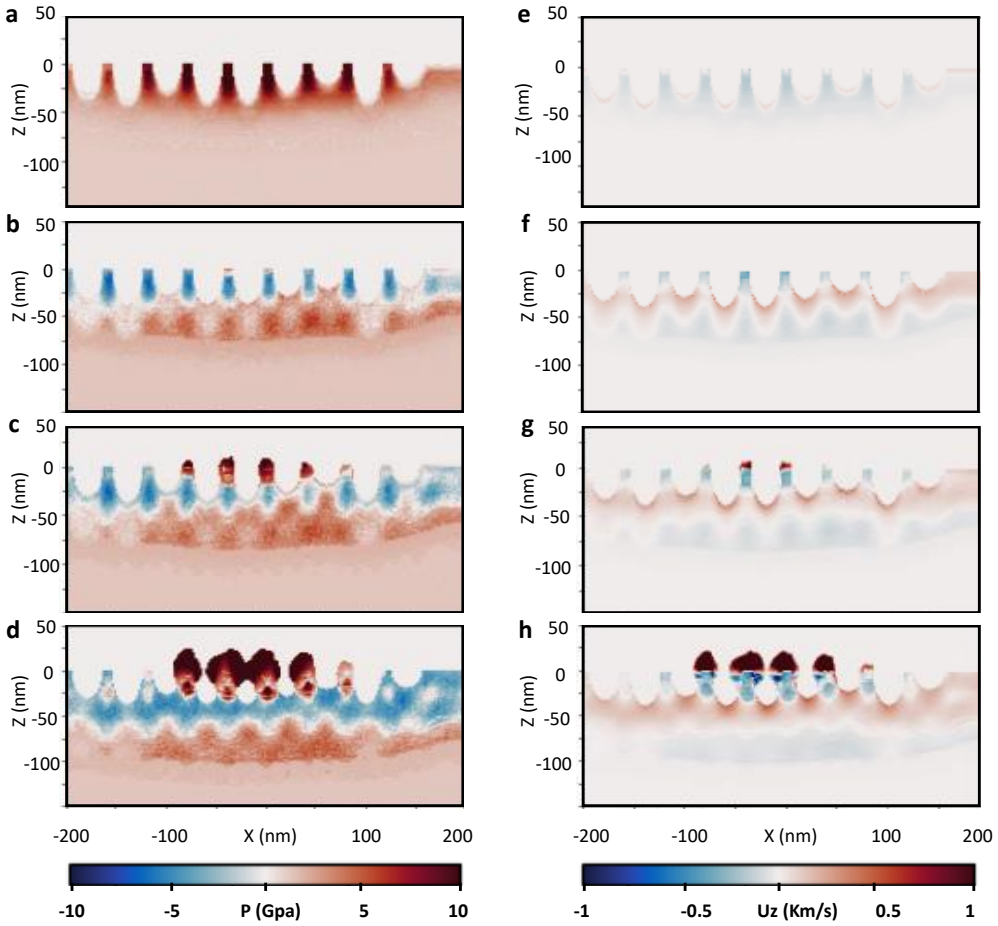

Figure 5.5: a-d) Instantaneous EOS pressure P and (e-h) fluid velocities u_z beneath the surface (a,e) 4 ps, (b,f) 8 ps, (c,g) 16 ps, and (d,h) 24 ps after the first pulse excitation. The cross-sections are taken for $Y = 0$ in the propagation plane.

temperature (from positive to negative pressures $P(\rho, T_i)$) for a liquid state. As a result, the positive pressures (compressive stress of ≈ 8 GPa) can be build at the top of the nanostructures, where the difference between negative pressures below the surface and on the top creates upwards fluid movement above the initial level of surface. The peaks can grow by tens of nanometers according to the numerical predictions as shown in Figure 5.5(d) and are latter stopped by the dominating diffusion processes. This localized high mechanical stress is probably the cause of the crystal disorientation revealed by HR-STEM in in Figure 4.7(c-e).

The experimental results for different number of applied pulses (20 - 30) in Figure 4.9 indicate that the nanopeaks grow swiftly up to ≈ 100 nm heights and then saturate, covering the irradiated area almost homogeneously. The growth saturation can be explained by drastic changes in the optical response of the surface topography, resulting in a smaller field enhancement on the top of the nanostructures. As a result, the temperature increase drops

down and the pressure gradients are not strong enough to contribute to further growth of the nanopeaks above the established height. Instead, the energy is more efficiently absorbed on the surface, resulting in less regular long nanostripes, connecting the neighbor nanopeaks for a higher number of applied pulses (30 - 50).

The experimental results and the performed calculations allow us to get insight into the nanostructure formation mechanisms as well as into the specific laser irradiation conditions required to control over the observed phenomenon. The unique role of cross-polarized laser pulses with equal amount of energy in concentrating light and heat at the nanoscale and in avoiding the formation of field-aligned patterns has been already evidenced in previous works [22, 83]. Specifically, the nanocavities and the nanobumps were attributed to convection instability in a thin liquid layer of Ni. As soon as these nanostructures densely and homogeneously cover the surface after multiple pulse irradiation, the light is trapped by the sub-wavelength structures and results in even more extreme conditions in a thin liquid layer. Additional parameter which is crucial is a choice of double pulse delay. If a delay is much shorter than the time required for energy transfer between electrons and lattice, both pulses interact with solid material and their action sums up. If a delay is much longer than the electron-ion transfer time, the diffusion effects tend to produce homogeneous temperature and pressure distributions, with less pronounced nanoscale hot spots. The intermediate regime is of particular interest because the temporal scales correspond to the initiation of phase transitions. Additionally, the fluence should be adapted in order to induce pronounced material modifications only where the light is confined by the nanostructures to avoid the uncontrolled damage. The influence of pulse duration in sub-picosecond range indicates the potential role of transient optical properties out of thermal equilibrium as well as the liquid state gradients in the efficiency of nanoscale energy deposition.

5.3 Self-organized nanopatterns by Swift–Hohenberg (SH) equation

As presented in the previous section, nanoscale fluid flows were shown to be driven by a complex interplay between electromagnetic, internal and surface pressure forces that can be trapped due to resolidification process. The prediction of underlying laser-coupling processes is constrained by a deterministic approach integrating low fluctuation conditions by surface roughness. Stationary patterns can become unstable under nonlinear amplification and bifurcate into more complex patterns that cannot be reliably described by classic approaches such as Navier-Stokes combined with Maxwell equations. However, experimental patterns that can be confronted with mathematical models dedicated to nonlinear system dynamics are now sufficiently characterized, enabling to explore the available phase space.

In this section, our original strategy relies on the use of Machile Learning (ML) integrating partial physical information in the form of the SH model to identify dominating stable modes for a set of parameters *independently* from initial roughness conditions. This strategy will allow us to solve the dual inverse problem from a single observed state, consisting of an SEM image, with little data. Our modelling is scale-invariant and can be applied to any laser process. It reduces experimental irradiation parameters to simple model coefficients,

which can then be optimized and extrapolated for surface pattern engineering.

5.3.1 Light-induced surface nanopatterning

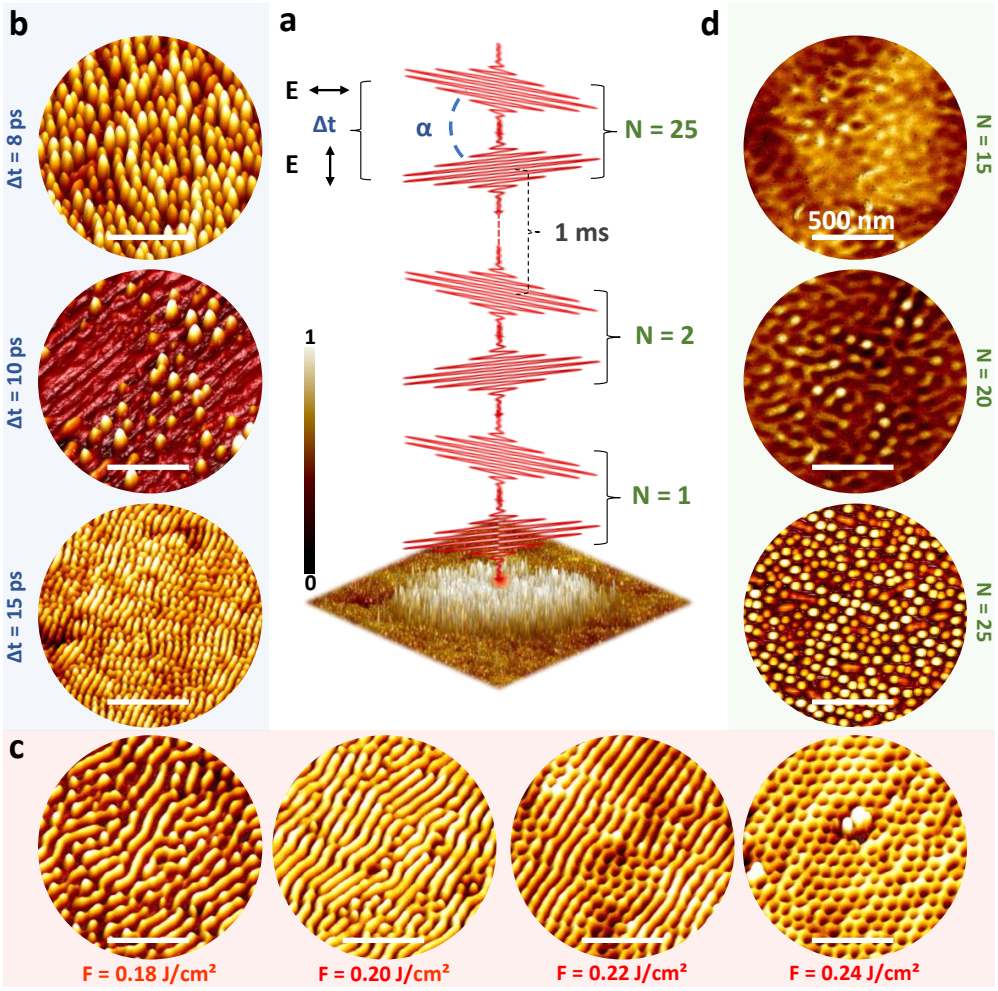

Figure 5.6: (a) Schematic illustration of experimental self-organization regimes induced by bursts of ultrafast laser double pulses. (b) Self-organized patterns of topography that develop varying time delays for a given F and N (AFM-3D mode). (c) Nanopatterns variation with respect to laser fluence at fixed Δt and N (AFM-3D mode). (d) Nanostructure growth by feedback at different number of pulses (AFM-2D mode), for a fixed Δt and F. The scale bars represent a length of 500 nm.

Tayloring nanotopographic features on the surface is an arduous challenge which has been successfully enabled through an ultrafast laser process implying time-controlled polarization strategies. Numerous regimes of LIPSS were reported with different periodicity, height, orientation and symmetry relying on different polarization directions between the first pulse $\vec{E_1}$ and second $\vec{E_2}$, characterized by $\alpha = (\vec{E_1} \cdot \vec{E_2})$ in Figure 5.6 [4, 111]. In the proposed experiment, Mach-Zehnder interferometry enables combining the effect of po-

larization mismatch with an adjustable inter-pulse delay Δt, which leads to a fine control of the surface topography on the tens of nanometer scale [21, 22]. By breaking the surface isotropy imposed by a single polarization state, a wide range of self-organization regimes has been achieved on Nickel monocrystal oriented in the (001) direction. Using a cross polarization strategy, setting a depolarization angle of $\alpha = 90°$ and a range of time delays between 8 and 25 ps as presented in Figure 5.6(a). The pulse duration was fixed to 150 fs and the laser dose was finely controlled by the number N of double-pulses sequences. The nickel initial surface was mechanically polished with a $R_a < 5$ nm prior to laser irradiation to ensure that the surface dynamics follows a hydrodynamics-governed process smoothing the inhomogeneous electromagnetic response.

Figs.5.6(b-d) present surface topographies measured by high resolution atomic force microscopy (AFM) used in the tapping mode. A circular region of 1 μm diameter corresponding to the laser impact center has been mapped in 3D (tilted) mode in Figure 5.6(b-c) and in 2D for Figure 5.6(d). In order to observe the significant temporal pulse splitting role in nanopatterns control, laser peak fluence F and N were fixed at 0.18 J/cm^2 and 25 respectively, as presented in Figure 5.6(b). At Δt = 8 ps, organized nanopeaks structures were observed with a high aspect ratio, a height of $\sim$ 100 nm and a diameter of $\sim$ 20 nm [34]. An extension of 2 ps in Δt modifies the observed patterns that turn into a different organization, a regime referred as nanobumps [22]. For Δt = 15 ps, a regime of nanohumps generation is reached with a lower aspect-ratio as the structures display a height of $\approx$ 10 nm and a diameter of $\approx$ 30 nm.

Furthermore, by fixing $\Delta t = 25$ ps and $N = 25$, the crucial role of laser fluence in controlling nanopattern types and structures is revealed in Figure 5.6(c). At $F = 0.18$ J/cm^2, a low-contrast nanopeaks regime falls into place which evolves into nanostripes pattern under a slight laser fluence increase to 0.20 J/cm^2. At 0.22 J/cm^2, a transition region is established from a combination of stripes and cavities. Then, by increasing the laser fluence to 0.24 J/cm^2, the surface is uniformly organized with hexagonally arranged nanocavities with a depth of $\approx$ 25 nm and a diameter of $\approx$ 30 nm. Both nanohumps and nanovoids were result from hydrothermal flows guided by surface tension and rarefaction forces which develop thermoconvective instability at the nanoscale, similarly to well-known Rayleigh–Bénard-Marangoni instabilities.

On the other hand, laser dose plays an essential role in nanopatterns formation, and positive feedback regulates the pulse by pulse topographical transformations. As observed in Figure 5.6(d), three different surface organizations were observed at a fixed laser fluence of 0.24 J/cm^2 and a time-delay of 8 ps with different N, corresponding to the parameters of nanopeaks formation presented in Figure 5.6(a). Pulse-to-pulse growth dynamics exhibits the transitions from convection cells at N = 15, to the creation of crests on the convection cells at N = 20. The nanopeaks grow on the edges of the crests to reach their optimal shape, concentration and organization at N = 25.

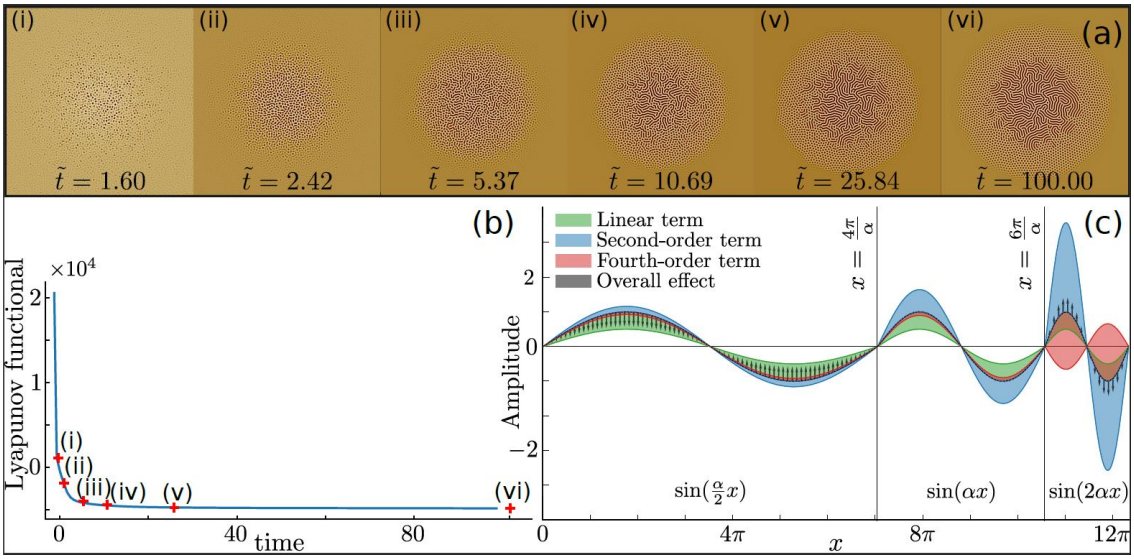

Figure 5.7: (a) Fields at solver times $\tilde{t}$, with ϵ a centered 2D Gaussian ramp to mimic the laser fluence distribution. (b) SH Lyapunov functional $V[\tilde{u}]$ converges asymptotically to a stable value. (c) the overall magnitude of SH terms is frequency dependent, giving rise to complex pattern solutions observed in (a).

5.3.2 Model prediction by machine learning

The generalized Swift-Hohenberg equation (SH) was used in an adimensional form as:

$$\dot{\tilde{u}} = \epsilon\tilde{u} - (1 + \tilde{\nabla}^2)^2\tilde{u} + \gamma\tilde{u}^2 - \tilde{u}^3. \tag{5.3}$$

SH model, which was introduced in [112] as a model of Rayleigh-Bénard convection, modified by the introduction of a u^2 nonlinearity allowing small amplitude destabilization and the existence of the experimentally observed hexagonal patterns. With appropriate boundary conditions, the original SH equation exhibits a type-I-s instability that is isotropic, invariant with respect to translations and to $u \to -u$ [113]. Perturbations of $u_b = 0$ are selectively amplified depending on the norm of the wave number, leading to the formation of complex *patterns* with no preferential direction. SH has the Lyapunov functional $V[\tilde{u}] = \int_\Omega \frac{\tilde{u}}{2}(\nabla^4\tilde{u} + 2\nabla^2\tilde{u} + \tilde{u}) + \frac{1}{4}\tilde{u}^4 - \frac{\gamma}{3}\tilde{u}^3 - \frac{\epsilon}{2}\tilde{u}^2 d\mathbf{x}$ and $\dot{\tilde{u}} = -\frac{\delta V}{\delta\tilde{u}}$. V decreases during the dynamics, converging asymptotically to a stable value [113] (Figure 5.7).

We solve numerically SH equation with a second-order Strang splitting [114–116] pseudo-spectral solver with an adaptive time step, providing a good compromise between accuracy and speed. Since the number of experimental points is not sufficient to use standard ML techniques, we use physics-guided machine learning, which allows us to restrict optimization to the space of solutions of the SH equation, which is then further restricted via a choice of feature projection that eliminates the dependency on initial conditions. Specifically, the experimental SEM images are labeled using the nearest neighbors among generated SH-

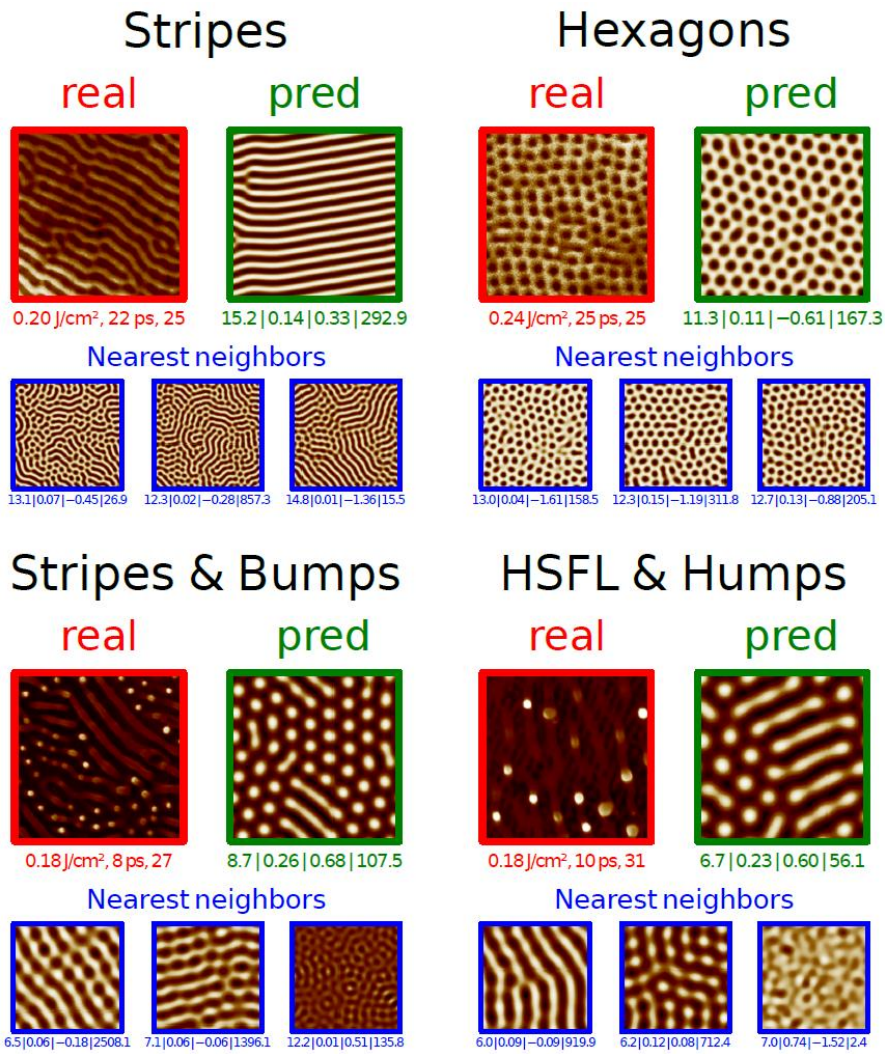

Figure 5.8: Each group shows experimental SEM images (red, never seen by the model), model predicted images (green, trained on the "full" dataset using the indirect method), given the same laser parameters and three nearest neighbors of the former among solver generated images (blue). Image labels, left to right: F, Δt, N (real images); l_p, ϵ_p, γ_p, $\tilde{t}_p$ (other images). All images are 224 by 224 pixels; for real images, 1 μm $\approx$ 237 pixels. Model's predictions are better than the nearest neighbor since they integrate global information. On the "Stripes and Bumps" group, we observe nearest neighbors with different length scales, suggesting concurrent multi-scale SH processes taking place. Only one of these can be recovered by the ML model (the stripes, rather than the nanobumps), which integrates single-scale SH knowledge. On the "HSFL and Humps" group, the real image has a top, low-frequency pattern, and a finer grid pattern underneath. The model predicts the former, which is also the only among the nearest neighbors.

solver solutions on this feature space, and support vector regressor machine learning model is trained on this labeled data to predict SH-equation parameters from laser parameters.

The SH parameters predicted by the ML model can then be used by the SH solver to

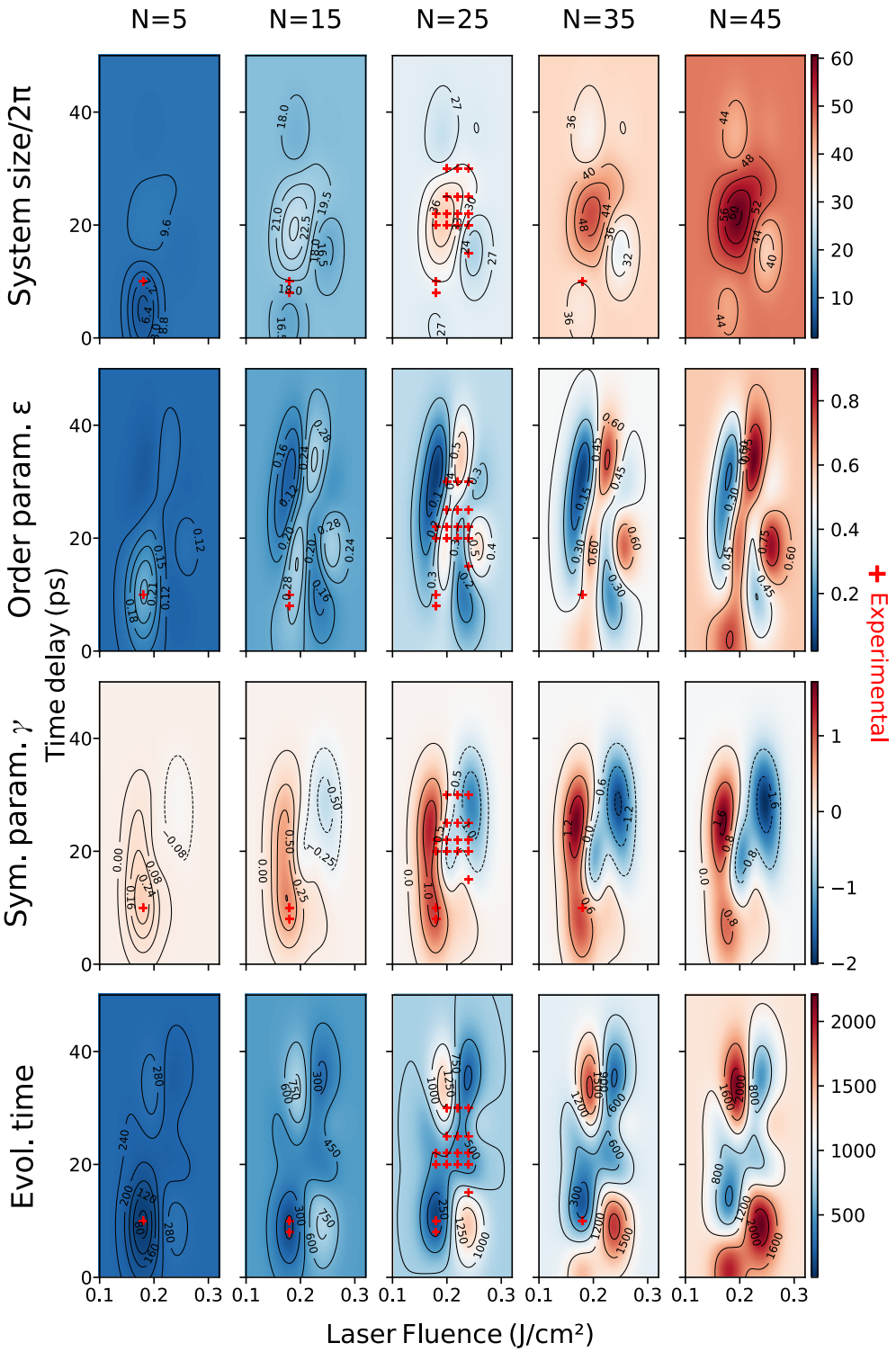

Figure 5.9: Each plot shows the ML model prediction of a single SH parameter (bottom to top: scale factor l_p; order parameter ϵ_p; symmetry breaking parameter γ_p; simulation stabilization time $\tilde{t}_p$) as a function of laser fluence, time delay, and number of pulses (respectively, x-axis and y-axis, and column). Experimental points are overlaid on each plot.

generate solutions corresponding to unseen laser parameters. We present in Figure 5.8 the generated solutions from unseen laser parameters together with the corresponding real SEM image and nearest neighbors in feature space. Comparing solutions generated by the model from unseen test data to real SEM images allows further interpretation. The model does quite well for the 'Stripes' and 'Hexagons' group, as there is a single pattern to learn. For the two other groups, there is more than one pattern/feature superimposed on the SEM image. Note that the model does predict one of the observed patterns with the correct scale and shape but, by design, it cannot possibly predict the other. For the 'Stripes and Bumps' group, for instance, we observe nanopeaks and lower-frequency stripes among the nearest neighbors, whereas the model predicts the lower frequency pattern only. For the "HSFL and Humps" group, where the difference in pattern frequency is more pronounced, again the model focuses on the lower frequency pattern; the high-frequency pattern is no longer among the nearest neighbors.

We observe in Figure 5.9 that the complexity of the learned relationship increases with the number of observations, with sharp boundaries of rapidly varying parameters appearing where data is sufficient. The ML model is able to extrapolate to regions with few data for N and Δt, but less so for F, which would require a more resolved experimental mapping. Importantly, predicted SH parameters are correlated, and the sign of the correlation changes with N, which imposes constraints on pattern design. As an example, consider the predicted SH parameter l_p, which is inversely correlated with pattern characteristic size and increases with N (the increase is not uniform, being greater for large l_p regions). While we cannot set the characteristic size of a given stable mode defined by $\epsilon_p, \gamma_p, \tilde{t}_p$ freely, we have a modicum of control:

For e.g. $N = 25$, we observe a high-gradient transition regime for l, at $F = 0.18$ J/cm², $\Delta t = 15$ ps in the Δt direction. For $F, \Delta t$ in the same region, the other SH parameters remain roughly constant. Varying l_p in the direction of ∇l_p would thus allow adjusting the characteristic size of the particular stable mode defined by the other SH parameters, which is of great interest to applications. Interestingly, (γ_p) determines whether we observe holes or bumps; $F = 0.2$ J/cm² separates a region of high and low γ_p, roughly independently of N; the sign of γ_p appears to be determined by F and Δt only. Also, for large bifurcation parameter (ϵ_p), many modes are non-attenuated and patterns are less ordered ; correspondingly, we observe large ϵ_p patches at high F/low Δt (highest energy coupling). For $N = 25$, superimposing the $\gamma_p = 0$ isosurface on the ϵ_p prediction, we observe that it is roughly perpendicular to isosurfaces of ϵ_p. These abrupt transition regimes of ϵ_p are consistent with experimental observations where *two* patterns of different order are superimposed on the *same* SEM image. ($\tilde{t}_p$) for constant $l_p, \epsilon_p, \gamma_p$, symmetry increases with $\tilde{t}_p$, as symmetrical patterns require large $\tilde{t}_p$ to stabilize from a uniformly random state. As can be seen in the bottom row, $\tilde{t}_p$ tends to increase with N, consistently with the physical view, as a large N increases the time, the dissipative system is in a far from equilibrium state. This increase is not uniform across $F, \Delta t$ pairs, and the area of laser parameter space of relatively large $\tilde{t}_p$ decreases with N.

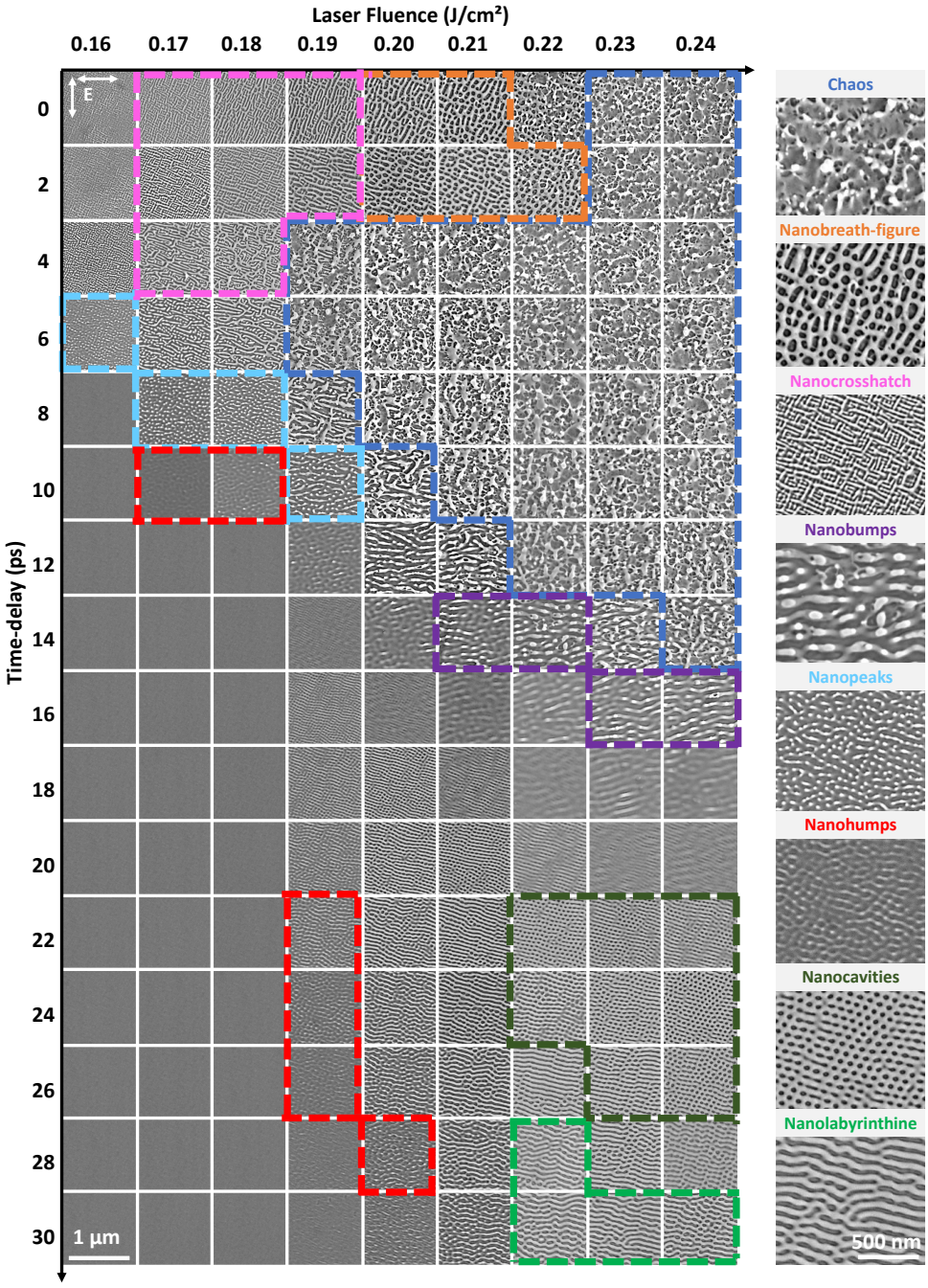

Figure 5.10: Scanning electron microscopy of a Ni(001) crystal irradiated by 25 double-pulses sequences at an incident laser fluence range from 0.16 to 0.24 J/cm^2 with time-delay range from $0 \leq \Delta t \leq 30$ ps between the two crossed polarizations. The nanostructures domains are presented in different colored regions such as: dark blue for chaos, orange for nanobreath-figure, pink for nanocrosshatch, light blue for nanopeaks, red for nanohumps, purple for nanobumps, dark green for nanovoids and light blue for nanolabyrinthines. The laser polarization E is indicated by the white arrow.

5.3.3 Self-organization observation by entropy interpretation

Several organization regimes are presented in Figure 5.10 controlled by laser fluence and time-delay (Δt) between the two cross-polarized pulses at a fixed number of double-pulses sequences of 25 and pulse duration of $\approx$ 100 fs. A total of eight different morphologies are observed. In Figure 5.10, the chaotic regime is presented in dark blue color, it is obtained at low $\Delta t \leq$14 ps and laser fluence between 0.19 and 0.24 J/cm^2.

The nanobreath-figure are observed in a smaller region where $\Delta t \approx 0$ ps and for a laser fluence between 0.20 and 0.22 J/cm^2. These nanopatterns are identified for the first time on Nickel. They have an unorganized cavity shape with dimensions at the nanoscale[117][12]. Nanocrosshatch are also observed at a $\Delta t \approx 0$ ps but at lower laser fluence between 0.17 and 0.19 J/cm^2. In this regime, two diagonal nanostripes superposed perpendicularly to each other are observed.

At larger time-delay between 6 ps $\leq \Delta t \leq$ 10 ps, the nanocrossatch are being transformed to a high aspect ratio nanopeaks. They have a diameter of $\approx$ 20 nm and a height of $\approx$ 100 nm[34]. By increasing the time-delay, nanopeaks are being transformed to nanobumps with a lower aspect ratio, they almost have a same height compared to nanopeaks but with a larger diameter of $\approx$ 100 nm and less concentration. They are presented in the purple region in Figure 5.10. The nanohumps are presented in red color, they are found at time delay $\geq$ 10 ps. They are small humps with a low aspect ratio and a height around 10 nm. The nanovoids or nanocavities are formed at higher energy above 0.19 J/cm^2 and they are presented in dark green color. Their size is increasing while increasing the laser fluence to reach homogeneous shapes and organizations at a laser fluence of 0.24 J/cm^2 and a time delay of 24 ps. Furthermore, labyrinthine nanostructures are observed at high laser fluence between 0.22 and 0.24 J/cm^2 and a large time-delay between 28 $\leq \Delta t \leq$ 30 ps. The fascinating labyrinthine shape is formed at a laser fluence of 0.23 J/cm^2 and a time-delay of 30 ps. The degree of instability of such patterns is so high that the nanostructure shape organization can be altered by a few picoseconds delay change. These states are characteristic of attractors toward which the dynamical system tends to evolve in dissipative structures. The door is open to describe mathematically the nonlinear dynamics of laser-induced surfaces with models able to reproduce the variability of the patterns in the phase space and explore the origin of bifurcations.

The Shannon entropy, due to Claude Shannon, is a mathematical function which, intuitively, corresponds to the quantity of information contained or delivered by a source of information. This source can be a text written in a given language, an electric signal or a computer file (collection of bytes). From the point of view of a receiver, the more different information the source sends, the greater the entropy (or uncertainty about what the source is sending). Thus, if a source always sends the same symbol, for example the letter 'a', then its entropy is null, i.e. minimal. Indeed, a receiver who only knows the transmission statistics of the source is assured that the next symbol will be an 'a'. On the other hand, if the source sends an 'a' half of the time and a 'b' the other half, the receiver is uncertain of the next letter to receive. The entropy of the source in this case is thus non-zero (positive) and represents quantitatively the uncertainty that reigns on the information emanating from the source. The entropy then indicates the amount of information necessary

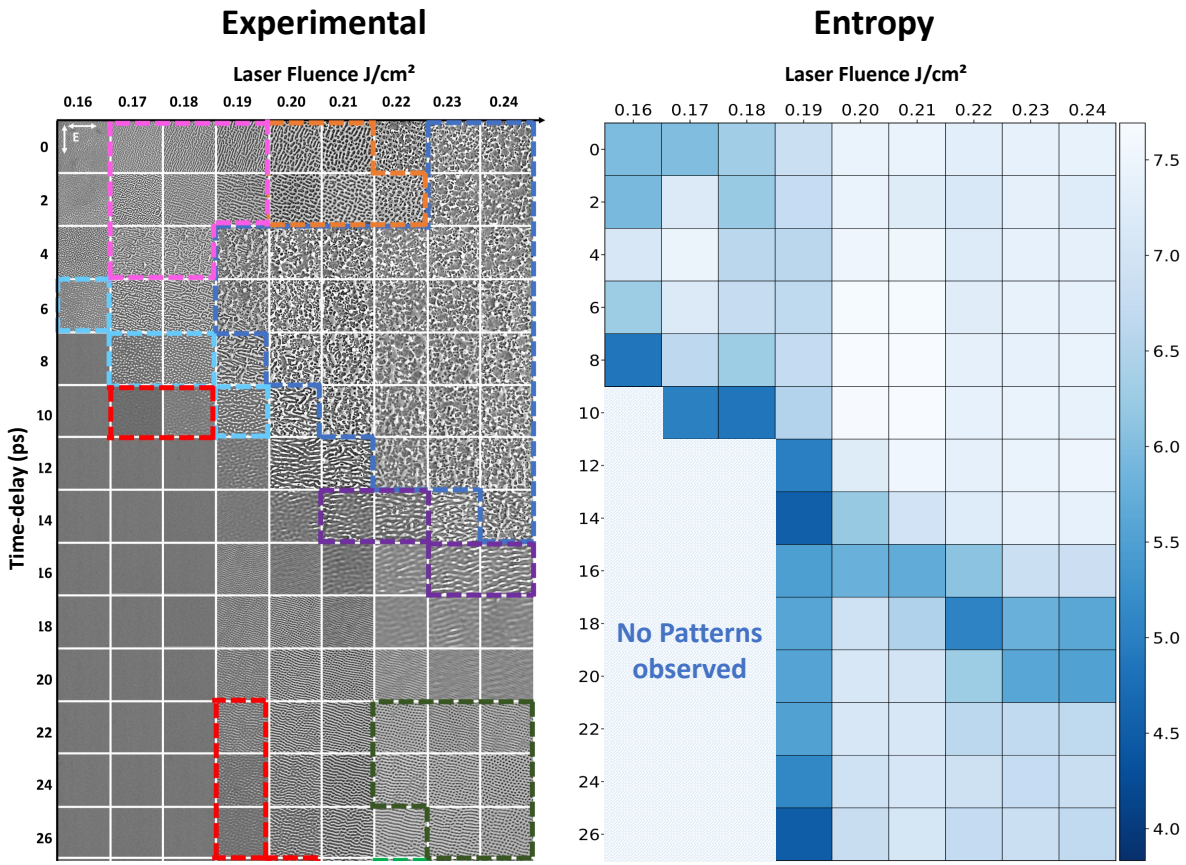

Figure 5.11: Comparison between experimental results and interpreted results, presenting the entropy of each image at different parameters.

for the receiver to determine unambiguously what the source has transmitted. The more information the receiver receives about the transmitted message, the greater the entropy (uncertainty) about this message. In particular, the more redundant the source is, the less information it contains. In the absence of particular constraints, the entropy is maximal for a source whose symbols are all equiprobable.

Figure 5.11 presents a good agreement between experimental and post-interpreted images. We can observe a low entropy at the regions where the self-organised structures specially for the high aspect ratio nanopeaks, nanocrosshatch and nanombumps. The entropy is higher for the low height nanostructures like nanocavities.

5.4 Conclusion

Laser beam polarization is timely controlled to prevent anisotropic energy absorption and to synchronize the laser energy delivery rate with the material dynamic response. This strategy upgrades the energy coupling and the structure growth explained by a state-of-the-art Maxwell-hydrodynamic simulation. Initiated by convective instabilities at the nanoscale,

we demonstrate that the crossed pulses polarization cancels the individual response of each nanorelief due to near-field optical enhancement and enables a collective response of the dissipative structure.

On the other hand, we show that ultrafast laser-irradiated surface nanoscale patterns can be numerically modelled by a scale-invariant generalized Swift-Hohenberg equation. A machine learning model is trained to learn the connection between the stochastic SH equation and laser parameters, independently of initial conditions, using a deep convolutional network to extract features and by incorporating physical information. The model is able to identify laser parameter regions of interest for applications and, since CNN features are not learned on observed patterns, can even be used for novel pattern prediction. Regions where pattern superpositions are observed could be modeled more accurately via a mixing of SH processes, as a manifestation of superposed states of self-organization, providing new routes toward nanoscale surface manipulation by light. These results and related discussions have been published in Entropy and WILEY, Advanced Science journals [89, 118].

Chapter 6

Applications

Là où il y a une volonté, il y a un moyen.
Il faut y croire

– Samar Elias Matta

In this chapter, we present the evaluation of microscopic and macroscopic properties of irradiated materials. Physico-chemical analysis of textured Ni sample were performed at GIE MANUTECH, the preliminary results show a slight improvement in surface hydrophobia. Furthermore, nanostructures Ti samples show a good potential in manufacturing antibacterial surfaces, which open the doors for several studies in this domain. These tests were carried out in at SAINBIOSE laboratory within the framework of Steve Papa's thesis.

6.1 Physico-chemical and antibacterial analysis of textured Ni

This experiment aims to compare the wetting behavior of an oriented nickel sample (001), before and after fs laser nanoscale texturing. The challenge of the study is to identify the contribution of nanoscale texturing to surface functionalization. A sample of Ni (001) was analyzed to identify its hydrophilic or hydrophobic character. The sample, having undergone nano-structuring by femtosecond laser, its contact angle with a drop of water was measured both on the textured part, as well as on the polished part, in order to identify the behavior to the wetting of these two surfaces. Multiple bibliographic studies have shown that a metallic surface evolves chemically for one or more tens of days (more or less, depending on the material) after femtosecond laser treatment, then it reaches a stabilized state of passivation. This is the reason why this study was carried out several months after the laser texturing. Contact angle measurements were performed at room temperature (22.6 ± 0.1°C) using drops of ≈ 3 µl ultrapure distilled water. The relative humidity level during the tests was 42%.

6.1.1 Ni texturation on a larger surface

In this section, the used Ni (001) samples were mechanically mirror polished by Automatic polishing procedure 1 of Figure 2.2, obtaining an initial R_a of ≈ 1 nm. The samples were irradiated using a SCANLAB scanner introduced previously in chapter 2. Several laser irradiation tests were carried out by varying the fluence and the recovery rate. First, these tests were performed on small surfaces with sizes ranging from a hundred microns to a few millimeters in order to control the type of structuring generated and the homogeneity of the surfaces. Figure 6.1 shows SEM images of a nickel sample irradiated at an incident laser fluence of 0.18 J/cm², time-delay Δt = 8 ps between the two crossed polarizations (nanopeaks parameters), at different number of double-pulses sequences and different spacing or scanning overlap. Further irradiations presented in Figure 6.2 and Figure 6.3 have allowed us to determine the most suitable scanner conditions, in function of coverage and overlap ratio, for the generation of nanopeaks while keeping the experimentation time reasonable.

The ablation spot diameter (D) was measured for each condition (dependent on laser fluence, time-delay and number of double-pulse sequences), and the ablation spot area was calculated (A=$\pi D^2/4$). The distance between irradiation spots d_s was determined to control the overlap ratio (OL) and coverage percentage (C_v) such as: OL = 1-(d_s/D) and

C_v=(A×N_p)×100, where N_p is the number of pulses per unit square (dependent on d_s).

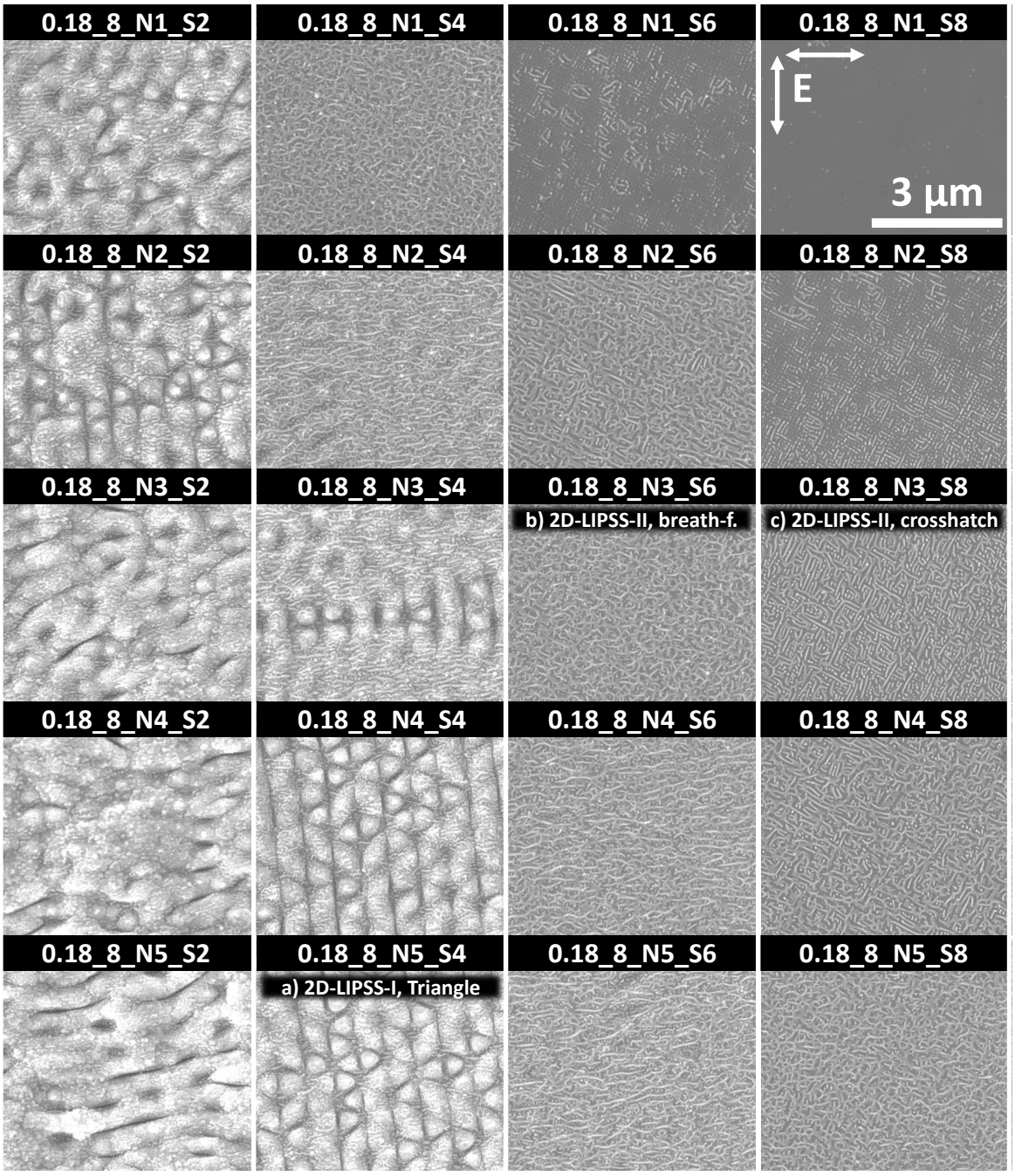

Figure 6.1: Scanning electron microscopy of a Ni (001) sample irradiated at an incident laser fluence of 0.18 J/cm², time-delay Δt = 8 ps between the two crossed polarizations, at different number of double-pulses sequences and different spacing (d_s). The image titles present the irradiation parameters accordingly such as: Laser fluence in J/cm², time-delay in ps, number of double-pulse sequences and spacing or steps between scanner impacts (d_s) in µm. 2D-LIPSS type I are observed in (a) in an almost triangular shape. However, 2D-LIPSS type II are observed in (b) and (c) for nanobreath-figure and nanocrosshatch, respectively.

In Figure 6.1, it can clearly observe the transformation from 2D-LIPSS type I to 2D-LIPSS type II just by increasing the spacing (d_s) (or reducing OL and C_v). In Figure 6.1 (a) (at 0.18 J/cm², 8 ps, 5 pulses, d_s=4 µm), we can observe triangular 2D-LIPSS-I similar to the presented one in chapter 1, Figure 1.14. The calculated overlap ratio and coverage were OL $\approx$ 0.53 and $C_v \approx 354$ %, respectively. By increasing the d_s from 4 µm to 6 µm and reducing the number of double-pulses sequences to 3 pulses, the triangular 2D-LIPSS-I were transformed to nanobreath-figure nanostructures (Figure 6.1 (b)), presented previously in chapter 5. The calculated overlap ratio and coverage were OL $\approx$ 0.29 and $C_v \approx 157$ %, respectively. Furthermore, just by increasing the d_s from 6 µm to 8 µm the nanobreath-figure nanostructures were tranformed to nanocrosshatch, presented in Figure 6.1 (c). The calculated overlap ratio and coverage were OL $\approx$ 0.058 and $C_v \approx 89$ %, respectively.

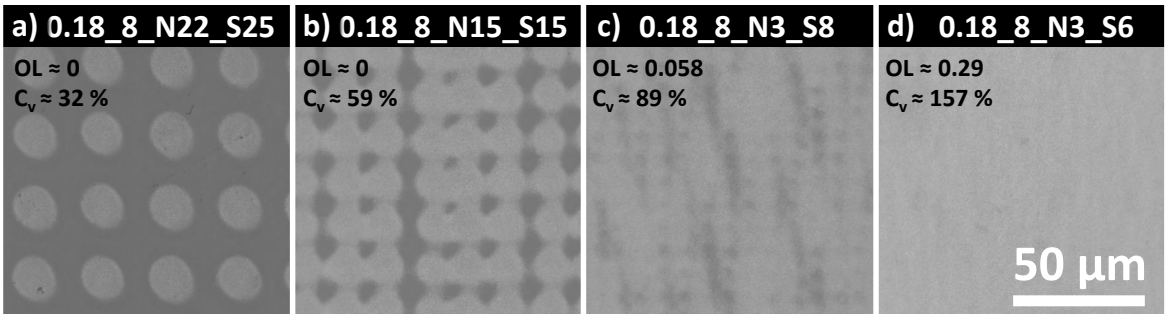

Figure 6.2: Scanning electron microscopy of a Ni (001) sample irradiated at fixed number of double-pulse sequences of 3 p and spacing or scanning overlap of 6 µm, at different laser fluence and time-delay presenting nanopeaks formation. The image titles present the irradiation parameters simultaneously such as: Laser fluence in J/cm², time-delay in ps, number of double-pulses sequences and spacing or steps between scanner impacts in µm.

Furthermore, several irradiations were performed in order to improve and control surface homogeneity on a large scale by interplaying with the number of double-pulse sequences and d_s, as presented in Figure 6.2. The overlap ratio (OL) in Figure 6.2 (a) and (b) is 0 since the impact diameter is smaller than d_s. However, the overlap ratio (OL) is > 0 in Figure 6.2 (c) but the coverage is $C_v \approx 89$ % < 100 %, which means that 11 % of the area are not covered by nanostructures. In Figure 6.2 (d), the overlap ratio (OL) is > 0 and and the coverage is $C_v \approx 157$ % > 100 %, which means that the surface is fully covered by nanobreath-figure nanostructures at these laser conditions and scanning parameters (0.18 J/cm², 8 ps, 3 pulses, d_s=6 µm), and we can visually confirm the surface homogeneity.

Moreover, after obtaining a large homogenous surface of nanobreath-figure, fine adjustments are still required to discover the nanopeaks parameters with the scanner. Several irradiations were tried by smoothly interplaying time-delays and laser fluences, by fixing the scanner parameters previously discussed (number of double-pulse sequences to 3 p and d_s to 6 µm), as presented in Figure 6.3. Based on our previous experience with nanostructures formation and transitions in Chapter 3 (and Figure 5.10), we discovered that nanopeaks can be obtained at lower energy of the nanobreath-figure and with a larger time-delay. Thus, the laser fluence was reduced to 0.17 J/cm² and 0.16 J/cm² which present the formation of nanocrosshatch as expected, at OL $\approx$ 0.2 and $C_v \approx 122$ %, respectively. As previously ob-

served in chapter 3 and Figure 5.10, the nanoscrossatch can be transformed to nanopeaks by increasing the time-delay. Thus, as expected, nanopeaks have appeared by finely increasing the time-delay to 9 ps, OL $\approx$ 0.17 and $C_v \approx 116$ %. As presented in Figure 6.3, the nanopeaks concentration was reduced by increasing the time delay to 9.5 and 10 ps (or finely reducing the OL and C_v, since the impact diameter reduces while increasing the time-delay).

Finally, the nanopeaks nanostructures were observed at OL $\approx$ 0.17 and $C_v \approx 116$ % (0.16 J/cm², 9 ps, 3 pulses, d_s = 6 µm). A nickel sample was homogeneously irradiated with a forest of nanopeaks on a larger surface of 1 mm², within 76 minutes.

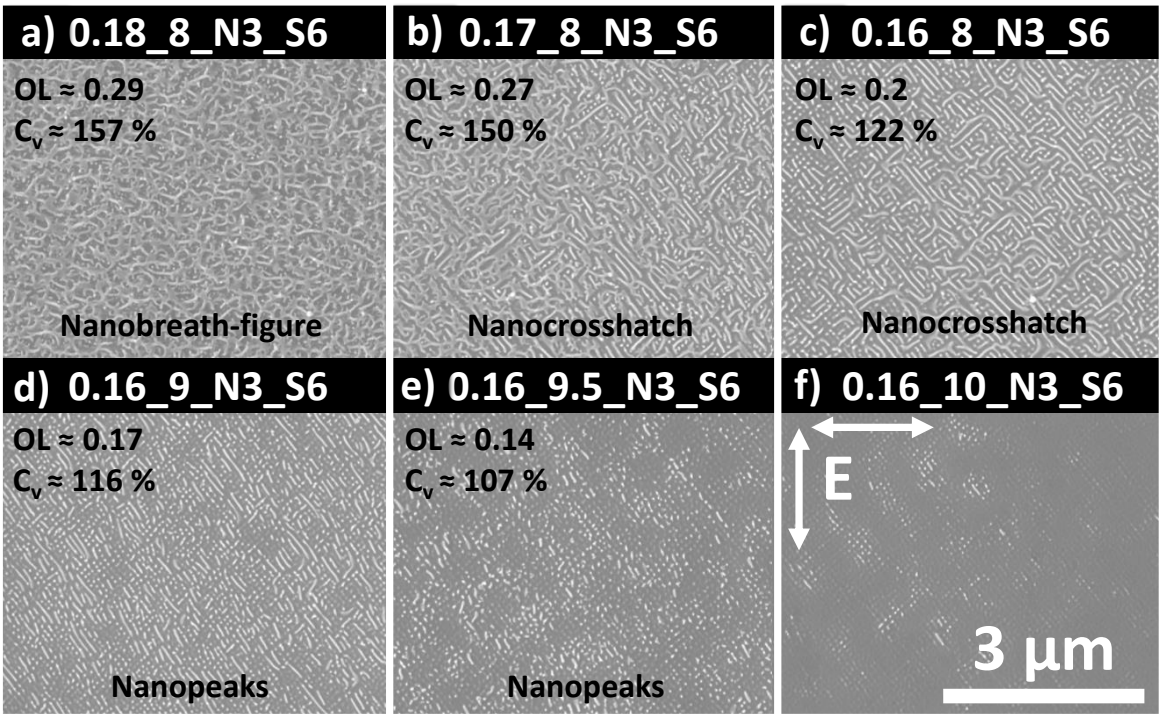

Figure 6.3: Scanning electron microscopy of a Ni (001) sample irradiated at fixed number of double-pulse sequences of 3 p and spacing or scanning overlap of 6 µm, at different laser fluence and time-delay presenting nanopeaks formation. The image titles present the irradiation parameters simultaneously such as: Laser fluence in J/cm², time-delay in ps, number of double-pulses sequences and spacing or steps between scanner impacts in µm.

6.1.2 Wettability tests on polished vs. nanopeaks textured Ni

The non-textured surface part being very small and very deformed, only one drop could be deposited and therefore only one measurement could be made. By depositing a drop of 2.7 µl of ultrapure distilled water, 3 images were recorded: a photo taken by the vertical camera showing the spreading of the drop on the substrate and two photos taken by the camera horizontal, one at the time of deposition and one at the end of the analysis, once the drop has stabilized on the substrate as presented in Figure 6.4.

Since the surface of the substrate was not flat enough, the triple point was often hidden by the substrate during the 360° rotation and therefore the contact angle very difficult to measure. The value of the contact angle recorded as well as the variation in the diameter of the drop are given in Figure 6.5. The evolution of the angle of contact with time means the evolution of the contact angle over 360° every 5° around the drop (we look always the same point by rotating the sample ≈ 5° at a time and systematically measuring the angle of static contact). The curve of the angle is very hilly due to the limited visibility of the triple point, but it shows a variation of the contact angle around an average angle of 80°±4°.

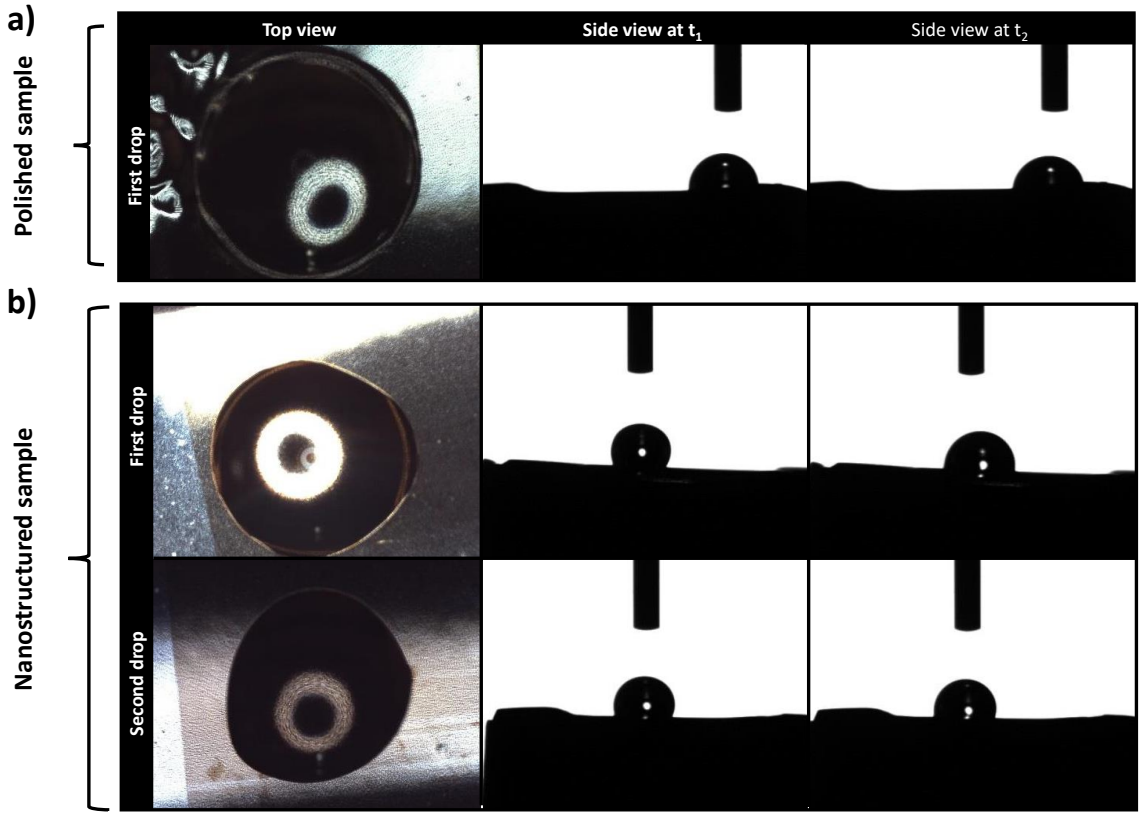

Figure 6.4: (a) Photos of the drop on the raw, mirror-polished Ni substrate. (b) Photos of the first and second drop on the nano-textured Ni substrate. Top view, side view at time of filing and side view at the end of the measurement.

A first drop of 3.15 µl was deposited on the textured substrate. Figure 6.4 shows the photo of the drop in view from above as well as two photos in side view: just after the deposit and at the end of the 360 rotation. The drop sank slightly between the moment of deposit and the end of the measurement, after 360° of rotation, as shown by the curve in Figure 6.5. This can be explained by the progressive impregnation of the drop in the nanoscale structures. The average contact angle is 104°±7°.

The second drop, of ≈ 2.9 µl, shows, in top or side view, a very similar aspect to the first. On the other hand, there is no longer any significant change in contact angle between the deposit and the end of the measurement, the angle of mean contact being 102°±3°.

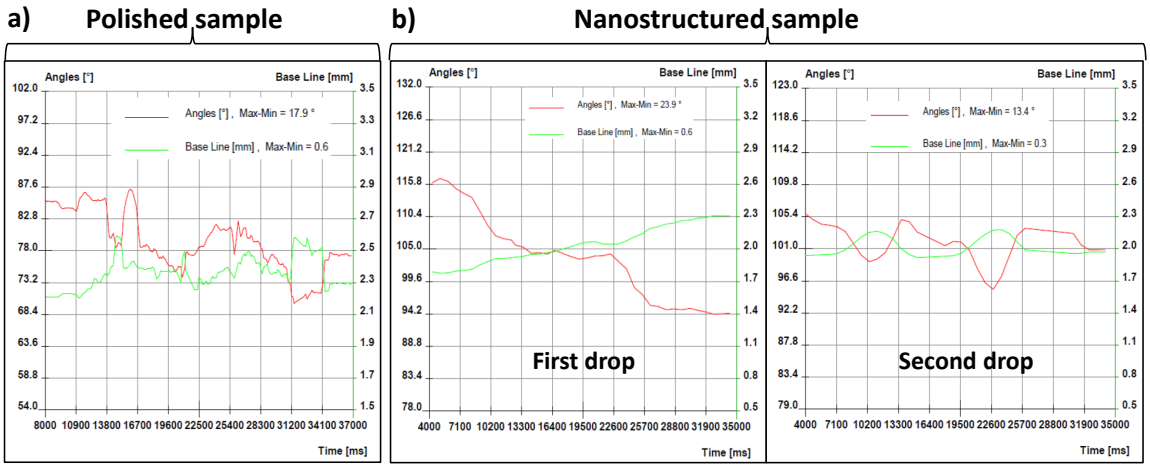

Figure 6.5: (a) Mirror-polished raw Ni. (b) Ni nano-textured – First and second drop: evolution of the contact angle and the diameter of the drop over time (rotation of the sample holder over 360°.)

A slight spreading anisotropy, which results in a decrease in the contact angle and an increase in the diameter of the drop in a given direction, is measured. This slight spreading anisotropy, probably induced by the nanostructure, is also present on the curve of the first drop, as presented in Figure 6.6.

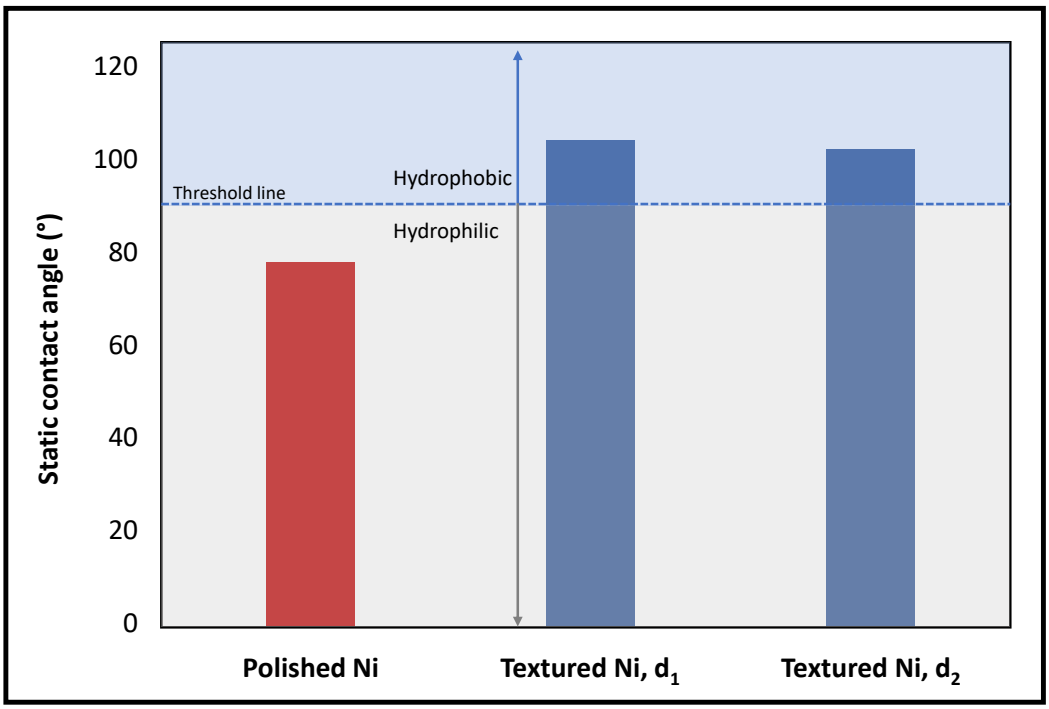

Figure 6.6: The average contact angles and the associated Pearson standard deviations measured on the Ni(001) substrate before and after the laser pass.

6.1.3 Antibacterial test of nanopeaks textured Ni

The same Ni sample tested by physico-chemical analysis, has been evaluated here for antibacterial adhesive properties. The sample was textured with high aspect nanopeaks structures as presented in Figure 6.7 (a), and was sent for a simple examination.

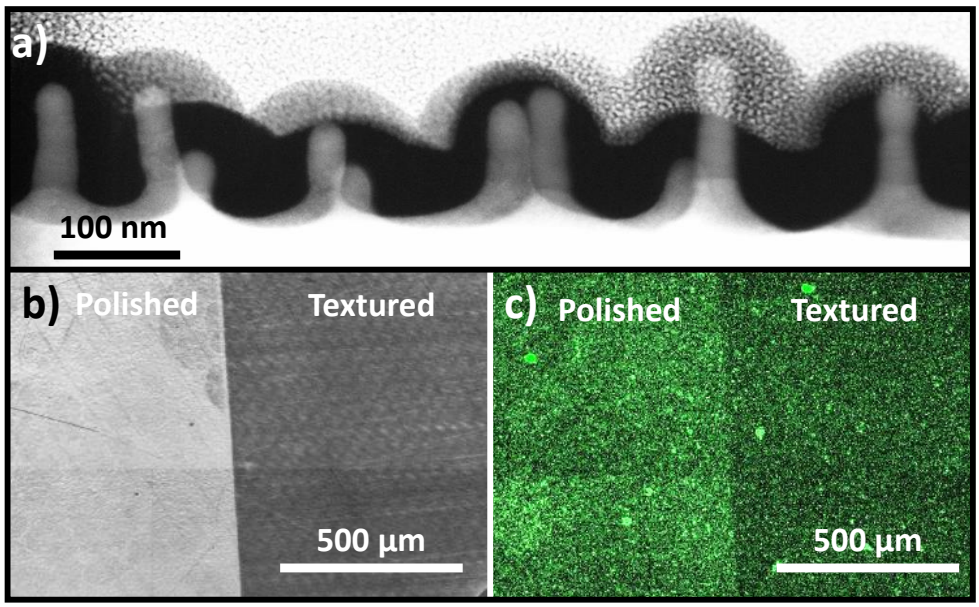

Figure 6.7: Antibacterial test performed on structured Ni by nanopeaks, compared with a polished surface. (a) High aspect ratio nanopeaks of the textured surface presented in (b) on microscale, characterized by optical microscopy. (c) Fluorescence measurements present a promising change or reduction in bacterial adhesion of the textured surface.

The fluorescence measurements (Figure 6.7 (c)) of the textured sample with a forest of nanopeaks show a promising change or reduction in bacterial adhesion of the textured surface. Thus, this simple results open the doors for other further investigations in the biological field.

6.2 Antibacterial test of textured Ti

In this section, a titanium material was irradiated with the goal of testing antibacterial adhesive properties. The titanium was chosen because it is more relevant to biologists' interests. Prior to laser irradiation, titanium samples were mechanically polished using the "automatic polishing procedure" described in Chapter 2, Table 2.2. We began polishing with a "coarse" paper, P240, and progressed to finer grain papers, P320, P600, P1200, and P4000. We cleaned the samples between two polishing papers in an ultrasonic bath for a few minutes to remove any particles from the previous paper that may have become embedded. Following the coarse papers, we polished with diamonds of 6 µm, 3 µm, and 1 µm before finishing with Colloidal silica mixed with 3% H_2O_2 and 3%NH_4OH to obtain a mirror initial surface with a R_a < 5nm.

6.2.1 Ti texturation on a larger surface

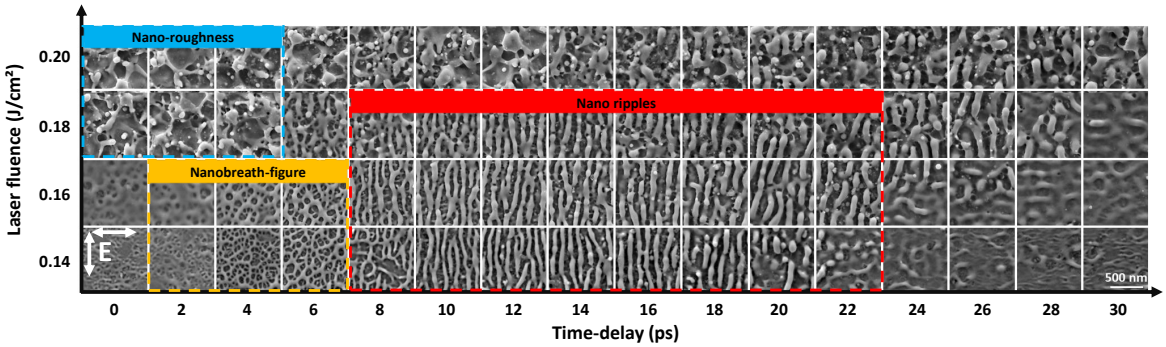

Figure 6.8: Scanning electron microscopy of a Ti sample irradiated by 25 number of double-pulses sequences at an incident laser fluence range from 0.14 to 0.20 J/cm² with time-delay range from 0 ps $\leq \Delta t \leq$ 30 ps between the two crossed polarizations. The nanostructures domains are presented in different colored regions such as: blue for nanoroughness, orange for nanobreath-figure, and red for nanoripples. The laser polarization E is indicated by the white arrow

Consequently, double pulse experiments were performed to discover the created nanostructures by using the same nickel irradiation parameters using a cross polarization strategy, setting a depolarization angle of α = 90 and a range of time delays between 0 and 30 ps as presented in Figure 6.8. The pulse duration was fixed to 150 fs and the number of double pulse sequences to 25. Figure 6.8 depicts various nanostructured regimes. Nanoroughnesses, nanobreath-figures, and nano-ripples are the three main regimes. Additional experiments were carried out in order to create two distinct types of structures known as nanobumps and micro-pillars, which will be discussed in the following sections.

6.2.2 Bacterial adhesion tests on polished vs. textured Ti

.

The nanobreath-figure are previously identified on Ni in Chapter 5, Figure 5.10, at $\Delta t \approx$ 0 ps and for a laser fluence between 0.20 and 0.22 J/cm². They have an unorganized cavity shape with dimensions at the nanoscale. They were also observed in Ti at small time-delay between 2 ps $\leq \Delta t \leq$ 6 ps, but at lower laser fluences between 0.14 and 0.16 J/cm². The nanobreath-figure height was characterized on AFM, the minimum and maximum height is between -37.3 and 36.8 nm, respectively. The sample was irradiated on a larger area of few mm² without scanner, by creating impact-to-impact array, moving the motorized sample support with a fixed spacing of 14 µm. The spacing is determined after trying several spacing between 10 and 20 µm. In this case we did not obtain the same homogeneity and speed compared to scanner texturation, but further experimental setups are in progress for several future works. Fluorescence measurements in Figure 6.9 (a) show that there is a 10 % reduction in bacterial adhesion on the surface with nanobreath-figure compared to polished surface (p value < 0.05 not statistically significant).

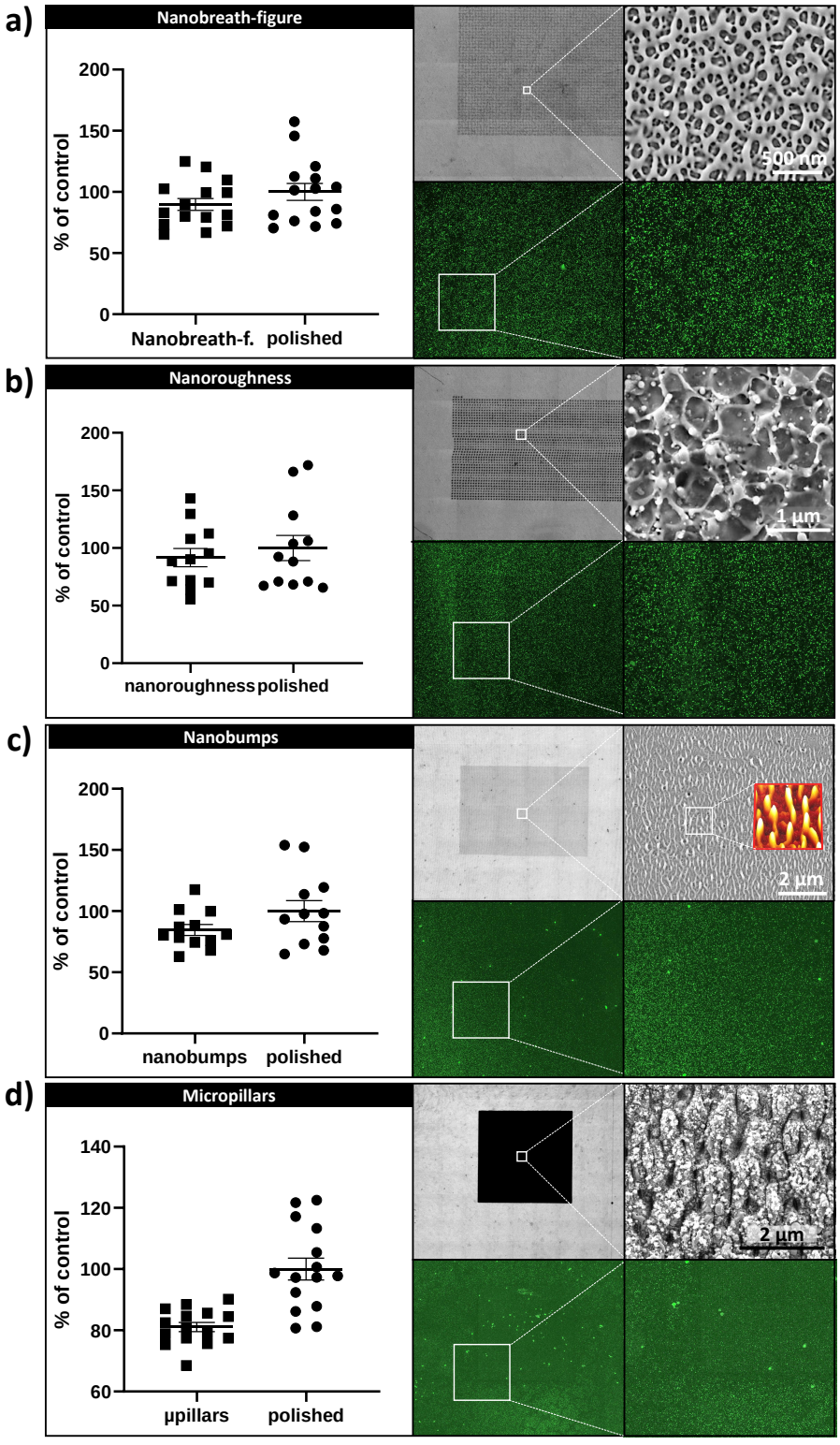

Figure 6.9: Antibacterial test performed on structured Ti by nanobreath-figure, nanoroughness, nanbumps and micropillars, compared with a polished surface.

Nanoroughness structures were observed in Figure 6.8 on Ti by increasing the laser fluence to 0.18 J/cm² and 0.20 J/cm² at a small time-delay between 0 ps $\leq \Delta t \leq$ 4 ps. These

nanoroughnes or chaotic nanostrucutres were also observed on Ni at similar time-delay but higher laser fluence of 0.23 J/cm² and 0.24 J/cm², as presented previously in Chapter 5. Nanoroughness height was characterized on AFM, the minimum and maximum height is between -161 nm and 163 nm, respectively. The sample was irradiated on a larger area of few mm² without scanner, by creating impact-to-impact array, moving the motorized sample support with a fixed spacing of 15 µm. Fluorescence measurements in Figure 6.9 (b) show that there is a 7 % reduction in bacterial adhesion on the surface with nanoroughness compared to polished surface (p value < 0.05 not statistically significant).

However, nanobumps structures were not immediately observed by the previous experiments presented in Figure 6.8, but some cavities with potential bumps formation were observed at 0.14 J/cm² and Δt = 24 ps. Thus, we fixed the laser fluence and time-delay at at 0.14 J/cm² and Δt = 24 ps and we increased the number of double pulses sequences to 50. Therefore, ripples nanostructures were observed with nanobumps as presented in Figure 6.10 (c). The nanobumps shape were similar to the ones observed in chapter 3 but with lower aspect-ratio. The height was characterized on AFM, the minimum and maximum height is between -38.5 nm and 41.9 nm, respectively. The sample was irradiated on a larger area of few mm² without scanner, by creating impact-to-impact array, moving the motorized sample support with a fixed spacing of 12 µm. Fluorescence measurements in Figure 6.9 (c) show that there is a 13 % reduction in bacterial adhesion on the surface with nanobumps compared to polished surface (p value < 0.05 not statistically significant).

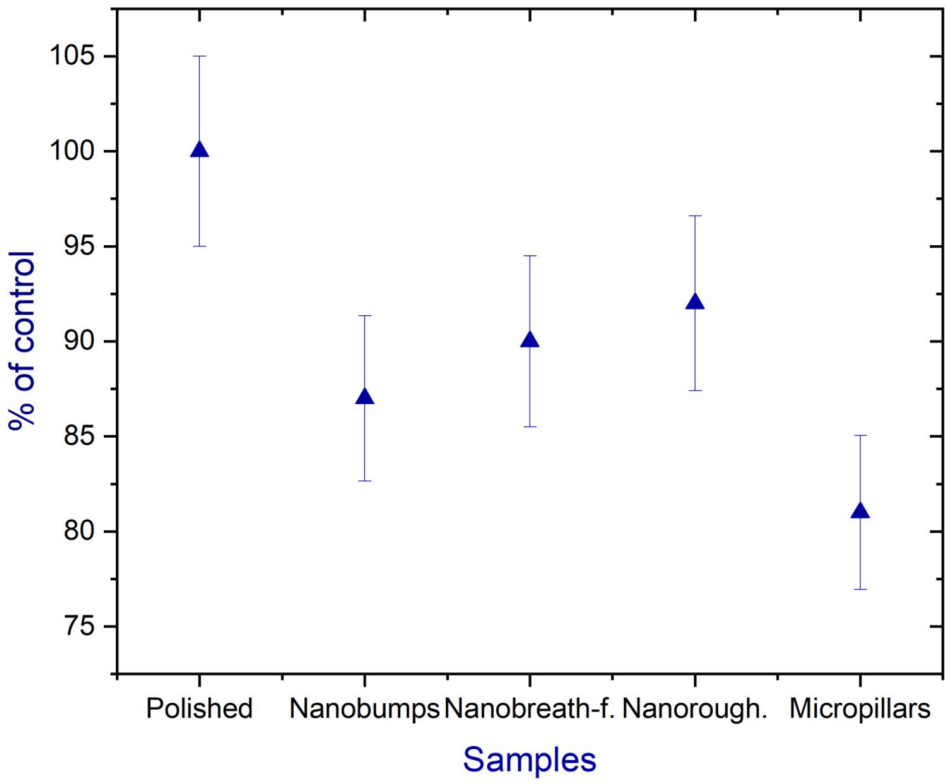

Figure 6.10: Comparison of bacterial adhesion tests on polished vs. textured Ti

Furthermore, micropillars structures were produced by increasing the laser fluence to

0.25 J/cm² and the number of double pulses sequences to 50. In the optical microscopy image, we observe a dark contrast could be formed by surface oxidation due to high laser dose. The sample was also irradiated on a larger area of few mm² without scanner, by creating impact-to-impact array, moving the motorized sample support with a fixed spacing of 12 µm. Fluorescence measurements in Figure 6.9 (d) show that there is a 20 % reduction in bacterial adhesion on the surface with micropillars compared to polished surface (p value < 0.0001 not statistically significant).

Figure 6.10 present a comparison of % of control between the polished and all the textured Ti samples. We can observe that in the textured samples, the % of control has reduced to 7%, 10% and 13% for nanoroughness, nanobreath-figure and nanobumps structures. However, the % of control was reduced by 20% for the micropillars. This study opens the doors for more investigations in the domain of antibacterial nanostructures.

6.3 Conclusion

Nanometric surface texturing by femtosecond laser slightly influences wetting. She allowed to increase the contact angle by ≈ 20°, the Ni substrate (001) changing from a hydrophilic behavior (angle of contact <90°) before laser irradiation to hydrophobic behavior (contact angle > 90°) after nanostructuring. The pattern created on the surface also seems to induce a slight spreading anisotropy. Figure 6.6 brings together the values of the contact angles for the polished and textured surface. Fluorescence measurements or textured Ti surfaces show that there is a promising reduction in bacterial adhesion on the surface compared to polished surfaces, which opens the door to several future works.

General conclusion and future work

Irradiation of materials by ultrashort laser pulses triggers anisotropically structured arrangement of matter on the nanoscale, the laser-induced periodic surface structures (LIPSS), or 'ripples'. This thesis demonstrates the potential of ultrafast laser for the fabrication of unconventional patterns (uniform periodic nanopatterns with a sub-100 nm periodicity). In an elegant way, the control of fluid flows on the nanoscale by laser irradiation is demonstrated by tuning laser parameters.

In chapter 3, a large variety of nanostructuring regimes are reported by controlling the laser fluence and time-delay. These irradiations have allowed us to reach the following conclusions:

- Laser parameters as peak fluence, time delay, and number of double-pulses sequences play a significant role on modifying surface morphology and topography.
- The formation of nanopeaks, nanobumps, nanohumps and nanocavities patterns with 20-80 nm transverse size unit and up to 100 nm height are reported.
- We showed that the use of crossed-polarized double laser pulse adds an extra dimension to nanostructuring process as laser energy dose and multi-pulse feedback tune the energy gradients distribution, crossing critical values for surface self-organization regimes.
- We revealed that initial surface roughness and the type of roughness both play a crucial role in controlling the transient emergence of nanostructures during laser irradiation.

Chapter 4 reveals the uniform formation of unconventional self-organized patterns on the 100 nm scale generated by focused ultrafast light. Irradiated surface turns to a forest of nanopeaks with the highest aspect ratio reported in the literature at the nanoscale (height 100 nm: width 20 nm with a sub-100 nm periodicity). In this chapter, we concluded that:

- By pointing out the proposed nanostructuring strategy, relying on a timely-controlled polarization feedback, opens the route for producing uniform high-aspect ratio structures for nanoengineering metamaterials.
- Pseudo-3D scanning electron microscopy and high-resolution atomic force microscopy images present the pulse-to-pulse dynamics of the nanopeaks formation by displaying the transformation from convection cells to ridges, nanopeaks, nanostripes and chaos.
- The periodicty of nanopeak and concentration can be controlled by pulse duration, which will definitely make them compatible with several types of applications. This suggests that the mechanical momentum defined by pulse duration plays a crucial role in controlling the aspect ratio, the periodicity as well as the concentration of the formed nanopeaks.

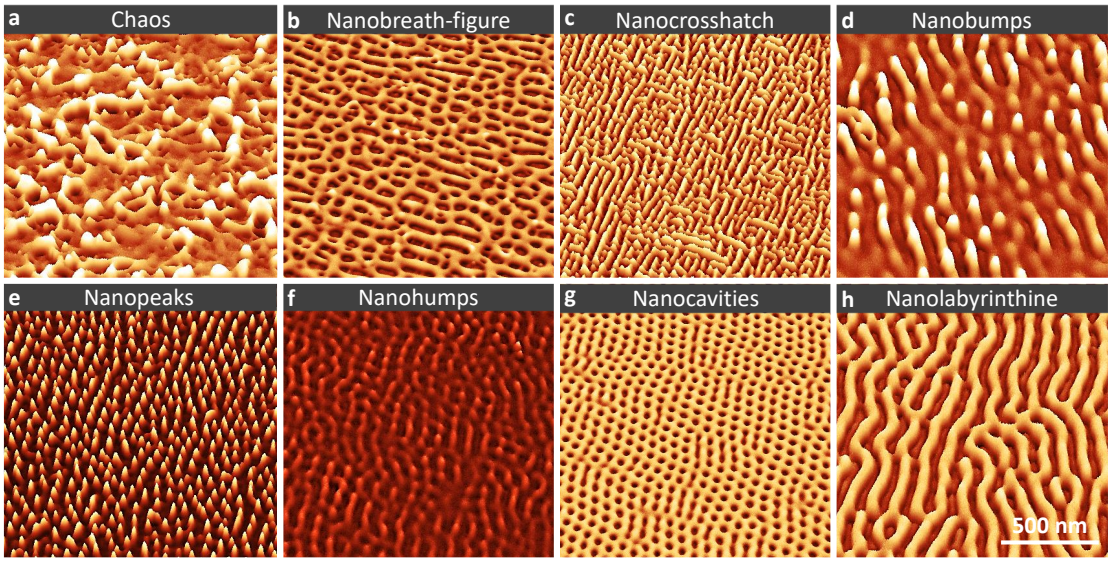

Figure 6.11: a-h) Pseudo 3D scanning electron microscopy of nanostructures chaos (a), nanobreath-figure (b), nanocrosshatch (c), nanobumps (d), nanopeaks (e), nanohumps (f), nanocavities (g) and nanolabyrinthine (h).

In chapter 5, electromagnetic coupled with hydrodynamic simulations were performed to reveal why this unique optical manipulation allows peaks generation by inhomogeneous local absorption sustained by nanoscale convection. Moreover, we used non-linear dynamics and physics-guided machine learning, an emerging field of research that combines physical knowledge and machine learning to predict novel patterns by integrating partial physical knowledge in the form of the Swift-Hohenberg partial equation. In this chapter we concluded that:

- Electromagnetic coupled with hydrodynamic simulations were performed to reveal why the unique optical manipulation allows nanopeaks generation by inhomogeneous local absorption sustained by nanoscale convection.
- The growth of the laser-induced structures from quasi-hexagonal cavities to uniform nanopeaks is analyzed by combined electromagnetic and hydrodynamic approaches.
- Non-linear dynamics and physics-guided machine learning were used, an emerging field of research that combines physical knowledge and machine learning to predict novel patterns by integrating partial physical knowledge in the form of the Swift-Hohenberg partial equation.
- The model is able to identify laser parameter regions of interest for applications and, since CNN features are not learned on observed patterns, can even be used for novel pattern prediction.
- In total, eight different nanostructures were observed and presented in Figure 6.11 on irradiated Ni such as: chaos (a), nanobreath-figure (b), nanocrosshatch (c), nanobumps (d), nanopeaks (e), nanohumps (f), nanocavities (g) and nanolabyrinthine (h).

- Self-organization observation by Entropy interpretation open the door to describe mathematically the nonlinear dynamics of laser-induced surfaces with models able to reproduce the variability of the patterns in the phase space and explore the origin of bifurcations.
- This carried work opens a new experimental path to generate unconventional structures with extreme periodicities on different materials, opening up new possibilities for ultrafast laser processing functionalization of metals.

In this chapter 6, we present the evaluation of microscopic and macroscopic properties of irradiated materials. Physico-chemical analysis of textured Ni sample were performed at MANUTECH facility, the preliminary results show a slight improvement in surface hydrophobia. Furthermore, nanostructures Ti samples show a good potential in manufacturing antibacterial surfaces, which opens the door for several studies in this domain. In this chapter we conclude that:

- Nanometric surface texturing by femtosecond laser influences surface wetting properties.
- Physico-chemical analysis of textured Ni demonstrate that nanopeaks has transformed the surface from hydrophilic to hydrophobic.
- Fluorescence measurements of the textured sample with a forest of nanopeaks show a promising change in bacterial adhesion of the textured surface. Now the door is open for further investigations in the biological field.
- Fluorescence measurements or textured Ti surfaces show that there is a promising reduction in bacterial adhesion on the surface compared to polished surfaces.

Scientific productions

Publications

- Nakhoul, A., Maurice, C., Agoyan, M., Rudenko, A., Garrelie, F., Pigeon, F., & Colombier, J.-P. (2021). Self-Organization Regimes Induced by Ultrafast Laser on Surfaces in the Tens of Nanometer Scales. Nanomaterials, 11(4), 1020. doi: 10.3390/nano11041020
- Nakhoul, A., Rudenko, A., Sedao, X., Peillon, N., Colombier, J. P., Maurice, C., Blanc, G., Borbèly A., Faure, N., Kermouche, G. (2021). Energy feedthrough and microstructure evolution during direct laser peening of aluminum in femtosecond and picosecond regimes. J. Appl. Phys., 130(1), 015104. doi: 10.1063/5.0052510
- Nakhoul, A., Rudenko, A., Maurice, C., Reynaud, S., Garrelie, F., Pigeon, F., & Colombier, J.-P. (2022). Boosted Spontaneous Formation of High-Aspect Ratio Nanopeaks on Ultrafast Laser-Irradiated Ni Surface. Adv. Sci., 9(21), 2200761. doi: 10.1002/advs.202200761
- Brandao, E., Colombier, J.-P., Duffner, S., Emonet, R., Garrelie, F., Habrard, A., Jacquenet, F., Nakhoul, A., Sebban, M. (2022). Learning PDE to Model Self-Organization of Matter. Entropy, 24(8), 1096. doi: 10.3390/e24081096
- Nakhoul, A., Maurice, C., Faure, N., Garrelie, F., Pigeon, F., & Colombier, J.-P. (2022). Tailoring the surface morphology of Ni at the nanometric scale by ultrashort laser pulses. Appl. Phys. A, 128(10), pp 1–7, 1432-0630. doi: 10.1007/s00339-022-06046-2

International Conferences

- SPIE. PHOTONIC WEST 2022 : Oral Presentation- Laser Applications in Microelectronic and Optoelectronic Manufacturing (LAMOM): Surface morphologies at nanometric scale by temporal and polarization control of ultrashort laser pulses. Nakhoul, A., Maurice, C., Reynaud, S., Garrelie, F., Pigeon, F., & Colombier, J.-P.
- COLA 2021/2022 : Poster Presentation: Surface Morphology at Nanometric Scale by Temporal and Polarization Control of Ultrashort Laser Pulses. Nakhoul, A., Maurice, C., Reynaud, S., Garrelie, F., Pigeon, F., & Colombier, J.-P.

Bibliography

[1] S. Echeverría-Alar and M. G. Clerc. "Labyrinthine patterns transitions". In: *Phys. Rev. Res.* 2 (4 2020), p. 042036. DOI: 10.1103/PhysRevResearch.2.042036. URL: https://link.aps.org/doi/10.1103/PhysRevResearch.2.042036.

[2] Xxx Sedao et al. "Influence of crystal orientation on the formation of femtosecond laser-induced periodic surface structures and lattice defects accumulation". In: *Applied Physics Letters* 104.17 (2014), p. 171605. DOI: 10.1063/1.4874626. URL: https://doi.org/10.1063/1.4874626.

[3] Anthony Abou Saleh et al. "Nanoscale imaging of ultrafast light coupling to self-organized nanostructures". In: *ACS photonics* 6.9 (2019), pp. 2287–2294.

[4] J. Bonse et al. "Femtosecond laser-induced periodic surface structures". In: *J. Laser Appl.* 24.4 (2012), p. 042006. ISSN: 1042-346X. DOI: 10.2351/1.4712658.

[5] Zhipeng Wu et al. "Recent advances in femtosecond laser-structured Janus membranes with asymmetric surface wettability". In: *Nanoscale* 13.4 (Feb. 2021), pp. 2209–2226. ISSN: 2040-3364. DOI: 10.1039/D0NR06639G.

[6] Jörn Bonse. "Quo Vadis LIPSS?—Recent and Future Trends on Laser-Induced Periodic Surface Structures". In: *Nanomaterials* 10.10 (2020), p. 1950. ISSN: 2079-4991. DOI: 10.3390/nano10101950.

[7] Vassilia Zorba et al. "Biomimetic Artificial Surfaces Quantitatively Reproduce the Water Repellency of a Lotus Leaf". In: *Adv. Mater.* 20.21 (2008), pp. 4049–4054. ISSN: 0935-9648. DOI: 10.1002/adma.200800651.

[8] Aaron Elbourne, Russell J. Crawford, and Elena P. Ivanova. "Nano-structured antimicrobial surfaces: From nature to synthetic analogues". In: *J. Colloid Interface Sci.* 508 (2017), pp. 603–616. ISSN: 0021-9797. DOI: 10.1016/j.jcis.2017.07.021.

[9] A. Y. Vorobyev and Chunlei Guo. "Colorizing metals with femtosecond laser pulses". In: *Appl. Phys. Lett.* 92.4 (2008), p. 041914. ISSN: 0003-6951. DOI: 10.1063/1.2834902.

[10] J. Bonse et al. "Tribological performance of femtosecond laser-induced periodic surface structures on titanium and a high toughness bearing steel". In: *Appl. Surf. Sci.* 336 (2015), pp. 21–27. ISSN: 0169-4332. DOI: 10.1016/j.apsusc.2014.08.111.

[11] Anton Rudenko et al. "Self-organization of surfaces on the nanoscale by topography-mediated selection of quasi-cylindrical and plasmonic waves". In: *Nanophotonics* 8.3 (2019), pp. 459–465.

[12] Hao Zhang et al. “Coherence in ultrafast laser-induced periodic surface structures”. In: *Phys. Rev. B* 92.17 (2015), p. 174109. ISSN: 2469-9969. DOI: 10.1103/PhysRevB.92.174109.

[13] Anton Rudenko et al. “Spontaneous periodic ordering on the surface and in the bulk of dielectrics irradiated by ultrafast laser: a shared electromagnetic origin - Scientific Reports”. In: *Sci. Rep.* 7.12306 (2017), pp. 1–14. ISSN: 2045-2322. DOI: 10.1038/s41598-017-12502-4.

[14] J. Z. P. Skolski et al. “Laser-induced periodic surface structures: Fingerprints of light localization”. In: *Phys. Rev. B* 85.7 (2012), p. 075320. ISSN: 2469-9969. DOI: 10.1103/PhysRevB.85.075320.

[15] A. Rudenko et al. “Light absorption by surface nanoholes and nanobumps”. In: *Appl. Surf. Sci.* 470 (2019), pp. 228–233. ISSN: 0169-4332. DOI: 10.1016/j.apsusc.2018.11.111.

[16] Xxx Sedao et al. “Self-Arranged Periodic Nanovoids by Ultrafast Laser-Induced Near-Field Enhancement”. In: *ACS Photonics* 5.4 (2018), pp. 1418–1426. DOI: 10.1021/acsphotonics.7b01438.

[17] A. Rudenko et al. “High-frequency periodic patterns driven by non-radiative fields coupled with Marangoni convection instabilities on laser-excited metal surfaces”. In: *Acta Mater.* 194 (2020), pp. 93–105. ISSN: 1359-6454. DOI: 10.1016/j.actamat.2020.04.058.

[18] A Abou-Saleh et al. “Spallation-induced roughness promoting high spatial frequency nanostructure formation on Cr”. In: *Applied Physics A* 124.4 (2018), pp. 1–12.

[19] Sohail A. Jalil et al. “Formation of controllable 1D and 2D periodic surface structures on cobalt by femtosecond double pulse laser irradiation”. In: *Appl. Phys. Lett.* 115.3 (July 2019), p. 031601. ISSN: 0003-6951. DOI: 10.1063/1.5103216.

[20] Fotis Fraggelakis et al. “Controlling 2D laser nano structuring over large area with double femtosecond pulses”. In: *Appl. Surf. Sci.* 470 (2019), pp. 677–686. ISSN: 0169-4332. DOI: 10.1016/j.apsusc.2018.11.106.

[21] Anthony Abou Saleh et al. “Sub-100 nm 2D nanopatterning on a large scale by ultrafast laser energy regulation”. In: *Nanoscale* 12.12 (2020), pp. 6609–6616. ISSN: 2040-3364. DOI: 10.1039/C9NR09625F.

[22] Anthony Nakhoul et al. “Self-Organization Regimes Induced by Ultrafast Laser on Surfaces in the Tens of Nanometer Scales”. In: *Nanomaterials* 11.4 (2021), p. 1020.

[23] P. Laporte, F. Salin, and S. Mottin. *Systèmes femtosecondes*. Saint-Etienne, France: Publications de l’Université de Saint-Etienne, 2001. ISBN: 978-2-86272210-8.

[24] Donna Strickland and Gerard Mourou. “Compression of amplified chirped optical pulses”. In: *Opt. Commun.* 56.3 (Dec. 1985), pp. 219–221. ISSN: 0030-4018. DOI: 10.1016/0030-4018(85)90120-8.

[25] Paul Hervier. *Fonctionnalisation de surface de verres métalliques base Zirconium.* Grenoble, France: Université Grenoble Alpes (ComUE), Nov. 2017. URL: https://www.theses.fr/2017GREAI088.

[26] Vanessa Belaud. *Structuration de surfaces au moyen d'un traitement laser femtoseconde : applications à la fonctionnalisation de surface du polypropylène en vue de sa métallisation.* Ecully, Ecole centrale de Lyon, Jan. 2014. URL: https://www.theses.fr/2014ECDL0003.

[27] François Hache. "Chapitre 5 Effet Kerr optique". In: *Optique non linéaire.* EDP Sciences, July 2016, pp. 71–90. ISBN: 978-2-75982007-8. DOI: 10.1051/978-2-7598-2007-8.c008.

[28] F. Garrelie et al. "Evidence of surface plasmon resonance in ultrafast laser-induced ripples". In: *Opt. Express* 19.10 (May 2011), pp. 9035–9043. ISSN: 1094-4087. DOI: 10.1364/OE.19.009035.

[29] J. P. Colombier et al. "Effects of electron-phonon coupling and electron diffusion on ripples growth on ultrafast-laser-irradiated metals". In: *J. Appl. Phys.* 111.2 (Jan. 2012), p. 024902. ISSN: 0021-8979. DOI: 10.1063/1.3676221.

[30] A. Nakhoul et al. "Energy feedthrough and microstructure evolution during direct laser peening of aluminum in femtosecond and picosecond regimes". In: *J. Appl. Phys.* 130.1 (July 2021), p. 015104. ISSN: 0021-8979. DOI: 10.1063/5.0052510.

[31] B. Dusser et al. "Controlled nanostructrures formation by ultra fast laser pulses for color marking". In: *Opt. Express* 18.3 (Feb. 2010), pp. 2913–2924. ISSN: 1094-4087. DOI: 10.1364/OE.18.002913.

[32] E. Bévillon et al. "Ultrafast Surface Plasmonic Switch in Non-Plasmonic Metals". In: *arXiv* (Sept. 2015). DOI: 10.1103/PhysRevB.93.165416. eprint: 1509.03182.

[33] Jijil J. J. Nivas et al. "Direct Femtosecond Laser Surface Structuring with Optical Vortex Beams Generated by a q-plate". In: *Sci. Rep.* 5.17929 (Dec. 2015), pp. 1–12. ISSN: 2045-2322. DOI: 10.1038/srep17929.

[34] Anthony Nakhoul et al. "Boosted Spontaneous Formation of High-Aspect Ratio Nanopeaks on Ultrafast Laser-Irradiated Ni Surface". In: *Adv. Sci.* 9.21 (July 2022), p. 2200761. ISSN: 2198-3844. DOI: 10.1002/advs.202200761.

[35] Leonid V. Zhigilei, Prasad B. S. Kodali, and Barbara J. Garrison. "Molecular Dynamics Model for Laser Ablation and Desorption of Organic Solids". In: *J. Phys. Chem. B* 101.11 (Mar. 1997), pp. 2028–2037. ISSN: 1520-6106. DOI: 10.1021/jp9634013.

[36] E. G. Gamaly. "The physics of ultra-short laser interaction with solids at non-relativistic intensities". In: *Phys. Rep.* 508.4 (Nov. 2011), pp. 91–243. ISSN: 0370-1573. DOI: 10.1016/j.physrep.2011.07.002.

[37] E. Bévillon, R. Stoian, and J. P. Colombier. "Nonequilibrium optical properties of transition metals upon ultrafast electron heating". In: *J. Phys.: Condens. Matter* 30.38 (2018), p. 385401. ISSN: 0953-8984. DOI: 10.1088/1361-648x/aad8e5.

[38] Maxim V. Shugaev et al. "Laser-Induced Thermal Processes: Heat Transfer, Generation of Stresses, Melting and Solidification, Vaporization, and Phase Explosion". In: *Handbook of Laser Micro- and Nano-Engineering*. Cham, Switzerland: Springer, Nov. 2021, pp. 83–163. DOI: 10.1007/978-3-030-63647-0_11.

[39] S. I. Anisimov, B. L. Kapeliovich, and T. L. Perel'Man. "Electron emission from metal surfaces exposed to ultrashort laser pulses". In: *Soviet Journal of Experimental and Theoretical Physics* 39 (Aug. 1974), pp. 375–377. ISSN: 1063-7761. URL: https://ui.adsabs.harvard.edu/abs/1974JETP...39..375A/abstract.

[40] B. N. Chichkov et al. "Femtosecond, picosecond and nanosecond laser ablation of solids". In: *Appl. Phys. A* 63.2 (Aug. 1996), pp. 109–115. ISSN: 1432-0630. DOI: 10.1007/BF01567637.

[41] Xxx Sedao et al. "Electron backscatter diffraction characterization of laser-induced periodic surface structures on nickel surface". In: *Appl. Surf. Sci.* 302 (May 2014), pp. 114–117. ISSN: 0169-4332. DOI: 10.1016/j.apsusc.2013.10.152.

[42] Chengping Wu et al. "Generation of subsurface voids and a nanocrystalline surface layer in femtosecond laser irradiation of a single-crystal Ag target". In: *Phys. Rev. B* 91.3 (Jan. 2015), p. 035413. ISSN: 2469-9969. DOI: 10.1103/PhysRevB.91.035413.

[43] Brian J. Demaske et al. "Ablation and spallation of gold films irradiated by ultrashort laser pulses". In: *Phys. Rev. B* 82.6 (Aug. 2010), p. 064113. ISSN: 2469-9969. DOI: 10.1103/PhysRevB.82.064113.

[44] N. A. Inogamov et al. "Hydrodynamics driven by ultrashort laser pulse: simulations and the optical pump—X-ray probe experiment". In: *Appl. Phys. B: Lasers Opt.* 119.3 (June 2015), pp. 413–419. ISSN: 0946-2171. DOI: 10.1007/s00340-015-6039-7.

[45] V. V. Zhakhovskii, N. A. Inogamov, and K. Nishihara. "New mechanism of the formation of the nanorelief on a surface irradiated by a femtosecond laser pulse". In: *JETP Lett.* 87.8 (June 2008), pp. 423–427. ISSN: 1090-6487. DOI: 10.1134/S0021364008080079.

[46] Jean-Philippe Colombier et al. "Hydrodynamic simulations of metal ablation by femtosecond laser irradiation". In: *Physical Review B: Condensed Matter and Materials Physics (1998-2015)* 71 (Apr. 2005), p. 165406. URL: https://hal.archives-ouvertes.fr/hal-00121833.

[47] N. Georgiev, A. Pavlovska, and E. Bauer. "Surface disordering without surface roughening". In: *Phys. Rev. B* 52.4 (July 1995), pp. 2878–2888. ISSN: 0163-1829. DOI: 10.1103/physrevb.52.2878. eprint: 9981359.

[48] A. Borowiec and H. K. Haugen. "Subwavelength ripple formation on the surfaces of compound semiconductors irradiated with femtosecond laser pulses". In: *Appl. Phys. Lett.* 82.25 (June 2003), pp. 4462–4464. ISSN: 0003-6951. DOI: 10.1063/1.1586457.

[49] Jörn Bonse et al. "Femtosecond Laser Texturing of Surfaces for Tribological Applications". In: *Materials* 11.5 (May 2018), p. 801. ISSN: 1996-1944. DOI: 10.3390/ma11050801.

[50] E. V. Golosov et al. "Ultrafast changes in the optical properties of a titanium surface and femtosecond laser writing of one-dimensional quasi-periodic nanogratings of its relief". In: *J. Exp. Theor. Phys.* 113.1 (July 2011), pp. 14–26. ISSN: 1090-6509. DOI: 10.1134/S1063776111050025.

[51] Shazia Bashir, M. Shahid Rafique, and Wolfgang Husinsky. "Femtosecond laser-induced subwavelength ripples on Al, Si, CaF2 and CR-39". In: *Nucl. Instrum. Methods Phys. Res., Sect. B* 275 (Mar. 2012), pp. 1–6. ISSN: 0168-583X. DOI: 10.1016/j.nimb.2011.12.016.

[52] A. Y. Vorobyev, V. S. Makin, and Chunlei Guo. "Periodic ordering of random surface nanostructures induced by femtosecond laser pulses on metals". In: *J. Appl. Phys.* 101.3 (Feb. 2007), p. 034903. ISSN: 0021-8979. DOI: 10.1063/1.2432288.

[53] Min Huang et al. "The morphological and optical characteristics of femtosecond laser-induced large-area micro/nanostructures on GaAs, Si, and brass". In: *Opt. Express* 18.104 (Nov. 2010), A600–A619. ISSN: 1094-4087. DOI: 10.1364/OE.18.00A600.

[54] Matteo Mastellone et al. "Deep-Subwavelength 2D Periodic Surface Nanostructures on Diamond by Double-Pulse Femtosecond Laser Irradiation". In: *Nano Lett.* 21.10 (May 2021), pp. 4477–4483. ISSN: 1530-6984. DOI: 10.1021/acs.nanolett.1c01310.

[55] Shuji Sakabe et al. "Mechanism for self-formation of periodic grating structures on a metal surface by a femtosecond laser pulse". In: *Phys. Rev. B* 79.3 (Jan. 2009), p. 033409. ISSN: 2469-9969. DOI: 10.1103/PhysRevB.79.033409.

[56] Catalina Albu et al. "Periodical structures induced by femtosecond laser on metals in air and liquid environments". In: *Appl. Surf. Sci.* 278 (Aug. 2013), pp. 347–351. ISSN: 0169-4332. DOI: 10.1016/j.apsusc.2012.11.075.

[57] Y. C. Guan et al. "Femtosecond laser-induced ripple structures on magnesium". In: *Appl. Phys. A* 115.1 (Apr. 2014), pp. 13–18. ISSN: 1432-0630. DOI: 10.1007/s00339-013-7927-5.

[58] Kiminori Okamuro et al. "Laser fluence dependence of periodic grating structures formed on metal surfaces under femtosecond laser pulse irradiation". In: *Phys. Rev. B* 82.16 (Oct. 2010), p. 165417. ISSN: 2469-9969. DOI: 10.1103/PhysRevB.82.165417.

[59] A. Pan et al. “Formation of laser-induced periodic surface structures on niobium by femtosecond laser irradiation”. In: *J. Appl. Phys.* 115.17 (May 2014), p. 173101. ISSN: 0021-8979. DOI: 10.1063/1.4873459.

[60] Xxx Sedao et al. “Growth twinning and generation of high-frequency surface nanostructures in ultrafast laser-induced transient melting and resolidification”. In: *ACS nano* 10.7 (2016), pp. 6995–7007.

[61] Fotis Fraggelakis et al. “Controlling 2D laser nano structuring over large area with double femtosecond pulses”. In: *Applied Surface Science* 470 (2019), pp. 677–686.

[62] George D. Tsibidis et al. “Modelling periodic structure formation on 100Cr6 steel after irradiation with femtosecond-pulsed laser beams”. In: *Appl. Phys. A* 124.1 (Jan. 2018), pp. 1–13. ISSN: 1432-0630. DOI: 10.1007/s00339-017-1443-y.

[63] J. Bonse et al. “Sub-100-nm laser-induced periodic surface structures upon irradiation of titanium by Ti:sapphire femtosecond laser pulses in air”. In: *Appl. Phys. A* 110.3 (Mar. 2013), pp. 547–551. ISSN: 1432-0630. DOI: 10.1007/s00339-012-7140-y.

[64] Miklos Fule et al. “Comparative study of the surface nanostructure formation on different surfaces generated by low number of fs laser pulses”. In: *Journal of Laser Micro Nanoengineering* 10.1 (Feb. 2015), pp. 74–81. ISSN: 1880-0688.

[65] Tianchi Chen et al. “Laser-Induced Nanostructures on the Zinc Surface”. In: *J. Russ. Laser Res.* 35.6 (Nov. 2014), pp. 561–569. ISSN: 1573-8760. DOI: 10.1007/s10946-014-9463-y.

[66] Nisar Ali et al. “Nanostructuring of zirconium by femtosecond laser irradiation in the ambient environment of air and ethanol”. In: *Optik* 134 (Apr. 2017), pp. 149–160. ISSN: 0030-4026. DOI: 10.1016/j.ijleo.2017.01.021.

[67] Jörn Bonse and Stephan Gräf. “Maxwell Meets Marangoni—A Review of Theories on Laser-Induced Periodic Surface Structures”. In: *Laser & Photonics Reviews* 14.10 (2020), p. 2000215.

[68] Zhou Guosheng, P. M. Fauchet, and A. E. Siegman. “Growth of spontaneous periodic surface structures on solids during laser illumination”. In: *Phys. Rev. B* 26.10 (Nov. 1982), pp. 5366–5381. ISSN: 2469-9969. DOI: 10.1103/PhysRevB.26.5366.

[69] JE Sipe et al. “Laser-induced periodic surface structure. I. Theory”. In: *Physical Review B* 27.2 (1983), p. 1141.

[70] V. I. Emel’yanov, Nikolai I. Koroteev, and V. N. Seminogov. “Interaction of powerful laser radiation with the surfaces of semiconductors and metals: nonlinear optical effects and nonlinear optical diagnostics”. In: *Phys.-Usp.* 28.12 (Dec. 1985), pp. 1084–1124. ISSN: 1063-7869. URL: https://ufn.ru/en/articles/1985/12/b/citedby.html.

[71] Anatoliy Y. Vorobyev and Chunlei Guo. "Direct femtosecond laser surface nano / microstructuring and its applications". In: *Laser Photonics Rev.* 7.3 (May 2013), pp. 385–407. ISSN: 1863-8880. DOI: 10.1002/lpor.201200017.

[72] Anton Rudenko et al. "High-frequency periodic patterns driven by non-radiative fields coupled with Marangoni convection instabilities on laser-excited metal surfaces". In: *Acta Materialia* 194 (2020), pp. 93–105.

[73] Allen Taflove, Susan C Hagness, et al. "Computational electrodynamics: the finite-difference time-domain method". In: *Norwood, 2nd Edition, MA: Artech House, l995* (1995).

[74] Sergei I. Anisimov and B. S. Luk'yanchuk. "Selected problems of laser ablation theory". In: *Physics-Uspekhi* 45.3 (2002), p. 293.

[75] Anton Rudenko et al. "Amplification and regulation of periodic nanostructures in multipulse ultrashort laser-induced surface evolution by electromagnetic-hydrodynamic simulations". In: *Phys. Rev. B* 99 (23 2019), p. 235412.

[76] J. Z. P. Skolski et al. "Modeling laser-induced periodic surface structures: Finite-difference time-domain feedback simulations". In: *J. Appl. Phys.* 115.10 (Mar. 2014), p. 103102. ISSN: 0021-8979. DOI: 10.1063/1.4867759.

[77] Camilo Florian et al. "The Role of the Laser-Induced Oxide Layer in the Formation of Laser-Induced Periodic Surface Structures". In: *Nanomaterials* 10.1 (Jan. 2020), p. 147. ISSN: 2079-4991. DOI: 10.3390/nano10010147.

[78] A. V. Dostovalov et al. "Oxide composition and period variation of thermochemical LIPSS on chromium films with different thickness". In: *Opt. Express* 26.6 (Mar. 2018), pp. 7712–7723. ISSN: 1094-4087. DOI: 10.1364/OE.26.007712.

[79] Juergen Reif et al. "The role of asymmetric excitation in self-organized nanostructure formation upon femtosecond laser ablation". In: *AIP Conf. Proc.* 1464.1 (July 2012), pp. 428–441. ISSN: 0094-243X. DOI: 10.1063/1.4739897.

[80] Olga Varlamova, Mourad Bounhalli, and Juergen Reif. "Influence of irradiation dose on laser-induced surface nanostructures on silicon". In: *Appl. Surf. Sci.* 278 (Aug. 2013), pp. 62–66. ISSN: 0169-4332. DOI: 10.1016/j.apsusc.2012.10.140.

[81] Florenta Costache, Matthias Henyk, and Jürgen Reif. "Modification of dielectric surfaces with ultra-short laser pulses". In: *Appl. Surf. Sci.* 186.1 (Jan. 2002), pp. 352–357. ISSN: 0169-4332. DOI: 10.1016/S0169-4332(01)00675-4.

[82] Jörn Bonse et al. "Tribological performance of femtosecond laser-induced periodic surface structures on titanium and a high toughness bearing steel". In: *Applied Surface Science* 336 (2015), pp. 21–27.

[83] Anthony Abou Saleh et al. "Sub-100 nm 2D nanopatterning on a large scale by ultrafast laser energy regulation". In: *Nanoscale* 12.12 (2020), pp. 6609–6616.

[84] J. M. Liu. "Simple technique for measurements of pulsed Gaussian-beam spot sizes". In: *Opt. Lett.* 7.5 (1982), pp. 196–198. ISSN: 1539-4794. DOI: 10.1364/OL.7.000196.

[85] Costantino Grana, Daniele Borghesani, and Rita Cucchiara. "Optimized Block-Based Connected Components Labeling With Decision Trees". In: *IEEE Transactions on Image Processing* 19.6 (2010), pp. 1596–1609. DOI: 10.1109/TIP.2010.2044963.

[86] Juha-Matti Savolainen, Martin S. Christensen, and Peter Balling. "Material swelling as the first step in the ablation of metals by ultrashort laser pulses". In: *Phys. Rev. B* 84.19 (2011), p. 193410. ISSN: 2469-9969. DOI: 10.1103/PhysRevB.84.193410.

[87] F. Baset et al. "Nanopillar formation from two-shot femtosecond laser ablation of poly-methyl methacrylate". In: *Appl. Surf. Sci.* 357 (2015), pp. 273–281. ISSN: 0169-4332. DOI: 10.1016/j.apsusc.2015.09.007.

[88] Eduardo Vitral et al. "Spiral defect chaos in Rayleigh-B\'enard convection: Asymptotic and numerical studies of azimuthal flows induced by rotating spirals". In: *Phys. Rev. Fluids* 5.9 (2020), p. 093501. ISSN: 2469-990X. DOI: 10.1103/PhysRevFluids.5.093501.

[89] Anthony Nakhoul et al. "Tailoring the surface morphology of Ni at the nanometric scale by ultrashort laser pulses". In: *Appl. Phys. A* 128.10 (Oct. 2022), pp. 1–7. ISSN: 1432-0630. DOI: 10.1007/s00339-022-06046-2.

[90] Tsing-Hua Her et al. "Microstructuring of silicon with femtosecond laser pulses". In: *Applied Physics Letters* 73.12 (1998), pp. 1673–1675.

[91] J Vincenc Oboňa et al. "Modification of Cu surface with picosecond laser pulses". In: *Applied surface science* 303 (2014), pp. 118–124.

[92] Quan-Zhong Zhao, Stefan Malzer, and Li-Jun Wang. "Self-organized tungsten nanospikes grown on subwavelength ripples induced by femtosecond laser pulses". In: *Optics Express* 15.24 (2007), pp. 15741–15746.

[93] Chengping Wu and Leonid V Zhigilei. "Nanocrystalline and polyicosahedral structure of a nanospike generated on metal surface irradiated by a single femtosecond laser pulse". In: *The Journal of Physical Chemistry C* 120.8 (2016), pp. 4438–4447.

[94] Jiawang Xie et al. "Atomic-Level Insight into the Formation of Subsurface Dislocation Layer and Its Effect on Mechanical Properties During Ultrafast Laser Micro/Nano Fabrication". In: *Advanced Functional Materials* (2021), p. 2108802.

[95] Denver P Linklater et al. "Mechano-bactericidal actions of nanostructured surfaces". In: *Nature Reviews Microbiology* 19.1 (2021), pp. 8–22.

[96] Jafar Hasan et al. "Antiviral nanostructured surfaces reduce the viability of SARS-CoV-2". In: *ACS Biomaterials Science & Engineering* 6.9 (2020), pp. 4858–4861.

[97] Alexander Baev et al. "Metaphotonics: An emerging field with opportunities and challenges". In: *Physics Reports* 594 (2015), pp. 1–60.

[98] Arash Ahmadivand and Burak Gerislioglu. “Deep-and vacuum-ultraviolet metaphotonic light sources”. In: *Materials Today* (2021).

[99] Eberhard Bodenschatz, Werner Pesch, and Guenter Ahlers. “Recent Developments in Rayleigh-Bénard Convection”. In: *Annu. Rev. Fluid Mech.* 32.1 (2000), pp. 709–778. ISSN: 0066-4189. DOI: 10.1146/annurev.fluid.32.1.709.

[100] A. Thess and M. Bestehorn. “Planform selection in B\’enard-Marangoni convection: l hexagons versus g hexagons”. In: *Phys. Rev. E* 52.6 (1995), pp. 6358–6367. ISSN: 2470-0053. DOI: 10.1103/PhysRevE.52.6358.

[101] D. H. Sharp. “An overview of Rayleigh-Taylor instability”. In: *Physica D* 12.1 (July 1984), pp. 3–18. ISSN: 0167-2789. DOI: 10.1016/0167-2789(84)90510-4.

[102] R. V. Morgan et al. “Rarefaction-driven Rayleigh–Taylor instability. Part 2. Experiments and simulations in the nonlinear regime”. In: *J. Fluid Mech.* 838 (2018), pp. 320–355. ISSN: 0022-1120. DOI: 10.1017/jfm.2017.893.

[103] Marc K. Smith and Stephen H. Davis. “Instabilities of dynamic thermocapillary liquid layers. Part 1. Convective instabilities”. In: *J. Fluid Mech.* 132 (1983), pp. 119–144. ISSN: 1469-7645. DOI: 10.1017/S0022112083001512.

[104] Marc K. Smith. “Instability mechanisms in dynamic thermocapillary liquid layers”. In: *Phys. Fluids* 29.10 (1986), pp. 3182–3186. ISSN: 0031-9171. DOI: 10.1063/1.865836.

[105] George D. Tsibidis, C. Fotakis, and E. Stratakis. “From ripples to spikes: A hydrodynamical mechanism to interpret femtosecond laser-induced self-assembled structures”. In: *Phys. Rev. B* 92.4 (2015), p. 041405. ISSN: 2469-9969. DOI: 10.1103/PhysRevB.92.041405.

[106] F. H. Busse. “Remarks on the critical value Pc=0.25 of the Prandtl number for internally heated convection found by Tveitereid and Palm”. In: *Eur. J. Mech. B Fluids* 47 (2014), pp. 32–34. ISSN: 0997-7546. DOI: 10.1016/j.euromechflu.2014.04.001.

[107] Thomas Boeck and André Thess. “Bénard–Marangoni convection at low Prandtl number”. In: *J. Fluid Mech.* 399 (1999), pp. 251–275. ISSN: 1469-7645. DOI: 10.1017/S0022112099006436.

[108] J. Bragard and M. G. Velarde. “Bénard–Marangoni convection: planforms and related theoretical predictions”. In: *J. Fluid Mech.* 368 (1998), pp. 165–194. ISSN: 1469-7645. DOI: 10.1017/S0022112098001669.

[109] E. Bévillon et al. “Free-electron properties of metals under ultrafast laser-induced electron-phonon nonequilibrium: A first-principles study”. In: *Phys. Rev. B* 89 (11 2014), p. 115117.

[110] Igor’V. Lomonosov, Aleksey V. Bushman, and Vladimir E. Fortov. “Equations of state for metals at high energy densities”. In: *AIP Conference Proceedings*. Vol. 309. AIP. 1994, pp. 117–120.

[111] Shaojun Wang et al. “Controllable formation of laser-induced periodic surface structures on ZnO film by temporally shaped femtosecond laser scanning”. In: *Opt. Lett.* 45.8 (2020), pp. 2411–2414. ISSN: 1539-4794. DOI: 10.1364/OL.388770.

[112] Ju Swift and Pierre C Hohenberg. “Hydrodynamic fluctuations at the convective instability”. In: *Physical Review A* 15.1 (1977), p. 319.

[113] Mark C Cross and Pierre C Hohenberg. “Pattern formation outside of equilibrium”. In: *Reviews of modern physics* 65.3 (1993), p. 851.

[114] Gilbert Strang. “On the construction and comparison of difference schemes”. In: *SIAM journal on numerical analysis* 5.3 (1968), pp. 506–517.

[115] Randall J LeVeque. *Finite difference methods for ordinary and partial differential equations: steady-state and time-dependent problems*. SIAM, 2007.

[116] Haruo Yoshida. “Construction of higher order symplectic integrators”. In: *Physics letters A* 150.5-7 (1990), pp. 262–268.

[117] Tianqi Guo et al. “Ordered porous structure hybrid films generated by breath figures for directional water penetration”. In: *RSC Adv.* 5.107 (Oct. 2015), pp. 88471–88476. ISSN: 2046-2069. DOI: 10.1039/C5RA13627J.

[118] Eduardo Brandao et al. “Learning PDE to Model Self-Organization of Matter”. In: *Entropy (Basel).* 24.8 (Aug. 2022), p. 1096. ISSN: 1099-4300. DOI: 10.3390/e24081096. eprint: 36010759.